



Low-Energy Electrons in Strong-Field Ionization

DISSERTATION

zur Erlangung des akademischen Grades

Doctor rerum naturalium
(Dr. rer. nat.)

vorgelegt

der Fakultät Mathematik und Naturwissenschaften
der Technischen Universität Dresden

von

Elias Diesen

geboren am 10.11.1984 in Överjärna

MAX-PLANCK-INSTITUT FÜR PHYSIK KOMPLEXER SYSTEME

Dresden, January 2016

Eingereicht am 29. Januar 2016.
Verteidigt am .

1. Gutachter:
2. Gutachter:

Abstract

The ongoing development of more powerful and controllable laser sources in the IR regime, together with the steadily increasing precision of photoelectron detection methods, has led to several unexpected findings in strong-field ionization experiments over the last decades. While a lot of attention has been paid to high energy photoelectrons resulting from interaction of a strong laser field with an atom or a molecule, there are also unresolved questions regarding the spectrum of low energy photoelectrons. We address two such spectral features, the Low Energy Structure (LES) with an energy of a few eV, and the Zero Energy Structure (ZES) with an energy in the meV range. Our treatment of the laser-driven electron dynamics is completely classical. By introducing simplifying assumptions, analytical models are obtained that reproduce the essence of the experimental features; numerical simulations, propagating the classical equations of motion, are used to support the arguments and bridge the gap between our analytical solutions and available experimental results.

Using only a well-known strong-field trajectory model, which we modify to describe motion in few-cycle laser pulses, we arrive at simple analytical estimates for the LES peak energies in short pulses. The scaling formula agrees well with numerical simulations. For comparison with experimental results additional considerations have to be made, taking the different laser intensities within the laser focus into account; this can be included in a compact way. In the end, an agreement well within the experimental accuracy is reached, so that our formula may be used for predictions in future experiments with different laser parameters or ionization targets.

Predicting the LES energies is one issue; explaining how they are formed is another. We approach the problem from a classical nonlinear dynamics viewpoint, introducing a model which allows a fully analytical treatment and agrees well with simulations. An intuitive picture emerges, where the LES results from electrons being driven back by the laser into the vicinity of the ion, and performing low energy "soft" recollisions some 20 au away from it. The recollisions cause a caustic structure in the final momentum spectrum. Carefully separating the discussion of different aspects of this feature, which are sometimes confused in the literature, gives a unified classical view of all LES features.

The ZES caused significant interest when it was experimentally discovered a few years ago, lacking a theoretical explanation. Our treatment shows that the ZES is caused by a secondary field ionization process after the strong-field laser pulse is over; it is an effect of the weak electric field applied in the detector in order to measure the momentum of outgoing charged products. It is thus not a signature of an unknown interaction process between the driven electron and the ionic core, but of excited atomic states being populated by the laser driving. Our analytically derived scaling of the ZES momentum with the detector field is found to agree well with experimental results, supporting our understanding. The fact that it rises so strongly above the spectral background can be understood from classical dynamics - the situation is that of the Stark problem, which allows a thorough analytical treatment. Somewhat surprisingly a relevant aspect of Stark dynamics - the distribution of delay times in an ensemble of escaping trajectories - was not analyzed before, but nevertheless allow a fully analytical treatment, and in the experimental detection method gives rise to a peculiar structure that is identified as the ZES.

Contents

1	Introduction	1
2	High intensity laser-atom interaction	5
2.1	Interaction of strong fields with atoms	5
2.2	Description of the laser field	7
2.3	Strong field physics	10
2.4	High energy rescattering effects	14
2.5	Frustrated tunneling ionization (FTI)	15
2.6	The low energy structure (LES)	15
2.7	Final remarks	18
3	The LES trajectory model	19
3.1	LES three-step model	19
3.2	Classical strong field dynamics	20
3.3	LES trajectories in a continuous wave laser	21
3.4	LES trajectories in a short pulse	23
3.5	Comparison with experiment	28
3.6	Conclusions	32
4	The low energy recollision	35
4.1	The recollision model	36
4.2	Dynamics	40
4.3	VLES recollision	44
4.4	LES recollision	44
4.5	Conclusions	47
5	Realistic LES collision	51
5.1	The joint spectrum	51
5.2	Marginal distributions	54
5.3	Conditional spectrum along $p_\rho = 0$	56
5.4	Experimental detection of the discussed features	60
5.5	Summary	63
6	The Zero-energy-structure	67
6.1	Experimental observation	68
6.2	Hypothesis	70
6.3	Separation of time scales	70
6.4	Stark problem	71

6.5	Simulation results	78
6.6	Comparison with experiment	81
6.7	Quantum effects	83
6.8	Summary	84
7	Stark dynamics	87
7.1	Background	87
7.2	Stark trajectories	88
7.3	Obtaining the measured momentum	90
7.4	Periodicity in the measured momentum spectrum	92
7.5	Analytic expressions	95
7.6	Summary	96
8	Summary and outlook	97
A	Classical spectra	99
A.1	Basic theory	99
A.2	Bivariate probability distributions	100
A.3	2D momentum spectra	101
A.4	Singularities in the spectrum	101
A.5	Critical lines and caustics	102
B	Explicit expression for $G(\varphi)$	107
C	Simulation method	109
C.1	Tunneling	109
C.2	Motion	110
C.3	Focal averaging	111
C.4	The Jacobian	111
C.5	The critical line	111
C.6	The forward direction spectrum	112
C.7	The zero energy structure	112
D	ZES analytics	115
D.1	Calculation of $\xi(\tau)$	115
D.2	Calculation of $\eta(\tau)$	116
D.3	Finding the time delay	117
D.4	Calculating the period of barrier orbits	119

Chapter 1

Introduction

One could conceivably put the birth of atomic physics to the year 1814, when Fraunhofer discovered the presence of absorption lines in the spectrum of sunlight [1], the full explanation of which was then worked out by Kirchhoff and Bunsen in 1859 [2]. The atom - hitherto only an assumed entity used for explaining chemical reactions - thus revealed its own internal properties, and while the internal structure (or even existence of such) was only clarified at the turn of the 20th century, the fact that each atom had its own characteristic optical properties led the way to studying atoms as such.

The interaction between *light* and *matter* was thus, from the earliest moment, both the central tool for studying atoms, and a physical process whose properties needed to be understood. While the work of Maxwell clarified the nature of light as an electromagnetic wave and described its relation to material (electric and magnetic) processes, the exact nature of the interaction was not clear. The arrival of quantum mechanics in early 20th century finally provided a full theoretical basis for atomic physics. A key ingredient was the description of the photoelectric effect, pointing to the quantum theory of light.

Mid-20th century atomic physics had reached a high degree of refinement in measuring atomic spectra, and theoretical explanations of all the observed levels and shifts were available, but one was still confined to bulk experiments on a large number of atoms, and a wide range of frequencies involved. The idea of coherent light, stemming from a single atomic transition, came from theoretical formulations; in particular Einstein's prediction of *stimulated emission* [3] gave hopes of a powerful source of monochromatic light with a well-defined overall phase. While simple in theory, the technical challenges in reaching a higher occupation probability in higher energy levels than lower - the population inversion necessary for amplified stimulated emission - were enormous. In 1960 the device was successfully built and could amplify incoming light at a specific wavelength by many orders of magnitude, obtaining *light amplification by stimulated emission of radiation* - the laser.

While in itself a remarkable application of fundamental atomic physics, the importance of the laser as a tool for investigation of atoms was immediately clear, due to the unprecedented intensity, narrow frequency bandwidth, and coherence of the emitted light. The high intensities reached already by early lasers - around 10^{15} W/cm² within a few years of the first laser - suddenly made it possible to investigate processes that had previously only been *Gedankenexper-*

imente. It was suggested by Göppert-Mayer in 1931 that, at sufficient intensity, a system can absorb several photons at once [4], violating the simple energy conservation law for photoelectric transitions $\Delta E = h\nu$. Instead absorption of n photons gives $\Delta E = nh\nu$. Experimental realization of such *multiphoton* processes became possible with the advent of the laser. This in turn spurred the development of theoretical models for such processes. In particular multiphoton ionization was investigated; ionization of atoms was now possible using even visible or infrared light, due to a large number of photons being involved. Early studies were concerned with the ionization probability only, however with time, ionizing atoms and then measuring the momentum spectrum of the outgoing electrons and/or ions was possible, giving more information about the physical process.

While laser intensities have increased steadily the last 30 years, the available laser pulses have become shorter and shorter - femtosecond pulses are now routine, and as a secondary process pulses of attosecond timescale can be produced. Femtophysics has revealed a lot about chemical reactions and motion of atomic nuclei in molecules - attophysics, still in its cradle, promises to do similar for the motion of electrons in atoms and molecules.

Even though the theory behind multiphoton ionization is highly developed, numerous approximations are always necessary. The process is typically in a parameter regime at the border between several different theories - partly classical mechanics, partly quantum mechanics, sometimes relativistic... The large energy ranges available make the treatment more challenging. Hence theoretical development has often been pushed by new experimental discoveries, and the attention of theorists has been called on by a sequence of surprising results.

This thesis concerns two such unexpected experimental results. The low energy structure (LES) was discovered in 2009 [5] under experimental conditions where common theories were thought to be valid. Its explanation as a rescattering effect was soon put forward. Several different explanations have been suggested, so that a clear consensus has not been reached on its exact origin. Meanwhile its properties under different laser pulses is only partly known, experimentally and theoretically. This thesis aims to contribute to two aspects of the low energy structure: its properties in very short laser pulses, and the detailed mechanism of its formation.

Another unexpected feature was measured in 2013 [6] and named the zero energy structure (ZES). In this thesis a rather complete explanation is put forward, where it results as an effect of the measurement apparatus on the system, and not some kind of unknown scattering process, as was speculated originally. While less spectacular, it still provides information about the system and merits consideration in future experiments. From a theoretical point of view, it can be studied analytically to a high level of detail, and this study even reveals some new aspects of the more than 100 years old Stark problem.

Overview of this thesis

In Chapter 2 the theoretical background for the remaining thesis is outlined, describing the interaction of intense laser light with atoms, the description of the laser light itself, and the different parameter regimes of strong field ionization. Tunneling ionization is taken as a basis for the following discussion, where

the breakdowns of the simple models are described: above threshold ionization (ATI), high harmonic generation (HHG), frustrated tunneling ionization (FTI) and finally the low energy structure (LES). A short survey of the LES literature is included, forming the motivation for subsequent chapters.

In Chapter 3 a classical trajectory model for the LES is introduced and its properties discussed. Emphasis is on the scaling of LES energies with the pulse length of short laser pulses, where an experimental collaboration led to the work of [7]. The model is presented along with simulations, successively introducing more realistic circumstances until a comparison with the experiment is done, showing very good agreement.

Chapter 4 and Chapter 5 are concerned with the mechanism behind the LES peaks. Extending existing models, an analytical diagonalizable model is used to reproduce qualitatively the LES features. By binding these results together with the classical trajectory model of Chapter 3, a complete analytical theory is obtained and shown to agree well with simulations. In Chapter 5 a numerical treatment of the system is used to translate the insights of the analytical model to the fully realistic situation and show how experimentally reported features are related to those of the model.

Leaving the LES, Chapter 6 discusses the zero energy structure (ZES). After presenting the hypothesis of ZES being created by the influence of the electric field of the measurement apparatus on the experimental system, a model is proposed which leads to simple scaling properties of the structure, and reduces the situation to the Stark problem. Extending the simulation method to include this process reproduces the feature in excellent agreement with the experimental results. In a collaborative work [8], the theoretical scaling was confirmed by experimental measurements. The details of the involved Stark dynamics, which can be treated fully analytically, are worked out in Chapter 7. It is seen that the ZES is a generic feature of the Stark problem, which has only now been noticed due to the novel measurement techniques.

Chapter 2

High intensity laser-atom interaction

This chapter gives a short introduction to the theoretical models used in subsequent chapters for the treatment of strong field processes.

The interaction of a laser field with an atom is introduced in Section 2.1, together with the numerous assumptions and simplifications necessary in order to reduce the complexity of the real process and make the study of strong field processes feasible. Since our interest is in interaction with atoms, the simplifications are relatively easy to justify and the complicated behavior that arises in strong field processes in composite systems, like molecules or clusters, is avoided.

In Section 2.2 the properties of a laser pulse is discussed, and the spatial shape of a laser focus is treated.

The basic strong field approximation (SFA) is discussed in Section 2.3 with the two dominant ionization processes - multiphoton and tunneling - and their respective parameter regimes. The treatment is kept short since the main topic of this thesis is the dynamics after initial ionization, so that details of the - highly complex - initial ionization mechanism are not crucial. Thereafter a few of the observed breakdowns of the simple SFA is introduced: high energy above-threshold ionization (ATI), high harmonic generation (HHG) and frustrated tunneling ionization (FTI). These will be related to in subsequent chapters. The focus of Chapters 3-5 of this thesis is the low energy structure (LES). A short summary of the currently available results is given in Section 2.6, forming the motivation for the detailed treatment in the following chapters.

2.1 Interaction of strong fields with atoms

The interaction of an atom with an electromagnetic field is in general a complex problem, with a wealth of phenomena resulting such as photoabsorption, AC Stark splitting of atomic levels, Lamb shift and more [9,10]. Drastic approximations are necessary in order to isolate a single effect.

2.1.1 Single-active-electron approximation

In the situation of a high intensity laser field, the external field is so strong that it dominates the internal structure of the atom. The interest is not in resolving single energy levels, so that treating the whole atom in the simplest possible way is often feasible. This thesis discusses exclusively the single-active-electron approximation, where the motion of an electron is governed by the hydrogenic Hamiltonian, in atomic units:

$$H_{\text{SAE}} = \frac{(\mathbf{p} + \mathbf{A}(\mathbf{r}, t))^2}{2} - \frac{1}{|\mathbf{r}|}.$$

The dynamics of other electrons in the atom is neglected; they serve only to screen the nuclear charge, so that the active electron moves in the Coulomb field of a singly charged ion. The nucleus is treated as fixed (at the origin) due to its high mass. \mathbf{A} is the vector potential of the laser field; the coupling with the electromagnetic field is introduced via the minimal coupling prescription $\mathbf{p} \rightarrow \mathbf{p} + \mathbf{A}$ [11].

2.1.2 Dipole approximation

When dealing with light-driven processes that take place in a small region in space, use can be made of the dipole approximation

$$\mathbf{A}(\mathbf{r}, t) \approx \mathbf{A}(0, t)$$

which brings with itself two effects:

1. The electric field $\mathbf{E} = -d\mathbf{A}/dt$ has no spatial dependence, $\mathbf{E} = \mathbf{E}(t)$.
2. The Lorentz force, which affects the electronic motion over the magnetic field $\mathbf{B} = \text{rot } \mathbf{A}$, is neglected.

The first point is a good approximation if the actual field is roughly constant in the interesting region. This is often written as

$$\mathbf{k} \cdot \mathbf{r} \ll 1$$

where \mathbf{k} is the wave vector of the incoming light and \mathbf{r} the position vector of the system under study. For our systems we have $|\mathbf{k}| \sim \mu\text{m}$ while typically $|\mathbf{r}| \sim \text{nm}$, so the condition is well fulfilled.

The theoretical condition for the Lorentz force to be small is that the electron velocity is much smaller than the speed of light, $v \ll c$. For long wavelength high intensity lasers this is not always fulfilled. An experimentally verified breakdown was reported in [12], at the extreme end of the laser parameters used in this thesis (intensity $I = 6 \cdot 10^{13} \text{ W/cm}^2$, wavelength $\lambda = 3.4 \mu\text{m}$). Still, the error even at these parameters was found small, and we mainly use wavelengths at or shorter than $2 \mu\text{m}$ where indeed $v \ll c$. Therefore we use the dipole approximation.

2.1.3 Length gauge

Within the dipole approximation one can perform a gauge transformation [13] of the Hamiltonian by setting

$$\begin{aligned}\chi &\equiv -\mathbf{r} \cdot \mathbf{A}(t) \\ A_i(t) &\rightarrow A_i(t) + \frac{\partial \chi}{\partial x_i} = 0.\end{aligned}$$

While the vector potential vanishes in the new gauge, a scalar potential is introduced

$$V \rightarrow -\frac{\partial \chi}{\partial t} = -\mathbf{r} \cdot \mathbf{E}(t)$$

which multiplied with the electron charge -1 (atomic units) enters into the length gauge Hamiltonian

$$H_{\text{SAE}} = \frac{\mathbf{p}^2}{2} - \frac{1}{|\mathbf{r}|} + \mathbf{E}(t) \cdot \mathbf{r} . \quad (2.1)$$

This makes the propagating wave of the laser appear as a time-dependent electric field. In this picture the ionization process may be seen as tunneling through a potential barrier, see Fig. 2.3. This not just gives an intuitive physical picture, but is particularly suited as a starting point for numerical simulations.

2.2 Description of the laser field

A laser pulse is an electromagnetic field. Thus it has to obey Maxwell's equations, from which wave equations for the electric and magnetic fields can be derived [14]. Only the electric field is of interest to us, cf. Section 2.1.2. It satisfies

$$\nabla^2 \mathbf{E}(\mathbf{x}, t) - \frac{1}{c^2} \frac{\partial^2 \mathbf{E}(\mathbf{x}, t)}{\partial t^2} = 0$$

In this thesis we discuss linearly polarized fields only, with the polarization direction typically taken as z . The simplest solutions are then plane waves, $\mathbf{E} = F \cos(\mathbf{k} \cdot \mathbf{r} - \omega t) \mathbf{e}_z$, corresponding to a continuous wave (cw) laser field with an infinite spatial extension.

2.2.1 The laser pulse

Laser pulses are obtained by superposition of plane waves. In a physical laser system this is achieved by mode-locking of a large range of frequencies, giving pulses down to a length of a few fs [15]. For not too short pulses one typically writes, within the dipole approximation (i.e. $\mathbf{E}(t) = \mathbf{E}(0, t)$),

$$\mathbf{E}(t) = F_0 g(t) \cos(\omega t + \varphi_{\text{CEP}}) \mathbf{e}_z \quad (2.2)$$

with $g(t)$ the *pulse envelope*, ω the *central frequency*, φ_{CEP} the *carrier envelope phase* and F_0 the *peak field strength*. The exact shape of the pulse envelope of a

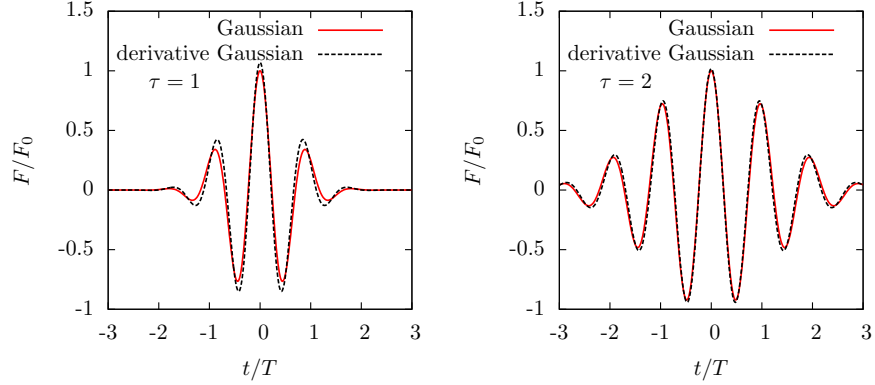


Figure 2.1: Comparison of the two pulse definitions for a one and two cycle pulse (FWHM). $T = 2\pi/\omega$ is the laser period.

femtosecond laser pulse depends on the system; for theoretical treatment a few idealized $g(t)$ are in common use.

The pulse can also be defined via the vector potential:

$$\mathbf{A}(t) = -\frac{F_0}{\omega} f(t) \sin(\omega t + \varphi_{\text{CEP}}) \mathbf{e}_z \quad (2.3)$$

from which the electric field is found as

$$\mathbf{E}(t) = -\frac{d\mathbf{A}}{dt} . \quad (2.4)$$

For pulses longer than a few cycles $f(t) \approx g(t)$.

Whatever theoretical model is used, it is necessary that

$$\int_{-\infty}^{\infty} \mathbf{E}(t) dt = 0 .$$

This corresponds to a vanishing first Fourier coefficient, i.e. the field contains no DC component. If one builds up the pulse in the frequency representation, as is done in real laser pulses by combining frequencies, this is automatically enforced since a constant field is not a solution of the Maxwell equations, but for theoretical pulses constructed from Eq. (2.2) care is necessary.

We will consider two specific pulse shapes:

Gaussian

The Gaussian pulse is defined as

$$A(t) = -\frac{F_0}{\omega} \exp \left\{ -2 \ln 2 \left(\frac{t}{\tau} \right)^2 \right\} \sin(\omega t - \varphi_{\text{CEP}}) \quad (2.5)$$

τ is the full width at half maximum (FWHM), i.e. the duration when the intensity $I = cF^2$ is larger than half its peak value.

Derivative Gaussian pulse

An alternative, related, pulse definition, which we name here a "derivative Gaussian", is given by [16]

$$A(t) = \frac{F_0}{\omega^2} \frac{d}{dt} \left[\exp \left\{ -2 \ln 2 \left(\frac{t}{\tau} \right)^2 \right\} \cos(\omega t - \varphi_{\text{CEP}}) \right]. \quad (2.6)$$

By defining the vector potential as the derivative of a Gaussian function, trajectory models (see Section 3.4) lead to very compact expressions. The difference between Eq. (2.5) and Eq. (2.6) is visible for a FWHM of $\tau = 1T$ but hardly noticeable for $\tau = 2T$; cf. Fig. 2.1. For longer pulses it is negligible.

2.2.2 Spatial shape of the laser focus

In vacuum the spatial and temporal variation of the field envelope can be separated. The presence of a propagation medium may destroy the separation by dispersion and the optical Kerr effect, leading to self-focusing and other nonlinearities [17]. Strong-field experiments take place at low densities where the separation is an excellent approximation.

In order to reach the necessary intensities the laser beam is focused down to a small fraction of its initial area. It is important in all considerations of experiments that the target (in our case, a cloud of atoms) is typically much larger than the focal spot size, so that different parts are hit by different intensities. The experimental measurement will not take place at a definite intensity, but is the result of an average of measurements at the different intensities present in the focus.

Theoretically the spatial shape of a focused beam is described by a specific solution of Maxwell's equations, the TEM₀₀ Gaussian beam (not to be confused with the Gaussian *temporal* shape discussed in Section 2.2.1). Its intensity distribution close to the focus is, in the paraxial approximation, [17]

$$I = \frac{I_0}{1 + (z/z_R)^2} \exp \left(-\frac{2\rho^2}{w_0^2 [1 + (z/z_R)^2]} \right) \quad (2.7)$$

where the focal spot is at the origin and z_R is the Rayleigh length defined by

$$z_R = \pi w_0^2 / \lambda$$

with w_0 the beam waist and λ the wavelength. z_R gives the distance along the z -axis where the intensity has reduced to half its maximum value I_0 ; w_0 is the width of the radial Gaussian distribution at $z = 0$. See Fig. 2.2

For each intensity I_1 the focal volume with intensity higher than I_1 is given by

$$V(I > I_1) = \int \pi \rho^2(z) dz$$

with $\rho(z)$ given implicitly by Eq. (2.7) for $I = I_1$ and integration limits

$$z = \pm z_R \sqrt{I_0/I_1 - 1}$$

which gives [18, 19]

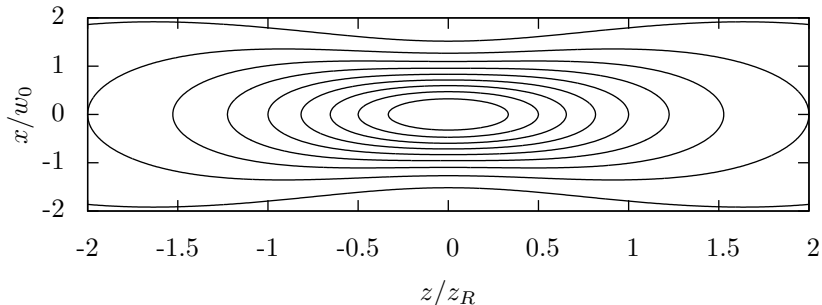


Figure 2.2: Intensity distribution within the focus according to Eq. (2.7), with contour lines at $I/I_0 = 0.9, 0.8, \dots, 0.1$. The axes have been scaled by the Rayleigh length and beam waist, respectively.

$$V(I > I_1) = \pi w_0^2 z_R \left(\frac{4}{3} \beta + \frac{2}{9} \beta^3 - \frac{4}{3} \arctan \beta \right)$$

where $\beta = \sqrt{(I_0 - I_1)/I_1}$. This is a steeply dropping function, meaning that the volume where the highest intensities are reached is relatively small.

The differential relative volume of each isointensity shell is given by

$$dV = \frac{\pi}{3} w_0^2 z_R (2I + I_0) (I_0 - I)^{1/2} I^{-5/2} dI \quad (2.8)$$

which is 0 at I_0 and rapidly increases as I decreases.

For a process giving a measurement outcome x with some intensity dependent probability $w(x, I)$, the measured probability for x from the whole focus will be:

$$w(x) = \int w(x, I) \frac{dV}{dI} dI \quad (2.9)$$

Even for a process strongly dependent on intensity, like tunneling, the focal volume of somewhat lower intensities is typically so large that they also contribute significantly to the observed process. Averaging over the intensities in the focus, by Eq. (2.9), is then necessary in comparing theory with experimental results.

2.3 Strong field physics

In this thesis we are mainly interested in mid-infrared laser fields interacting with single atoms. Experimentally the recent drive has been towards shorter and more precisely controlled pulses [20–22], and more refined measurement techniques [23]. The theoretical treatment of ionization of an atom by high intensity radiation is a rich field, still under development [24–26]; due to the large energy ranges and time scales involved, approximations are necessary that may be valid only in certain parameter ranges or for a part of the whole dynamics.

2.3.1 General overview

The first step is often to treat a zero-range potential, so that the effect of the Coulomb potential is neglected outside the origin, where the initial state is located. This was done already by Keldysh [27] and subsequently refined by Faisal [28] and Reiss [29,30], together giving name to the KFR method. Keldysh identified the adiabaticity parameter that bears his name

$$\gamma \equiv \sqrt{\frac{I_p}{2U_p}} = \omega t_{\text{barrier}}$$

where I_p is the ionization potential (negative bound state energy) and U_p is the ponderomotive energy; for linear polarization

$$U_p = F^2/4\omega^2 .$$

t_{barrier} was defined by Keldysh as the time a classical particle would spend in the barrier region [27]. The two equivalent definitions of γ thus have different physical meaning: one compares the energy scale of the laser driven motion to that of the bound state, the other the typical time scale of ionization to the time scale of the oscillating laser field, leading to the interpretation of γ as a measure of the adiabaticity of the process. γ is used to distinguish between two parameter regimes, each with its own physical interpretation [24, 31, 32]:

$\gamma \gg 1$: Multiphoton

A large value $\gamma \gg 1$ means that the laser field strength is changing rapidly compared to the typical timescale of the ionization process, so that ionization takes place through "shake-up" of the electron energy. The laser field acts as a periodic driving force, successively giving energy to the system. The photon energy is rather high, meaning that a few photons are enough to ionize the atom. More photons than necessary can be absorbed; this is known as above-threshold ionization (ATI). The momentum spectrum typically consists of rings ("ATI rings") at constant energy, each corresponding to a definite photon number.

$\gamma \ll 1$: Tunneling

A different physical picture is valid when γ is small, $\gamma \ll 1$. The laser is then slowly varying with respect to the bound state dynamics, so that the bound state can follow the change of the laser field adiabatically. Ionization proceeds either by tunneling through the barrier (Fig. 2.3) or, for even stronger fields, by classical over-the-barrier motion [33].

Multiphoton	Tunneling
High ω	Low ω
Periodic driving $F(t) \sim \cos \omega t$	Adiabatic ionization $F(t) \sim F_0$
$\gamma \gg 1$	$\gamma \ll 1$
Discrete peaks in energy spectrum	Continuous energy spectrum

Table 2.1: Comparison of the two extreme cases of pure multiphoton vs. pure tunneling ionization.

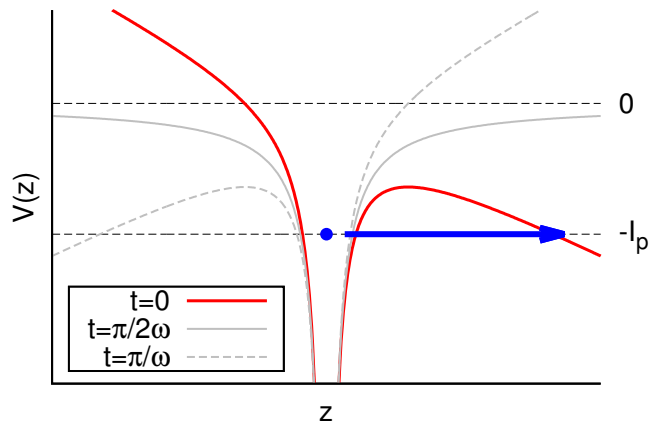


Figure 2.3: Illustration of the tunneling process. I_p is the ionization energy of the atom. As the Coulomb tails are "bent down" by the laser field, an electron can tunnel out. Half a cycle later, tunneling occurs in the opposite direction.

Much of the experimental work is done in a regime where $\gamma \approx 1$ and none of the pictures is entirely valid. While the KFR formulation can deal with any ω and give reasonable results, efforts to improve the result by including the effect of the Coulomb force of the ion on the escaping electron have not been very successful [34]. The tunneling picture can be used as a starting point for numerical simulations, classical or semiclassical, since the tunneling process gives a well defined exit point and exit time, which can be used as initial conditions in a simulation. In this thesis we use the tunneling picture in this way, while keeping in mind that the momentum distribution of a real system contains features depending on the number of photons involved, which are not reproduced by the model and hence do not show up in the simulation. This is especially true for wavelengths below $1 \mu\text{m}$. The rather continuous transition from a tunneling to multiphoton regime, that can be seen in theory [31,35,36] and experiments [37], shows that the discrete features evolve gradually as an additional structure on top of a background which is largely determined by the tunneling result.

2.3.2 Tunneling ionization

A small γ means that the field changes slowly on an atomic time scale. Hence one can assume that the atom follows this change adiabatically, and that there is no transfer of energy from the field to the atom prior to tunneling.

The tunneling rate for a hydrogenic atom with a ground state energy $E = -I_p$ in a constant field is well known [38]

$$w(\mathcal{F}) = \frac{4}{\mathcal{F}} \exp\left(-\frac{2}{3\mathcal{F}}\right). \quad (2.10)$$

where the reduced field strength is defined as

$$\mathcal{F} \equiv F/(2I_p)^{3/2}.$$

The typical tunneling behaviour of all systems is contained already in Eq. (2.10). The dominating influence comes from the exponential dependence on $1/F$, giv-

2.3 Strong field physics

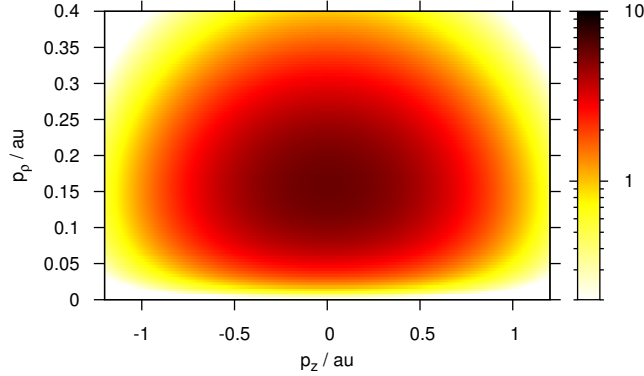


Figure 2.4: Photoelectron momentum spectrum from PPT theory, on a logarithmic color scale, for a laser intensity of $I = 10^{14}$ W/cm² and wavelength of $\lambda = 2$ μ m.

ing a sharply peaked ionization probability at the maximum field strength of a laser pulse.

The tunneling in an alternating field, like that of a laser, was the subject of Keldysh's original paper [27]. The theory for realistic atoms and different ranges of γ was soon afterwards developed, with a highly accurate tunneling rate given in the influential PPT papers [39, 40]

$$w_{lm} = (2I_p)^3 \sqrt{\frac{3}{\pi}} (2l+1) \frac{(l+m)!}{2^m m! (l-m)!} C_{\kappa l}^2 2^{2n^*-m} \cdot F^{m+1.5-2n^*} \exp \left\{ -\frac{2}{3\mathcal{F}} \left(1 - \frac{1}{10} \gamma^2 \right) \right\} \quad (2.11)$$

which with minor adjustments is also known as the ADK tunneling rate [31, 41]. n^* is the effective principal quantum number, l and m the azimuthal and magnetic quantum numbers, respectively, and $C_{\kappa l}$ the asymptotic coefficient of the atom wave function [42]. This gives the cycle-averaged tunneling rate; instantaneous rates are given in e.g. [43]. Note that the relative weight of different field strengths is contained in the second row of Eq. (2.11), while the first only gives a state-dependent prefactor.

The final momentum of the tunneling electron parallel to the polarization axis is, for a zero-range potential, given directly by the vector potential at the tunneling instant $p_z = -A(t')$ (see further Section 3.2). The probability distribution for the momentum perpendicular to the polarization axis can also be found from tunneling theory, so that the final photoelectron momentum spectrum is obtained. For Eq. (2.11) as $\gamma \rightarrow 0$ it takes the form [41]

$$w(\mathbf{p}) = w(0) \exp \left\{ -\left(\frac{\omega^2 (2I_p)^{3/2}}{3F^3} p_{\parallel}^2 + \frac{(2I_p)^{1/2}}{F} p_{\perp}^2 \right) \right\}$$

where

$$w(0) = C_{\kappa}^2 \frac{\omega^2}{\pi^2 F} \left(\frac{\mathcal{F}}{2} \right)^{-2n^*} \exp \left(-\frac{2}{3\mathcal{F}} \right)$$

Due to cylindrical symmetry around the polarization axis, which we choose as z , we can integrate over all azimuthal angles and get the distribution in cylindrical coordinates (p_ρ, p_z) . This momentum spectrum is plotted in Fig. 2.4.

The remainder of this thesis is concerned with dynamics after the tunneling event, manifesting themselves in the final momentum spectrum as modifications of the basic picture of Fig. 2.4.

2.4 High energy rescattering effects

While the tunneling and multiphoton pictures give a good first description of the overall shape of the momentum spectrum of measured photoelectrons, completely neglecting the Coulomb potential after initial escape from the atom is insufficient for explaining several observed phenomena.

The first serious breakdown was measured in 1979 [44,45], where photoelectrons with energies up to around $10U_p$ were measured after tunnel ionization in a linear polarized laser field. From the strong field approximation alone, a maximum energy of around $2U_p$ is expected. The explanation was possible in a classical electron trajectory picture [24,46]. After tunneling, the electron is moving freely driven by the electric field of the laser. It follows directly from Newton's 2nd law that

$$E(t) \sim \cos \omega t \implies z(t) \sim \cos \omega t + v_d t$$

since $\ddot{z}(t) = -E(t)$. This model is discussed in detail in Section 3.2. The electron performs harmonic oscillations but can, due to the linear term coming from the constant drift velocity v_d , recollide with the ion at any time during the cycle. From the model results the maximum energy at recollision [47]:

$$E = 3.17U_p .$$

In a theoretical head-on collision, the momentum of the electron is reversed. It then continues the oscillating motion but with a new v_d . The maximum possible final energy turns out to be [46]

$$E_{\max} = 10.007U_p .$$

Lower energies are about equally probable, so that a plateau is formed in the energy spectrum; the so-called ATI plateau [48]. The cross section for the recollision is very small, so that the plateau is only visible on a logarithmic scale spectrum; above $2U_p$, where there are almost no direct electrons, it is however the dominant spectral feature.

If there is recollision, there is also the possibility of recombination, where the electron recombines with the ion to form a neutral atom. The excess energy is released by emission of a single photon. Since the photon frequency is a multiple of the frequency of the incoming laser, corresponding to a certain number of photons absorbed by the system during the driven motion [49], the process is called high harmonic generation (HHG). It can be described by the so-called three-step model (1: tunneling, 2: driven motion, 3: recombination). The photon energy is limited by $3.17U_p$ [47,50]. Since U_p can reach up to hundreds of eV, the photon is typically in the XUV or X-ray range. This novel method of obtaining highly energetic photons from a table top laser system was first

2.5 Frustrated tunneling ionization (FTI)

realised in 1981 in plasmas [51] and 1987 in atoms [52], and has since become a standard method. It is the method used in obtaining attosecond XUV pulses [53].

2.5 Frustrated tunneling ionization (FTI)

After tunneling out of the atom, the electron performs driven oscillatory motion in the laser field. If its drift momentum v_d is high it escapes quickly from the vicinity of the ion, but if it is small, it returns close to the ion several times during the oscillations, so that the Coulomb field can have a strong influence on the motion. If the laser pulse is short, the electron may not gain enough energy ever to leave the ion, and is instead trapped in a, typically highly excited, bound orbit. The result of the tunneling process is not ionization, but excitation of the atom to an excited state.

The experimental evidence for this process was first obtained in 2008 [54], where it was named frustrated tunneling ionization (FTI). Performing an experiment where tunnel ionization occurred, the yield of neutral highly excited atoms was measured after the laser pulse was over. It was seen that there were indeed excited atoms present. Numerical simulations showed that the spectrum had a sharp increase at $n = 6$, and the distribution $p(n)$ then rapidly dropped to 0 for smaller n . The threshold value $n = 6$ could be explained by considering that oscillations occur with amplitude F/ω^2 (see further Section 3.3), so that an electron with vanishing drift momentum ends up at this distance from the ion, giving the minimum possible energy $-\omega^2/F$ due to the Coulomb potential. The high Rydberg states are stable after excitation, due to the period of the orbits being much longer than the laser period [55,56]; this is reminiscent of the stabilization phenomenon observed at XUV wavelengths [57]. The transition between FTI excitation and ATI is illustrated in [58].

The recapture of electrons was subsequently used to explain the "double-hump" structure of longitudinal momentum spectra [59–61]. In contrast to the tunneling expectation, where there is a maximum in the spectrum in the polarization direction at zero longitudinal momentum given by Eq. (2.11) and visible in Fig. 2.4, there is a dip for the smallest momentum. This is caused by electrons with small drift momentum during the laser pulse being captured after it, so they never escape [56]. While other electrons lose momentum on the way out and partly fill up this range of the momentum spectrum, there is still a net loss in probability, giving the local minimum around $p_z = 0$.

2.6 The low energy structure (LES)

In 2009, another breakdown of the SFA was reported, called the low energy structure [5].

The authors performed strong field ionization experiments with several different targets (noble gas atoms and diatomic molecules). The photoelectron spectrum was measured in the forward direction, i.e. along the laser polarization axis with a small opening angle around it. A significant peak was seen at an energy of a few eV; the ponderomotive energy was $U_p \sim 30$ eV. The peak was present for all different targets, pointing to a universal mechanism. The peak

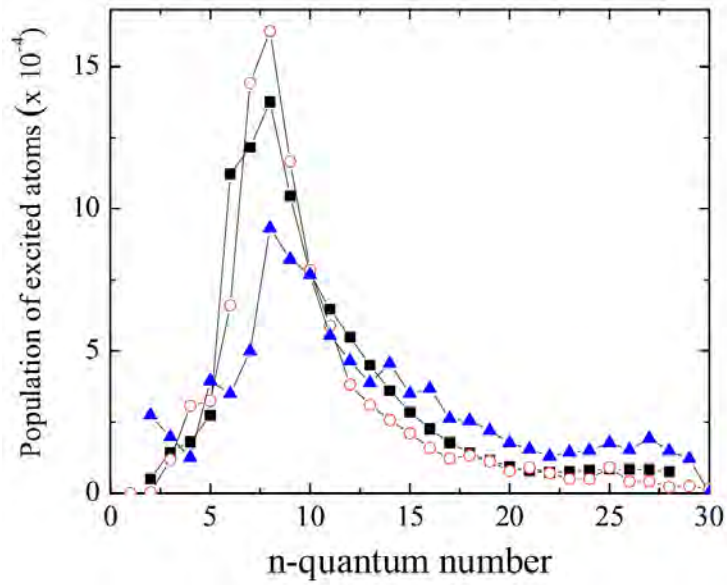


Figure 2.5: Calculated distribution of excited state population after the laser pulse, from [54].

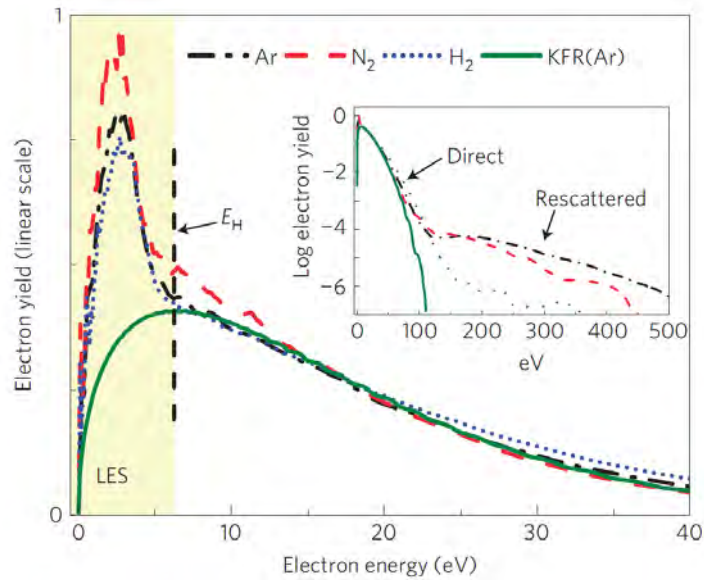


Figure 2.6: The low energy structure as a peak at a few eV, indicating a prominent breakdown of the KFR prediction. Measurements for argon atoms, nitrogen and hydrogen molecules. Inset shows the high energy ATI plateau formed by rescattering electrons. From [5].

2.6 The low energy structure (LES)

energy was seen to depend on the Keldysh parameter roughly as $E_H \sim \gamma^{-1.8}$.

The wavelength was also altered; a wavelength of $0.8 \mu\text{m}$ did not give a visible LES. Instead the ATI peaks associated with different number of participating photons dominate the spectrum. Hence it seemed necessary to be in the tunneling regime with $\gamma \ll 1$ for a clear LES to develop.

TDSE calculations were performed and agreed well with the experimental LES. This strongly indicated that some rescattering was responsible for the structure, since it is neglected in the SFA but present in the full problem. While the Coulomb potential could explain the shift of low energy electrons due to the FTI, it was expected to have a smooth influence and not give a pronounced, well defined peak at small positive energy.

Soon afterwards the experimental findings were confirmed [62]. In this experiment a possible second peak was observed close to zero. The experiment was compared to a semiclassical CTMC simulation similar to that described in Appendix C, and an agreement was found for wavelengths longer than $\lambda \approx 1.2 \mu\text{m}$. Hence a pure quantum effect was ruled out, so that the LES seemed to be a classical recollision effect.

A number of theoretical investigations followed. In [63] a classical analysis was used, drawing the conclusion that the LES is due to a focusing of transverse momenta into the forward direction, so-called Coulomb focusing [64]. The authors analyzed the different kind of trajectories that contribute to the LES, but the actual mechanism behind the focusing was not further clarified.

[65] used a semiclassical approach based on quantum orbits, that extends the strong-field approximation taking Coulomb effects into account. The idea behind the model is to use classical trajectories, including the Coulomb field, and including a quantum phase which is accumulated along the orbit. The final momentum distribution shows quite good agreement with TDSE results, with the additional advantage that an intuitive picture of the motion can be obtained from the classical trajectories used. (In a pure quantum treatment the trajectory concept loses its meaning.) The authors identified a caustic structure in the 2D momentum spectrum, identified this with the LES, and identified the type of trajectories responsible. Like [62] they stressed the importance of transverse focusing in the caustic formation.

The role of the asymptotic Coulomb potential was investigated in [66], which serves to complete the picture but does not by itself explain the observed LES features.

In [67] the LES peak momenta were shown to result directly from the classical trajectory model. Not just a single peak, but several peaks were predicted with definite momenta. The scaling with laser wavelength and field strength was shown to result immediately from the model. Furthermore, a mechanism behind the actual peak formation was suggested. This is based on so-called "soft recollisions" at odd number of half-periods, happening around 20 au distance from the ion, resulting in a "bunching" of longitudinal momenta. The mechanism was shown to give a pronounced peak in the longitudinal spectrum. In contrast to [65] and [63], the longitudinal momentum was identified as the significant one for LES formation. In [68], the same authors investigated the short pulse characteristics of the LES, indicating the CEP dependence of the LES and supporting the proposed recollision model.

[69] stressed the two-dimensional characteristic of the LES, and showed using CTMC simulations that a caustic-like structure was also visible when not

measuring final 2D momentum, but instead final energy and angular momentum. This sheds light on the physical process, but does not immediately translate to experiments since the angular momentum of the escaping electron is not a measurable quantity. The model was further elaborated in [70] and compared to TDSE and Coulomb-corrected SFA calculations.

[71] reported another experiment where the LES was resolved. In particular the peak at low energies was stressed, given the name VLES (very low energy structure). Classical simulations reproduced the observed structures. [72] further investigated the scaling properties and relation to the ATI peaks, using a quantum S-matrix treatment with scattering included to the lowest order.

The last years saw an increase in measurement precision, with fully resolved 2D momentum spectra being published [22, 73]. The LES was thus confirmed as occurring not only on the forward polarization axis, but as an increase in probability along a range of perpendicular momenta.

2.7 Final remarks

This chapter has given a short overview of strong field ionization of atoms. The general theory has been outlined, and the specific laser pulse shape and focal intensity distributions that will be used in this work have been described.

There are still many interesting open questions regarding the tunneling process (the question of tunneling time being at the moment the most debated one) and the transition to the multiphoton regime. The model described here is in many ways the simplest one possible, but is, together with numerical simulations, very powerful in explaining experimental results.

The focus of this thesis is the classical dynamics *after* tunneling, in the combined field of the ion and the laser. The details of the ionization probability will not severely affect the results presented, and therefore the somewhat pedestrian approach we take to the tunneling event is justified.

Chapter 3

The LES trajectory model

The appearance of the low energy structure (LES) has often been reproduced by considering the classical motion of the electron after tunneling [62, 63, 67]. Due to its appearance in classical trajectory simulations, it clearly is a classical effect, with quantum effects only slightly modifying the final result, at least for wavelengths $\lambda > 1 \mu\text{m}$. For shorter wavelengths single photon effects, the ATI rings, increasingly dominate the spectrum. [62, 74, 75].

In this chapter the trajectories and the recollision effects are treated in a simplified way, that has been found a useful approximation for finding the properties of the LES, and for intuitive understanding of the process. The discussion concerns what could be called a "classical strong field approximation", where the dynamics is treated completely classically and the Coulomb field is neglected after tunnel ionization. It is also known as the simple man's model [76, 77]. The ensuing dynamics is that of the celebrated three-step model for high harmonic generation (see Section 2.4).

From this model a series of LES peak energies are obtained, giving a first approximation to *where* in the spectrum the peaks are formed. The question of *how* they are formed is beyond the three-step model. It is discussed in detail in Chapter 4 and 5.

The model and resulting dynamics is presented in Section 3.1 and Section 3.2. To introduce the essential parts of the model, Section 3.3 discusses continuous wave laser fields only. The interesting modifications in pulses - in particular short ones - is discussed in detail in Section 3.4. A comparison with experiment is done in Section 3.5 together with a description of additional considerations that need to be taken into account.

3.1 LES three-step model

The LES can be described as a three-step process:

1. Tunnel ionization close to the field maximum.
2. Driven dynamics in the laser field alone (Coulomb field neglected).
3. Recollision with low energy - interaction gives visible low energy structures in final electron momentum.

The three-step model starts with a tunneling event, where the electron is separated from the ion. The central idea is that the effect of the interaction between the ion and the electron is only taken into account in the first and final step, which are both *instant* in time. The time dynamics is contained in the second part, where neglecting the Coulomb field gives a significant simplification, to the extent that the motion is given by analytical expressions. The initial tunneling step is well investigated, cf. Section 2.3.2.

In this chapter, the second step will be treated in detail. In Chapter 4 the third step is addressed.

The time evolution of trajectories treated here is identical to that used in the three-step HHG model (cf. Section 2.4). The only difference is the rescattering condition (3rd step) - while HHG/ATI assumes a high energy recollision, we look for low energy recollisions.

3.2 Classical strong field dynamics

Simply neglecting the Coulombic term in the full Hamiltonian Eq. (2.1) yields:

$$H_{\text{SFA}} = \frac{\mathbf{p}^2}{2} + \mathbf{r} \cdot \mathbf{E}(t) .$$

The classical trajectory of the electron follows from Newton's second law $\mathbf{F} = m\ddot{\mathbf{r}}$. The only force acting on the electron is the laser field $\mathbf{E}(t)$. In atomic units

$$\begin{aligned} \ddot{\mathbf{r}}(t) &= -\mathbf{E}(t) \\ \dot{\mathbf{r}}(t) &= \mathbf{v}_0 - \int_{t_0}^t dt' \mathbf{E}(t') = \mathbf{v}_0 + \mathbf{A}(t) - \mathbf{A}(t_0) \\ \mathbf{r}(t) &= \mathbf{r}_0 + (t - t_0)(\mathbf{v}_0 - \mathbf{A}(t_0)) + \int_{t_0}^t dt' \mathbf{A}(t') \end{aligned} \quad (3.1)$$

where \mathbf{v}_0 is the initial velocity and \mathbf{r}_0 the initial position. \mathbf{A} is the vector potential, cf. Eq. (2.4). The initial conditions must be obtained from the treatment of the ionization process. In the tunneling case, they are commonly taken as

$$\begin{aligned} \mathbf{r}_0 &= 0 \\ \mathbf{v}_{0,\parallel} &= 0 \quad \text{in the polarization direction} \end{aligned}$$

Perpendicular to the polarization direction, $\mathbf{v}_{0,\perp}$ can take any value. Motion in this direction is trivial since no force is acting.

The trajectory picture is very simple: perpendicular to polarization, the electron moves away with constant velocity. Parallel to the polarization, it performs oscillating motion due to the laser driving, plus a constant drift motion given by the vector potential at the tunneling instant. This *drift momentum* $\mathbf{v}_d = -\mathbf{A}(t_0)$ is what remains after the laser pulse is over, and what is measured as an outgoing momentum at the detector. The first question we want to answer is: for which \mathbf{v}_d is a low energy rescattering possible?

3.3 LES trajectories in a continuous wave laser

We first study the trajectories under a continuous wave (cw) laser, i.e. $g(t) = 1$ in Eq. (2.2). This can be thought of as the limiting case of a very long laser pulse, compared to the period. As will be shown below the results for time-limited pulses converge to the cw results, and the driven motion by the laser is very well approximated by the cw description for pulses of more than about 10 cycles length; already for a 4 cycle pulse the quantitative agreement is quite good.

In a cw laser the vector potential Eq. (2.3) simplifies to

$$\mathbf{A}(t) = -\frac{F}{\omega} \sin \omega t \mathbf{e}_z$$

since the CEP is not defined for a cw laser and can be taken as 0. The trajectories Eq. (3.1) take the form

$$\begin{aligned} \dot{z}(t) &= \frac{F}{\omega} [\sin \omega t_0 - \sin \omega t] \\ z(t) &= \frac{F}{\omega^2} [(\omega t - \omega t_0) \sin \omega t_0 + \cos \omega t - \cos \omega t_0] . \end{aligned} \quad (3.2)$$

A recollision occurs when, for some t_1

$$z(t_1) = 0 .$$

For the recollision to give a low-energy feature, it is expected that the electron has low energy at the recollision instant. Although the energy may change drastically at a recollision very close to the ion, such collisions are almost chaotic, and give a broad range of final energies, including the ATI plateau (Section 2.4). They will not contribute significantly to the low energy spectrum. One can therefore expect that the low energy features stem predominantly from electrons with low velocity at recollision, i.e.

$$\dot{z}(t_1) = 0 .$$

These two conditions inserted into Eq. (3.2) give

$$\begin{aligned} 0 = \sin \omega t_0 - \sin \omega t_1 &\implies \begin{aligned} \omega t_1 &= 2n\pi + \omega t_0 \text{ (VLES) or} \\ \omega t_1 &= (2n+1)\pi - \omega t_0 \text{ (LES)} \end{aligned} \\ 0 = (\omega t_1 - \omega t_0) \sin \omega t_0 + (\cos \varphi_1 - \cos \omega t_0) &\implies \sin \omega t_0 = \frac{2 \cos \omega t_0}{\omega t_1 - \omega t_0} . \end{aligned}$$

There are two types of recolliding trajectories, which we call the LES type *viz.* the VLES type. See figure Fig. 3.1.

Since ionization takes place close to the field maximum, t_0 is small so we use $\sin \omega t_0 \approx \omega t_0$, $\cos \omega t_0 \approx 1$, and further set the denominator $\omega t_1 - \omega t_0 \approx \omega t_1 + \omega t_0$ in the LES case. We then get the trajectory conditions [67]

$$\begin{aligned} t_0 &= \frac{1}{(n+1/2)\pi} \quad \text{n}^{\text{th}} \text{ order LES trajectory} \\ t_0 &= 0 \quad \text{VLES trajectory} \end{aligned} \quad (3.3)$$

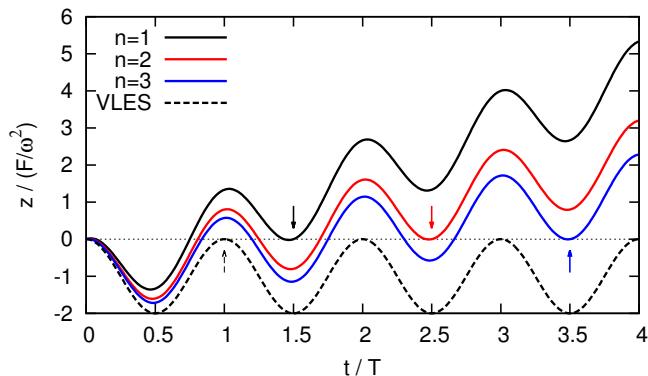


Figure 3.1: The motion in the polarization direction of the first three LES trajectories, and the VLES trajectory, as functions of time. $T = 2\pi/\omega$ is the laser period. Arrows indicate the rescattering events given by Eq. (3.4).

The recollision event for these trajectories takes place close to

$$\begin{aligned}
 t_1 &= (2n + 1) \frac{\pi}{\omega} && \text{odd number of half cycles} \\
 t_1 &= 2n \frac{\pi}{\omega} && \text{even number of half cycles}
 \end{aligned} \tag{3.4}$$

and their respective drift momenta are [67]

$$\begin{aligned}
 p_z &= \frac{F}{\omega} \frac{1}{(n + 1/2)\pi} && n^{\text{th}} \text{ order LES trajectory} \\
 p_z &= 0 && \text{VLES trajectory.}
 \end{aligned} \tag{3.5}$$

The LES trajectories form a series, with the recollision taking place after an odd number of half-cycles. As the order of the recollision increases the ionization takes place closer to the field maximum, giving a smaller drift momentum. This is seen in Fig. 3.1 where the position z is plotted as function of time t , in scaled variables. The drift momentum corresponds to the average slope of the trajectories, which decreases for each higher order.

The VLES condition allows one trajectory only, which recollides after each full cycle. Its drift momentum is 0. Even though it is thus impossible to detect directly since it will be captured in the FTI process (Section 2.5), they still play a role during the laser-driven dynamics, and trajectories close to the VLES one may participate in the interaction with the core and nevertheless escape.

The energy of the LES peaks of Eq. (3.5) scale with the pondermotive energy U_p . Although initially the experimental scaling $E_{\text{LES}} \sim \gamma^{-1.8}$ was reported [5], the scaling $E_{\text{LES}} \sim \gamma^{-2} \sim U_p$ now seems established [71] and is further supported by the work presented in Section 3.5 and [7].

The final energy, which is recorded experimentally, is always slightly lower than that predicted by the trajectory model. This is due to the dynamics *after* recollision, when the electrons have to escape from the Coulomb field.

3.4 LES trajectories in a short pulse

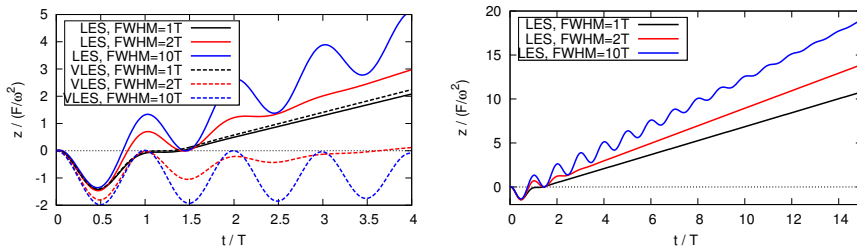


Figure 3.2: Left: Illustration of 1st order VLES and LES trajectories in a Gaussian pulse of different length. The final slope of the trajectory gives the drift momentum in units of $F/2\pi\omega$. Right: A few 1st order LES trajectories zoomed out, showing the asymptotic slope.

3.4 LES trajectories in a short pulse

In a short laser pulse the recollision conditions Eq. (3.3) must be modified. The shorter the pulse gets, the more does the final momenta deviate from those of Eq. (3.5). The pulse length and CEP dependence of the LES was initially studied for short pulses in [68], while a full treatment of the scaling properties for different pulse lengths and comparison with experiment was done in [7]. Here we discuss these results.

3.4.1 Recollision trajectories

One can intuitively understand how the drift momentum changes qualitatively when going from a cw field to a pulsed field, especially for $\varphi_{\text{CEP}} = 0$. The ionization will be increasingly centered around the center cycle within the pulse, since the tunneling rate depends exponentially on the field strength and this decreases towards the beginning and end of the pulse. For a few-cycle pulse, considering ionization only from the cycle in the pulse center is a good approximation. A VLES trajectory ionized at $\varphi = 0$ no longer returns to the core after one full cycle - the decreasing field does not drive it all the way back to the ion. For a return and subsequent low energy rescattering, giving a VLES structure, it needs a certain non-zero drift momentum. The shorter the pulse, the faster it needs to move in order to return to the core. For a LES trajectory the reasoning is similar, but works in the opposite direction: the pulse does not offset the electron as far from $z = 0$ as a cw laser, meaning that it needs to move slower than the cw LES electron. See Fig. 3.2.

The total offset from $z = 0$, by motion in the laser alone, at time t_1 is given by

$$\Delta z = \int_{t_0}^{t_1} A(t) dt .$$

The drift momentum have to compensate this motion exactly for a return to the origin at t_1 , so that

$$p_z = -\frac{\int_{t_0}^{t_1} A(t) dt}{t_1 - t_0} . \quad (3.6)$$

An appealing interpretation of this expression is that the drift momentum must be exactly equal to the time-averaged momentum of the laser-driven motion, with opposite sign.

In contrast to the cw case, the VLES is no longer degenerate with the order of rescattering - returning to the core after N cycles does not give the same VLES momentum as a return after $N + 1$. The splitting is however small and could not be resolved in simulations. Furthermore, ionization at different peaks of the laser field now gives different values for the LES/VLES momenta, where the center peak is expected to dominate strongly for short pulses due to the exponential ionization yield. For a long pulse on the other hand, this effect is weaker as all peaks converge to the cw ones. In an experimental situation resolving these "side-peaks" seems difficult as of now, and the result of this intermediate-length pulse effect is an overall broadening of the LES peaks.

In the two following sections we will use Eq. (3.6) for the two specific pulse shapes of Section 2.2.1 and derive the momenta of the LES and VLES. The Gaussian pulse is chosen for its realism and wide use in simulations, while the derivative Gaussian pulse is chosen since it gives very simple analytical expressions. The difference is shown to be negligible for pulse lengths exceeding 2 cycles, pointing to the universal nature of the scaling introduced here.

3.4.2 Gaussian pulse

The vector potential is taken to have a Gaussian shape Eq. (2.5) To allow for an analytical estimate, we assume that recollision takes place according to Eq. (3.4); for a Gaussian pulse this is a good approximation even when $\tau \approx 1$. The recollision momentum condition is given by inserting Eq. (2.5) into Eq. (3.6)

$$p_z = \frac{F_0}{\omega} \frac{1}{\varphi_1 - \varphi_0} \int_{\varphi_0}^{\varphi_1} \exp \left\{ -2 \ln 2 \frac{(\varphi + \varphi_{\text{CEP}})^2}{\omega^2 \tau^2} \right\} \sin \varphi d\varphi$$

where we change the integration variable to $\varphi = \omega t - \varphi_{\text{CEP}}$. Since tunneling occurs close to $A(t) = 0$, the integration limits are approximated as $\varphi_0 = 0$, $\varphi_1 = 2n\pi$ for the n^{th} VLES and $\varphi_1 = (2n + 1)\pi$ for the n^{th} LES.

Using the integral identity [78]

$$\int e^{-ax^2} \sin bxdx = \frac{\sqrt{\pi}}{2\sqrt{a}} e^{-b^2/4a} \text{Im erf} \left\{ \frac{2ax + ib}{2\sqrt{a}} \right\}$$

we obtain

$$p_z = \frac{F_0}{\omega} \frac{1}{\varphi_1} \frac{\sqrt{\pi}}{2\sqrt{a}} e^{-1/4a} \text{Im} \left(\text{erf} \left\{ \frac{2a(\varphi_1 + \varphi_{\text{CEP}}) + i}{2\sqrt{a}} \right\} - \text{erf} \left\{ \frac{2a\varphi_{\text{CEP}} + i}{2\sqrt{a}} \right\} \right)$$

$$a = \frac{2 \ln 2}{\omega^2 \tau^2} . \quad (3.7)$$

3.4.3 Derivative Gaussian pulse

Using the alternative pulse definition Eq. (2.6) one similarly gets

$$p_z = -\frac{F_0}{\omega} \frac{1}{\varphi_1} \left(\exp \left\{ -a(\varphi_1 + \varphi_{\text{CEP}})^2 \right\} \cos \varphi_1 - \exp \left\{ -a\varphi_{\text{CEP}}^2 \right\} \right) \quad (3.8)$$

3.4 LES trajectories in a short pulse

Experimentally the pulse length τ is typically expressed as a number of cycles k , i.e. $\tau = 2\pi k/\omega$. Using this we get $a = 2 \ln 2/4\pi^2 k^2$. For the n^{th} order LES we have $\varphi_1 = (2n + 1)\pi$ so that we can express Eq. (3.8) as

$$p_z = \zeta(k, n, \varphi_{\text{CEP}})p_\infty$$

where

$$\zeta(k, n, \varphi_{\text{CEP}}) = \frac{1}{2} \left(\exp \left\{ -\frac{\ln 2 \varphi_{\text{CEP}}^2}{2(k\pi)^2} \right\} + \exp \left\{ -\frac{\ln 2(2n + 1 + \varphi_{\text{CEP}}/\pi)^2}{2k^2} \right\} \right)$$

$$p_\infty = \frac{F_0}{\omega} \frac{1}{(n + 1/2)\pi} \quad (3.9)$$

The effect of the pulse is an overall shift to lower momenta, entering as a factor ζ to be multiplied with the asymptotic result p_∞ of a cw field.

For $\varphi_{\text{CEP}} = 0$ Eq. (3.9) takes the simpler form

$$\zeta(k, n, 0) = \frac{1}{2} \left(1 + \exp \left\{ -\frac{\ln 2(2n + 1)^2}{2k^2} \right\} \right) \quad (3.10)$$

which is applicable also for a randomized CEP, as will be shown.

3.4.4 CEP dependence

The two pulses are compared in Fig. 3.3. The curves are almost indistinguishable and the difference is much smaller than the experimental accuracy presently possible. This motivates using the derivative Gaussian pulse for theoretical work, due to its much simpler structure and yet accurate results, at least down to pulse lengths of about 1.5 laser cycle.

The curves for $\varphi_{\text{CEP}} \pm \pi/2$ are also included in Fig. 3.3. Any larger CEP means that the next or preceding half-cycle has a higher peak field strength and consequently should be used as 0 when defining the CEP; since we are in this section only concerned with the energy of the dominant LES peak, regardless of which direction the electrons are escaping in, this means we can interpret $\varphi_{\text{CEP}} = \pi/2 + x$ as $\varphi_{\text{CEP}} = -\pi/2 + x$.

The LES for a fixed non-zero CEP was investigated in [68]. The peak location is available from the formulae of Sections 3.4.2 and 3.4.3. Since $\varphi_{\text{CEP}}/\pi < 1/2$ a series expansion of the exponentials in Eq. (3.9) converges quickly; already the quadratic terms have small influence, so that the LES peaks shift almost linearly with varying CEP

$$\zeta(k, n, \varphi_{\text{CEP}}) \approx \frac{1}{2} \left(1 + \exp \left\{ -\frac{\ln 2(2n + 1)^2}{2k^2} \right\} \left[1 - \frac{\ln 2(2n + 1)}{2k^2\pi} \varphi_{\text{CEP}} \right] \right) \quad (3.11)$$

Many experiments are done without stabilized CEP, so that each successive pulse in the experiment has its own CEP. The Gouy shift [79] further gives a distribution of CEP:s within the focus, even for a single pulse. One then has to average over the theoretical CEP values to get a comparison with experiment. Within the linear approximation Eq. (3.11) the average over an even distribution

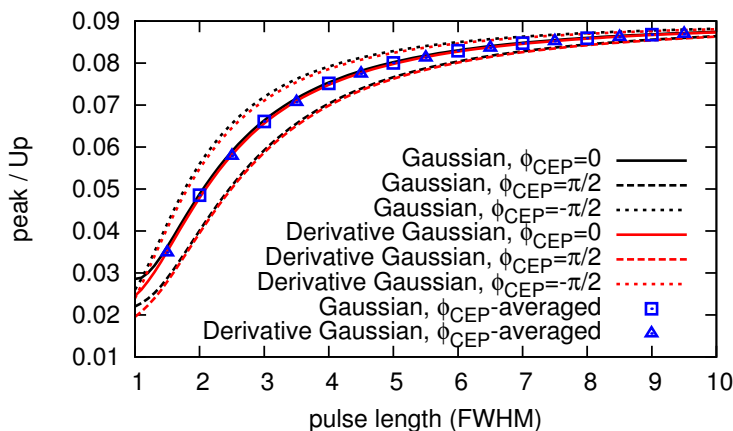


Figure 3.3: The 1st order LES peak energy in units of U_p as function of pulse length. The two pulse shapes with different CEP are compared; the CEP averaged peak energy is seen to agree excellently with the zero CEP value.

of CEP values returns trivially the zero CEP result. The higher order terms introduce a small shift, but as can be seen in Fig. 3.3 this shift is completely negligible. Thus the LES peak value is quite accurately given by the zero CEP value, even in a setup with random CEP.

3.4.5 Simulation results

The theoretical results are compared with CTMC simulation results (see Appendix C for a description of the numerical method) in Fig. 3.4, for a $3.2 \mu\text{m}$ laser ionizing argon atoms at $I = 10^{14} \text{ W/cm}^2$ and $\varphi_{\text{CEP}} = 0$. The peak energies are obtained from the spectrum of electrons emitted in the forward direction along the polarization axis, within an opening angle of 5° . See Fig. 3.5. The agreement is good for the first two LES curves. While it is tempting to identify the VLES in the simulation result, careful analysis of the spectra reveals that the first two points close to the VLES curve actually correspond to forming 1st and 2nd order LES, and the other points may be due to higher order LES forming. The VLES trajectory is not clearly visible in the final result, since it is mixed with higher order LES. Due to the VLES electrons typically staying close to the ion when the pulse dies out, the VLES seems to be made invisible by the FTI recapture process described in Section 2.5.

One powerful aspect of numerical simulation is the ability to look into the dynamics and present intermediate results that are not available in an experimental setting. In classical simulation in particular the system is represented by a point in phase space, so that all momenta and positions are sharply defined at any instant. In our system it is thus possible to visualize the evolution of the observable structures during the laser pulse.

In doing so we find a particular representation convenient, that is related to the two-dimensional photoelectron momentum distribution (2dPMD) measured experimentally.

The cylindrical symmetry around the laser polarization axis means that the azimuthal emission angle is irrelevant; when studying the dynamics, we

3.4 LES trajectories in a short pulse

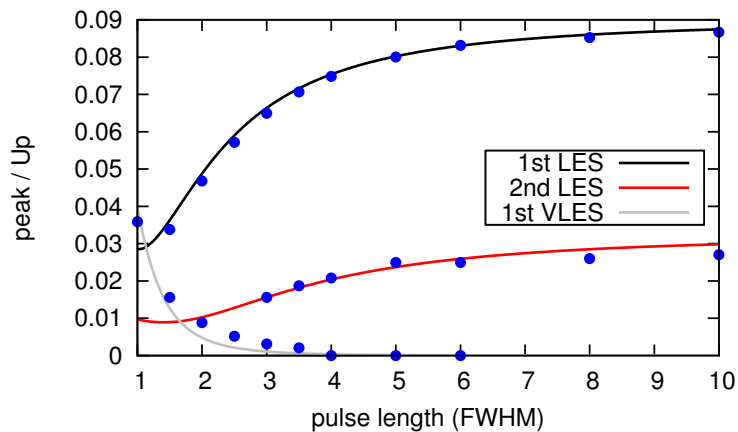


Figure 3.4: Simulation results (dots) compared to theoretical predictions from Eq. (3.7). The laser parameters are $I = 10^{14}$ W/cm², $\lambda = 3.2$ μ m.

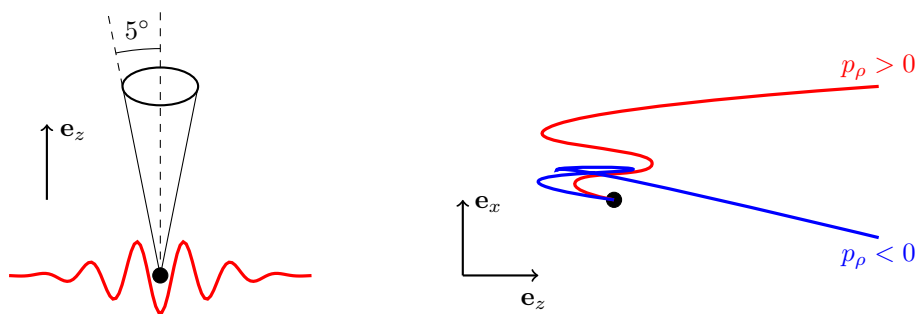


Figure 3.5: Left: The setup for recording a forward direction spectrum with an opening angle of 5° . Right: Sketch of trajectories with final transverse momentum of different sign. For the red trajectory our defined $p_\rho = \mathbf{p} \cdot \mathbf{e}_x > 0$, while for the blue trajectory $p_\rho = \mathbf{p} \cdot \mathbf{e}_x < 0$.

can assume all electrons exit along, say, the x -axis. With proper weighting of the initial conditions (see Appendix C) the cylindrical symmetry is taken into account. Asymptotically in the Coulomb field we always have $\mathbf{p} \cdot \mathbf{e}_\rho \geq 0$. However if we define the initial emission angle as $\varphi = 0$ so that emission is always along \mathbf{e}_x , a trajectory turning around once in the perpendicular direction escapes with $\mathbf{p} \cdot \mathbf{e}_x \leq 0$. See Fig. 3.5. Keeping this sign information helps the physical intuition. We choose however to use the designation p_ρ instead of p_x in our results since this draws attention to the cylindrical symmetry of the problem, and the fact that we take all electrons with the proper weighting into account.

Physically it is impossible to distinguish if a specific final momentum is due to an initial momentum in that direction, or if there was one, or multiple, changes of sign in p_ρ during the motion. From the simulation results with negative p_ρ , the observable 2dPMD is recovered by simply overlaying the negative and positive parts, i.e. $P_{\text{exp}}(p_\rho) = P_{\text{sim}}(p_\rho) + P_{\text{sim}}(-p_\rho)$.

Fig. 3.6 illustrates the evolution of this distribution during a six cycle laser pulse at 2 μm . Ionization is restricted to the central cycle for figure (a) to (c). Structures are seen to emerge according to the possible recollision times in the model. The top panels show the distribution of momentum in the polarization direction - the marginal spectrum in z -direction (cf. Appendix A.2).

Particularly interesting is that the VLES recollision, while giving only a weak contribution to the final spectrum in (d), is very pronounced during the laser pulse. In e.g. discussing probability of high energy ATI or HHG, where the probability distribution during the pulse is important, it may be necessary to take it into account.

In the realistic final result with ionization throughout the pulse and including the asymptotic motion after the laser pulse is over, only the 1st LES is clearly seen, while higher order LES and a trace of the VLES pile up at a small offset from zero, creating the double hump structure [59] in the longitudinal spectrum.

The details of the structures of Fig. 3.6 will be analyzed in Chapters 4 and 5.

3.5 Comparison with experiment

The scaling of the 1st order LES peak with pulse length was investigated experimentally, in a collaborative work [7]. The results confirm the overall scaling properties for a number of different species and laser parameters, illustrating the universality of the process. Before discussing the results it is necessary to make the connection to the experimental setting, where the laser intensity is not fixed throughout the experimental chamber.

3.5.1 Focal averaging

In comparing theoretical results in the strong-field area with experimental ones, one must always take into account that the focus of a laser beam does not only contain one single intensity; see Section 2.2.2. According to previous sections the energy of the LES peaks scales linearly with the intensity via the ponderomotive energy: $E_{\text{LES}} \sim U_p \sim I$. The single-intensity results of previous sections must be modified before they are compared to actual experimental results.

3.5 Comparison with experiment

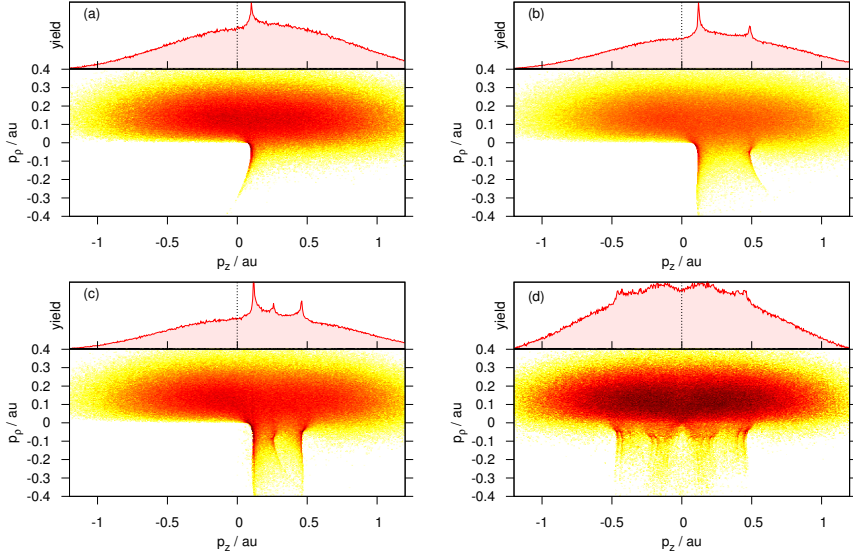


Figure 3.6: Development of VLES and LES features during the laser pulse. (a) After 1 full cycle, the 1st VLES is forming. (b) After 1.5 cycles, the 1st LES turns up. (c) After 2.5 cycles, an additional VLES (almost on top of the first) and the 2nd LES has formed. (d) Realistic final result. $I = 10^{14}$ W/cm², $\lambda = 2$ μ m.

The laser focus is described by the Gaussian beam of Section 2.2.2. The volume of each differential isointensity shell within the full focus is given by Eq. (2.8). It is convenient to rewrite this as a distribution in relative intensity, setting $i = I/I_0$ and disregarding prefactors

$$\frac{dV}{di} \sim i^{-5/2}(2i+1)\sqrt{1-i}. \quad (3.12)$$

We are interested in predicting the drift momentum of the LES/VLES. As discussed in Section 3.4 the peak momentum will approximately coincide with the peak from the center half-cycle, with the other cycles simply broadening the peak. It therefore suffices to consider ionization from the center half-cycle to get the dominant momentum.

We use the quasi-static ionization rate Eq. (2.10). Combining Eq. (3.12) and Eq. (2.10) gives the ionization rate for each intensity

$$w(i) \sim \exp\left(-\frac{2}{3\mathcal{F}_0\sqrt{i}}\right) i^{-3}(2i+1)\sqrt{1-i} \quad (3.13)$$

where

$$\begin{aligned} \mathcal{F}_0 &= F_0/(2I_p)^{3/2} \\ i &= I/I_0 = F^2/F_0^2 \end{aligned}$$

The shape of Eq. (3.13) depends on the single parameter \mathcal{F}_0 , the maximum of the reduced field strength.

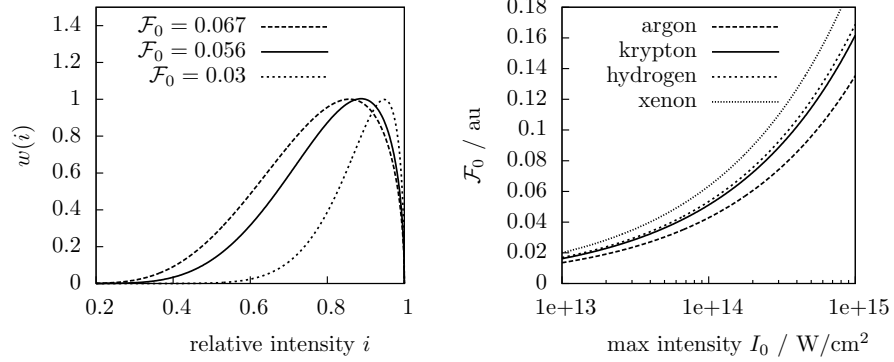


Figure 3.7: Left: $w(i)$ from Eq. (3.13) for $\mathcal{F}_0 = 0.056$, $\mathcal{F}_0 = 0.067$, and $\mathcal{F}_0 = 0.03$. Right: \mathcal{F}_0 for different atomic species, as function of central intensity I_0 .

Fig. 3.7 shows plots of Eq. (3.13) (normalized to the peak value) for a few different values of F_0 , as well as values of \mathcal{F}_0 for a few different atomic species, as function of intensity. Consider an idealized recollision process, where only a single, definite energy value is contributing. The final energy distribution coming from a single intensity should then be a δ -function. The focal averaged peak then gets the same shape as Eq. (3.13), shown in Fig. 3.7. The peak location in the result is then the non-averaged result multiplied by some factor $\alpha = \alpha(\mathcal{F}_0)$, which can be gained by extracting the peak from Eq. (3.13).

3.5.2 Approximate model for LES averaging

In order to avoid a numerical treatment for each field strength, we look for a simplification of the full expression of the average intensity. It turns out to be easiest to start from the expression in normalized field strength $f = \mathcal{F}/\mathcal{F}_0$:

$$w(f) \propto \exp\left\{-\frac{2}{3\mathcal{F}_0 f}\right\} \frac{2f^2 + 1}{f^5} \sqrt{1 - f^2}.$$

The average field strength of the LES peak is then given by

$$\bar{f} = \frac{\int_0^1 df f w(f)}{\int_0^1 df w(f)} \quad (3.14)$$

By defining $x \equiv 2/3\mathcal{F}_0$ we can rewrite this as

$$\bar{f} = \left(-\frac{d}{dx} \ln Q(x)\right)^{-1} \quad (3.15)$$

with

$$Q(x) \equiv \int_0^1 df f w(f).$$

It is now useful to set $f = 1/y$ thus getting

$$Q(x) = \int_1^\infty dy y^{-2} y^{-1} e^{-xy} \frac{2y^{-2} + 1}{y^{-5}} \sqrt{1 - y^{-2}} = \int_1^\infty dy e^{-xy} \frac{2 + y^2}{y^{-1}} \sqrt{y^2 - 1}.$$

3.5 Comparison with experiment

Since the parameter x is typically quite large $x \approx 10$, the integrand will quickly go to 0 as y is increasing. Keeping the exponential factor, we expand the rest of the integral in $\sqrt{y-1}$ around $y = 1$:

$$(2/y + y)\sqrt{y+1}\sqrt{y-1} \approx 3\sqrt{2}\sqrt{y-1} \text{ close to } y = 1$$

so that

$$Q(x) \approx 3\sqrt{2} \int_1^\infty dy e^{-xy} \sqrt{y-1} = 3\sqrt{\pi/2} e^{-x} x^{-3/2}$$

where we used the integral identity

$$\int_1^\infty e^{-xy} \sqrt{y-1} = \sqrt{\pi/2} x^{-3/2} .$$

We can now get the approximate \bar{f} by Eq. (3.15)

$$\bar{f} = -\frac{Q(x)}{Q'(x)} = \frac{1}{1 + 3/(2x)} = \frac{1}{1 + 9F_0/4} .$$

For the LES peaks we can write

$$P(n) = p_\infty(n)/C_{\text{av}}$$

for the n^{th} peak, where

$$C_{\text{av}} = 1 + \frac{9}{4}\mathcal{F}_0 . \quad (3.16)$$

Due to the smallness of \mathcal{F}_0 , this expression can even be linearised without introducing much further error:

$$P(n) \approx p_\infty(n) \approx 1 - \frac{9}{4}\mathcal{F}_0 . \quad (3.17)$$

The focal averaged LES peak energy is accordingly given by $E(n) = E_\infty(n)/C_{\text{av}}^2$ or $E(n) = E_\infty(n)(1 - 9\mathcal{F}_0/4)^2$.

The exact calculation according to Eq. (3.14) is compared with the approximation given by Eq. (3.16) and the linearized version Eq. (3.17) in Fig. 3.8.

We thus have a simple analytical estimate of the change in the LES peak momentum due to the distribution of intensities within the focal volume. It gives an overall decrease in the observed peak momentum, as compared to the one at the fixed maximum intensity, depending only on the reduced field strength at the focal center. Note that a smaller reduced field strength gives a smaller shift of the average, in agreement with the narrower distribution in Fig. 3.7.

The shift does not depend on the pulse length, meaning that the scaling properties described in Section 3.4 remain unchanged.

3.5.3 Experimental result

The experimental results reported in [7] are presented in Fig. 3.9. The theoretical curves are shifted to lower energy by 15%, which was attributed to the

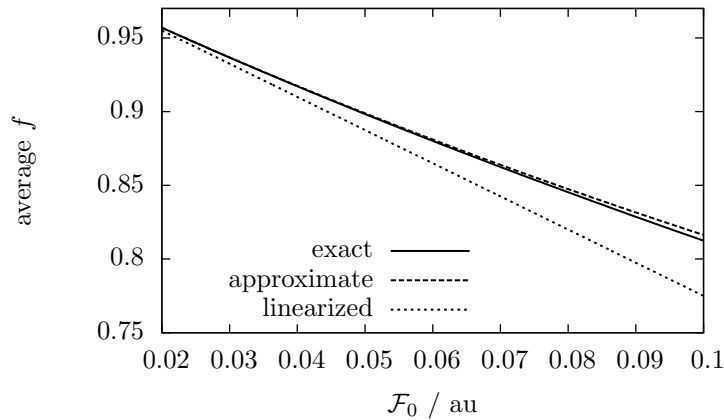


Figure 3.8: Shift of the LES peak momentum as function of \mathcal{F}_0 . Numerically integrated (exact) curve is compared to the approximate expression Eq. (3.16) and the linearized one Eq. (3.17).

inexact determination of U_p in the experiment. The agreement between the analytical curve and the experimental results is very good. This strongly supports that the model described here is an accurate description of the physical process measured in the experiment, showing that classical trajectory arguments can predict the location of the LES peak to an accuracy which is within the experimental resolution (cf. error bars of Fig. 3.9).

An additional shift, due to the energy loss in escaping the Coulomb potential after recollision, was included in Fig. 3.9. The shift was calculated as described in Section 5.2 using the effect of the Coulomb potential at a saddle point trajectory. While not exact, this gave an additional shift of around 5% and yielded the very good agreement of Fig. 3.9.

The detector used in [7] had a lower limit of ~ 0.7 eV, meaning that the VLES and higher order LES could not be observed. These are all located below 0.5 eV, as simulation shows. Confirmation of the scaling of those peaks needs to be done in a future experiment, preferably at longer wavelength giving more resolution to the detailed structure of the peaks. This may also cast light on the VLES peak formation and its relation to the VLES trajectory discussed.

3.6 Conclusions

Using a classical trajectory model one can arrive at simple, analytical expressions for the drift momenta of the LES and VLES in a cw field (Section 3.3), as well as in a short laser pulse (Section 3.4). Comparing the case of a cw field with a short pulse, the LES/VLES momentum is seen to change and depend sensitively on the pulse length. The analytical scaling corresponds well to simulated results, as well as the experimental measurement of [7]. The intensity distribution in the focus can be included in the model, giving a simple overall factor. The model needs small modifications to reproduce the absolute measured values, however the scaling, which is the the main subject of this chapter, is

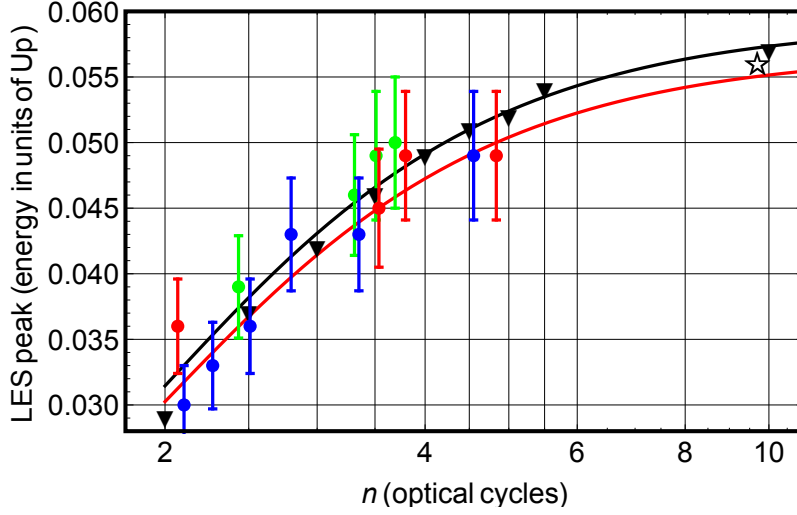


Figure 3.9: The 1st order LES peak energy in units of U_p as function of pulse length. The data is for Krypton $U_p = 20$ eV (green) and $U_p = 25$ eV (blue), and Argon 31 eV (black) and 55 eV (red). Circles are from experiment, triangles from CTMC simulation and lines are analytical results. The star is from the experiment of [5], for Argon at $U_p = 35.6$ eV. Focal averaging is included in the analytical model by means of Eq. (3.16). All theoretical results are shifted down by 15%. From [7].

already described by the original formula Eq. (3.10).

It is our hope that this scaling will be further investigated experimentally, thus confirming or disproving the results presented here. In particular the mechanism behind the VLES has not been identified in experiments yet. The VLES was so far mainly seen as an increase in the spectrum towards threshold. We have tentatively identified this structure with recollision trajectories of a specific type, while pointing out that higher order LES also play an important role in forming the experimental VLES structure. The VLES recollision trajectories have a large influence at the simulated electron momentum distribution during the laser pulse. Using short pulses and possibly altering their shape (e.g. by adding higher harmonics) may make the effect of this recollision measurable. A systematic study of the possibilities lies beyond the scope of this work.

The validity of the classical model rests on sufficiently long excursion distances and travelling times, so that quantum interference between trajectories is negligible. In experiments at intensities around 10^{14} W/cm², this typically holds when $\lambda > 1$ μ m. See e.g. [62]. For shorter distances ATI peaks from a definite number of absorbed photons increasingly dominate the spectrum. On the other hand, for $U_p/2\omega c > 1$, the dipole approximation starts to break down appreciably [12]. For our intensities this happens around wavelengths longer than ~ 3 μ m and will modify the electron trajectories via the Lorentz force. Initially this will only slightly change the shape of the recolliding wave packet, thus not essentially changing the LES process.

Chapter 4

The low energy recollision

In Chapter 3 we studied in detail the classical trajectories (step 2 in the three-step model of Section 3.1) that take part in the low energy recollision. We now proceed to describe the actual rescattering event (step 3). It turns out that the essential features are reproduced by an approximate, analytical model. The model explains how the recollision causes a peak in the spectrum at the corresponding momentum and can also describe the details of the structure, as visible in classical simulations and, to a certain degree, in experiments.

The recollision event has previously been studied to a much lesser extent than the participating strong-field trajectories. The final momentum of the trajectories, and thus the measured result in e.g. [5], can be found just from assuming *some* interaction at recollision, avoiding the details.

In [67] a bunching mechanism was proposed, that leads to a visible peak in the longitudinal momentum spectrum. The model in this chapter is based on the same assumptions but take into account the full dimensionality of the problem, making predictions about the joint distribution (cf. Appendix A.2) of final momenta. From these results, the behaviour of the marginal distributions in both longitudinal and transverse direction can be deduced, as well as the conditional distribution in the forward direction, where the original LES was found. The relations between these observables will also be clarified, referring to the general discussion of Appendix A.

Another proposed mechanism of LES formation is Coulomb focusing, where the transverse force is playing the crucial role [63, 65]. The reasoning is that, upon returning close to the ion, electrons are focused by the interaction, giving an increased probability of motion in forward direction after recollision. While the transverse force does play a role, this model in itself cannot account for the full LES characteristics. We always treat the 2D situation, which is trivially related - by the cylindrical symmetry around the laser polarization axis - to the full physical 3D situation. From our treatment, it is seen that transverse and longitudinal forces both have an important influence on the result, and the final LES can only be said to depend on both (in particular the 2D features), although the bunching process that results in forward motion takes place in a direction that is more longitudinal than transverse, giving that direction some precedence.

It is characteristic of most proposed explanations for the LES that one direction is considered dominant. In [63, 65, 71] it is the transverse one, while

in [67] it is the longitudinal. There is even some confusion about what is actually meant by the LES: is it a caustic in the 2D spectrum [65, 69] or is it a peak in the forward direction [5, 63, 71]?

Misunderstandings and disagreement in the literature on the nature of the interaction seems to stem from these different viewpoints. In particular, several authors have reproduced the LES in the conditional forward spectrum using simulations where the longitudinal component of the Coulomb force was neglected completely. This was taken as an indication for the transverse nature of the LES. Notwithstanding that the 2D momentum distribution is badly reproduced by such a model, and that pure longitudinal Coulomb force also gives an LES (though much weaker), a complete understanding necessarily needs the physical force included in the model. As we see from our model the spherical symmetry of the Coulomb field is a basic property of the problem, and destroying that by artificial means can only give superficial knowledge about the actual process.

We will therefore throughout treat the full dimensionality, and carefully indicate when conclusions are made regarding the various 1D distributions that can be obtained from the 2D one.

The treatment in this and the following chapter contains several ideas from the papers mentioned here. It can be viewed as a generalization of the bunching mechanism of [67] to the 2D distribution. Thus the fully 2D viewpoint of [69] is adopted. At the same time, the caustic formation of [65] is clarified and shown to be qualitatively reproduced by an analytical model. Finally, in the next chapter all conclusions for the forward direction spectrum, as measured and discussed in [5, 62, 63, 71], are drawn.

First the recollision by itself is discussed in Section 4.1. We use approximate recollision trajectories to set up a model where the change in drift momentum at recollision is obtained through the gradient, with respect to the turning point, of a scalar function. Together with the strong field trajectories we can then describe the full dynamics in Section 4.2. Recollisions at specific distance from the ion results in a caustic in the final momentum spectrum, giving the LES and VLES for the respective trajectories. The VLES (Section 4.3) is directly described by the simple model, while for describing the shape of the LES caustic, also motion before recollision is taken into account in Section 4.4. The results of the model then agree well with simulation results.

The analytical treatment used here reproduces the LES features from single recollisions very accurately. However the full effect of the Coulomb potential on the entire electron trajectory is not taken into account. This is done in the following chapter, where a completely numerical treatment is used. The insights from the analytical model are used to easily identify the similar features in the numerical result, contributing to a complete understanding of the phenomenon.

4.1 The recollision model

In Chapter 3 we demanded that low energy recollision trajectories return exactly to the origin with a momentum of exactly zero. Certainly trajectories coming very close to the ion will not give distinct features in the low energy spectrum, since they interact very strongly with the ion and can gain high energies. They are responsible for the high energy ATI plateau described in Section 2.4 and can recombine to generate high harmonics. To get low energies the interaction

needs to be weak and thus the electron turns around some distance away from the ion ("soft recollision" [67]). Given the large length scales involved in the laser driven motion, the approximations of Chapter 3 still give a good first estimate of the momenta of recolliding trajectories. Here we treat the recollision in more detail, where the recollision point \mathbf{r}_C is no longer the origin. Instead its value determines the shift in the drift momentum \mathbf{p} at recollision.

4.1.1 Approximate recollision trajectories

To set up the model we make two assumptions. The interaction process happens within some time interval (t_0, t_2) containing the maximum of a laser cycle at t_1 . Due to the laser driving, the recolliding trajectories typically only spend a short time in the vicinity of the ion, before being accelerated away by the laser field. During this time, the laser field is almost constant. We therefore make the following assumption

$$F(t) \approx F(t_1) \quad \text{during recollision; assumption (i)}$$

where t_1 is the recollision time, defined as in Eq. (3.4) as the instant when $p_z = 0$.

Then we make the approximation that, throughout the scattering process:

$$|F(t_1)| \gg |\mathbf{F}_C(\mathbf{r}(t))| \quad \forall t \in (t_0, t_2), \text{ assumption (ii)}$$

where \mathbf{F}_C is the Coulomb force, evaluated at points \mathbf{r} the trajectory passes during the process. This means that the Coulomb force is very weak compared to that of the laser, so that we can neglect its influence on the trajectory during rescattering. The trajectory follows the same path it would follow without the Coulomb field present, and the field is taken into account by computing its influence along the trajectory, giving a shift in the asymptotic drift momentum. This perturbative approach is similar in spirit to the first-order Born approximation of quantum mechanical scattering theory, where the potential allows scattering between field-free asymptotic states, but does not change these states themselves [11].

The trajectory itself is then given by the strong-field one Eq. (3.1) expanded to lowest order in t :

$$\mathbf{r}(t) \approx \mathbf{r}_C + \frac{F(t-t_1)^2}{2} \mathbf{e}_z \quad \text{where } F \equiv F(t_1) \quad (4.1)$$

The electron follows a trajectory with fixed $\rho = \rho_C$, and motion in z like that in a constant field, with turning point given by z_C .

This model for the recollision trajectories is widely used, e.g. in [63, 67, 80].

4.1.2 The recollision process

Along the trajectory of Eq. (4.1) the influence of the Coulomb potential on the drift momentum \mathbf{p} is calculated by integrating the force over all times (primes denote initial values):

$$\mathbf{p} = \mathbf{p}' + \delta\mathbf{p}(\mathbf{r}_C) \\ \delta\mathbf{p}(\mathbf{r}_C) = \int_{-\infty}^{\infty} \mathbf{F}_C(\mathbf{r}(t)) dt = - \int_{-\infty}^{\infty} \text{grad}_{\mathbf{r}_C} \frac{-1}{|\mathbf{r}(t)|} dt = - \text{grad}_{\mathbf{r}_C} \Phi. \quad (4.2)$$

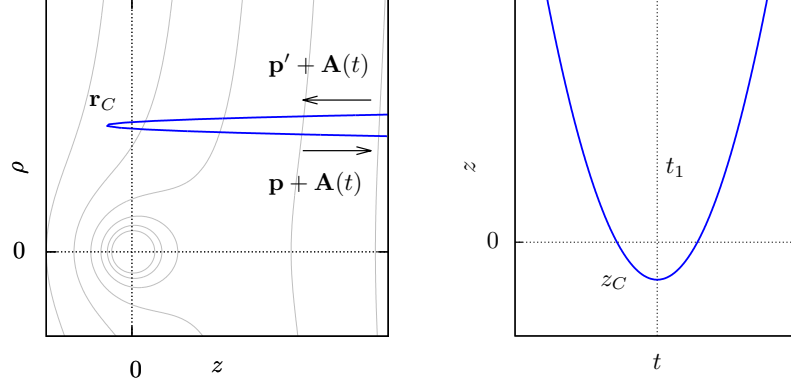


Figure 4.1: Illustration of the recollision model. Left: Change of drift momentum from \mathbf{p}' to \mathbf{p} during the recollision. Contours indicate the combined potential of the ion and the laser. Right: The motion in z -direction is that in a constant field.

For a given field strength, the value of $\delta\mathbf{p}$ is determined by the point of recollision \mathbf{r}_C alone, which itself depends on the initial momentum \mathbf{p}' . We have defined

$$\Phi \equiv \int_{-\infty}^{\infty} \frac{-1}{|\mathbf{r}(t)|} dt. \quad (4.3)$$

The event can be viewed as a kind of potential scattering off the potential $\Phi(\mathbf{r}_C)$, which is the integrated Coulomb potential along the Coulomb-free trajectory with turning point at \mathbf{r}_C . One should however not understand it as a conventional scattering problem, with time dynamics in a potential Φ between in- and out-states, but rather an instantaneous influence of Φ , giving an instantaneous change in drift momentum (=momentum of outgoing state) of the strong-field trajectory. Φ plays the role of a potential, being an object from which a change in the momentum is obtained by taking the gradient.

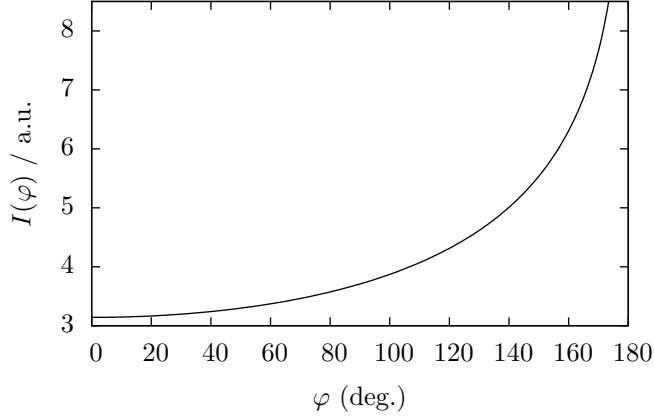
The central object of the classical interaction process is the Jacobian determinant between ingoing and outgoing momenta, cf. Appendix A.3. Using Eq. (4.2) and Eq. (4.3) the full Jacobian can be decomposed into

$$\begin{aligned} J &= \frac{\partial(p_\rho, p_z)}{\partial(p'_\rho, p'_z)} = I + \frac{\partial(\delta p_\rho, \delta p_z)}{\partial(p'_\rho, p'_z)} = I + \frac{\partial(\delta p_\rho, \delta p_z)}{\partial(\rho_C, z_C)} \frac{\partial(\rho_C, z_C)}{\partial(p'_\rho, p'_z)} \\ &= I - H_\Phi(\rho_C, z_C) \frac{\partial(\rho_C, z_C)}{\partial(p'_\rho, p'_z)}. \end{aligned} \quad (4.4)$$

where H_Φ is the Hessian matrix of Φ w.r.t. \mathbf{r}_C .

The study of the recollision process itself is thus reduced to the study of the potential Φ . The final spectrum is in addition influenced by the motion before recollision which enters in the last factor of Eq. (4.4).

We now see the point of writing $\delta\mathbf{p}$ in terms of Φ : the final momentum spectrum depends on its Hessian matrix. The Hessian of any smooth function is a symmetric matrix, so that it can be diagonalized in an orthogonal basis. The structure of the determinant $\det J$ is thus greatly simplified.


 Figure 4.2: The function $I(\varphi)$ of Eq. (4.5).

4.1.3 Properties of Φ

It turns out convenient to change to polar coordinates for the rescattering location

$$\mathbf{r}_C = r(\sin \varphi \mathbf{e}_\rho + \cos \varphi \mathbf{e}_z) .$$

Changing the integration variable to $\xi = t\sqrt{F/2r}$ gives

$$\begin{aligned} \Phi &= - \int_{-\infty}^{\infty} \frac{dt}{|\mathbf{r}_C + Ft^2/2\mathbf{e}_z|} = -\frac{1}{r} \sqrt{\frac{2r}{F}} \int_{-\infty}^{\infty} \frac{d\xi}{\sqrt{\sin^2 \varphi + (\cos \varphi + \xi^2)^2}} \\ &= -\sqrt{\frac{2}{Fr}} \int_{-\infty}^{\infty} \frac{d\xi}{\sqrt{1 + 2 \cos \varphi \xi^2 + \xi^4}} \equiv -\sqrt{\frac{2}{Fr}} I(\varphi) . \end{aligned}$$

Φ factorizes into one function of the radial recollision distance r , and one function of the recollision angle φ . $I(\varphi)$ is an elliptic integral, which can be written as

$$\begin{aligned} I(\varphi) &= 2(1 + \lambda)F(\arctan \lambda^{-1/2}|1 - \lambda^2) \\ \lambda &= \frac{1 - \sin \varphi/2}{1 + \sin \varphi/2} \end{aligned} \quad (4.5)$$

where F is the standard elliptic integral of the first kind [78]. This is mainly useful for deriving a few special values, since the analytic expressions of derivatives of $I(\varphi)$ are cumbersome.

Explicit expressions for the elements of the Hessian H_Φ are given in Appendix B. The factor structure of Φ is preserved in derivation; its final form is

$$H_\Phi = -\sqrt{\frac{2}{F}} \frac{1}{r^{5/2}} G(\varphi) \quad (4.6)$$

with $G(\varphi)$ a symmetric matrix. Diagonalizing H_Φ reduces to finding a rotation angle $\theta(\varphi)$ which diagonalizes the matrix $G(\varphi)$.

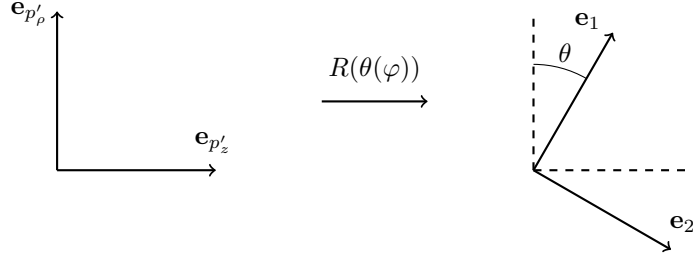


Figure 4.3: Definition of basis vectors \mathbf{e}_1 and \mathbf{e}_2 by rotation by $(\varphi$ -dependent) angle θ .

4.2 Dynamics

So far we only discussed the recollision process itself, studying the momentum change as function of recollision position. We now include the initial motion before recollision, giving a relation between final and initial momentum.

4.2.1 Diagonalization of the full Jacobian

In the real situation, the evolution before the LES recollision is non-trivial, leading to complexities in the final spectrum which do not result from the recollision alone. In order to focus on the recollision event, we assume that the collision point depends linearly on the initial momentum, as in the strong-field dynamics of the three-step model:

$$\begin{aligned} \rho_C(p'_\rho, p'_z) &= \tau p'_\rho + b_1 \\ z_C(p'_\rho, p'_z) &= \tau p'_z + b_2 \end{aligned} \quad (4.7)$$

with τ the recollision time and $b_{1,2}$ arbitrary constants. For e.g. the 1st order LES, $\tau = 3\pi/\omega$, cf. Eq. (3.4). From Eq. (4.7) follows

$$\frac{\partial(\rho_C, z_C)}{\partial(p'_\rho, p'_z)} = \tau I$$

with I the unity matrix. This gives with Eq. (4.4)

$$J = \frac{\partial(p_\rho, p_z)}{\partial(p'_\rho, p'_z)} = I - \tau H_\Phi = I + \sqrt{\frac{2}{F}} \frac{\tau}{r^{5/2}} G(\varphi) .$$

J is diagonalized by the same rotation $\theta(\varphi)$ of the basis as that diagonalizing $G(\varphi)$. Note that the matrix G is completely general; laser intensity and wavelength are contained only in the prefactors. Denoting the eigenvalues of G by $\mu_{1,2}(\varphi)$, we get the following expression for the Jacobian determinant

$$\det J = \left(1 + \sqrt{\frac{2}{F}} \frac{\tau}{r^{5/2}} \mu_1(\varphi) \right) \left(1 + \sqrt{\frac{2}{F}} \frac{\tau}{r^{5/2}} \mu_2(\varphi) \right) \equiv \lambda_1 \lambda_2 . \quad (4.8)$$

It is immediately seen that changing the laser parameters and the recollision radius such that

$$\sqrt{\frac{2}{F}} \frac{\tau}{r^{5/2}}$$

is held constant, the determinant expression at a certain recollision angle φ does not change. We can thus map a change in laser parameters to a change in recollision distance where a certain spectral value is obtained. If the determinant vanishes (as turns out to be the case), this is caused by recollision at a specific (φ -dependent) r , which when changing the laser parameters scales as

$$r \sim \frac{\tau^{2/5}}{F^{1/5}} \sim \frac{1}{(F\omega^2)^{1/5}}.$$

τ depends here on the period of the laser, as for recollision after a fixed number of cycles. This weak scaling with respect to the laser parameters signifies that the model is reliable for a large range of parameters. Changing the laser intensity or wavelength only adjusts a little the radial distance at which recollision must occur, in order to give rise to a certain spectral feature. The *drift* momentum may change significantly, but the recollision process itself stays very similar.

4.2.2 Formation of the LES

Fig. 4.4a shows the eigenvalues $\mu_{1,2}(\varphi)$ of the matrix $G(\varphi)$. Since $\mu_1 > 0$ it follows that always $\lambda_1 > 1$, so that in the direction \mathbf{e}_1 associated with λ_1 there is reduction of spectral weight ("anti-bunching"). Along \mathbf{e}_2 however there is bunching for $\varphi < 163^\circ$, since $\mu_2 < 0$ thus $\lambda_2 < 1$. In particular there is complete bunching if

$$\lambda_2 = 0 \implies r = \left(-\sqrt{\frac{2}{F}} \tau \mu_2(\varphi) \right)^{2/5} \quad (4.9)$$

giving rise to a critical line. By Appendix A.5 it results in a caustic in the final spectrum. The fact that $\lambda_2 = 0$ means that, moving in the space of initial coordinates (the (p'_ρ, p'_z) -plane) in the direction of the eigenvector \mathbf{e}_2 associated with λ_2 , the final momentum (p_ρ, p_z) does not change (to first order), causing the divergent spectrum. We can say that there is complete "bunching" in the direction \mathbf{e}_2 .

Fig. 4.4b shows the rotation angle θ that diagonalizes $G(\varphi)$ and J . At $\varphi = 0$, i.e. recollision at positive z with $\rho = 0$, it is equal to $\theta = 90^\circ$, meaning the bunching eigenvalue λ_2 acts along the original ρ -coordinate. At $\varphi = 116.5$, it is zero giving bunching purely along z .

Fig. 4.5a shows for illustration the eigenvalues $\lambda_{1,2}(r, \varphi)$ for the parameters $\tau = 3\pi/\omega$ (1st order LES), $\omega = 0.0228$ au ($\lambda = 2$ μm) and $F = 0.0534$ au ($I = 10^{14}$ W/cm²) at recollision radius $r = 20$ au. Since μ_2 is almost constant for a large range of angles φ , the condition $\lambda_2 = 0$ will be fulfilled for almost the same r for these angles. Fig. 4.5b shows the radius of the recollisions giving $\lambda_2 = 0$, given explicitly by the expression Eq. (4.9), for the same parameters. It is seen to stay within a narrow range of ≈ 25 au until some 140° , where it drops off sharply. Since $\mu_2(0) = -3\pi/8$ (see Appendix B) the 1st order LES recollisions with $\rho = 0$ gives a vanishing determinant at the recollision distance

$$r = z = \left(\sqrt{\frac{2}{F}} \tau \frac{3\pi}{8} \right)^{2/5} = \left(\sqrt{\frac{2}{F}} \frac{9\pi^2}{8\omega} \right)^{2/5} \approx \frac{3}{(F\omega^2)^{1/5}}. \quad (4.10)$$

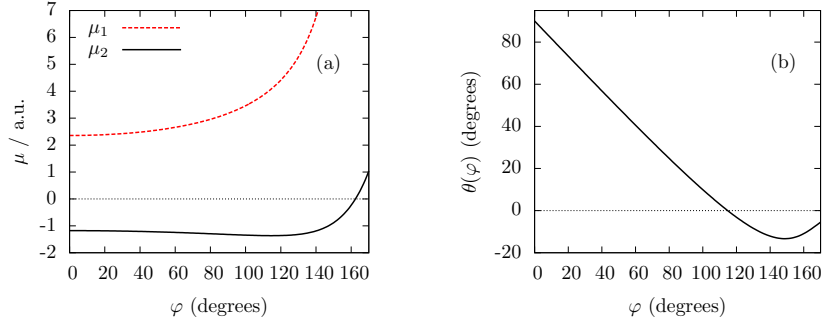


Figure 4.4: (a) The two eigenvalues of the matrix $G(\varphi)$ of Eq. (4.6). (b) The rotation angle $\theta(\varphi)$ diagonalizing $G(\varphi)$.

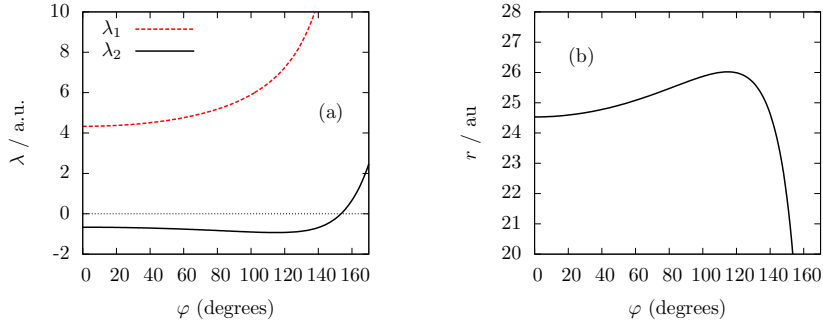


Figure 4.5: (a) Example of eigenvalues of the full Jacobian J at $r = 20$, for laser parameters $\tau = 3\pi/\omega$, $\omega = 0.0228$ au and $F = 0.0534$ au. (b) The recollision radius $r(\varphi)$ yielding the critical line, given by Eq. (4.9).

Since the recollision radius r changes little with the recollision angle φ , especially in the first quadrant (cf. Fig. 4.5b), Eq. (4.10) can be used for a first estimate for the distance of the critical recollision from the ion.

Fig. 4.6 shows the two eigenvalues of the problem as functions of the turning point \mathbf{r}_C , using (4.7) with $\tau = 3\pi/\omega$, $\omega = 0.0228$ au. The critical line, defined by $\lambda_2 = 0$, is marked in red.

4.2.3 The deflection function, the critical line and the caustic

Writing the final momentum as function of the initial ones gives the so-called deflection functions $p_\rho(p'_\rho, p'_z)$ and $p_z(p'_\rho, p'_z)$, which give an illuminating picture of the full dynamics. They are obtained by means of Eq. (4.2) and plotted simultaneously as contour plots in Fig. 4.7, for the parameters of Fig. 4.6. The critical line, obtained by the condition Eq. (4.9) together with $\mathbf{r}_C = \mathbf{p}'\tau$, is shown in blue. It indicates the points where $\text{grad } p_\rho \parallel \text{grad } p_z$ and clearly runs through the visible saddle point in p_z , cf. Appendix A.5.

The shape of the caustic is determined by the expression Eq. (4.2), for initial values \mathbf{p}' belonging to the critical line, i.e. fulfilling Eq. (4.9). Due to the weak

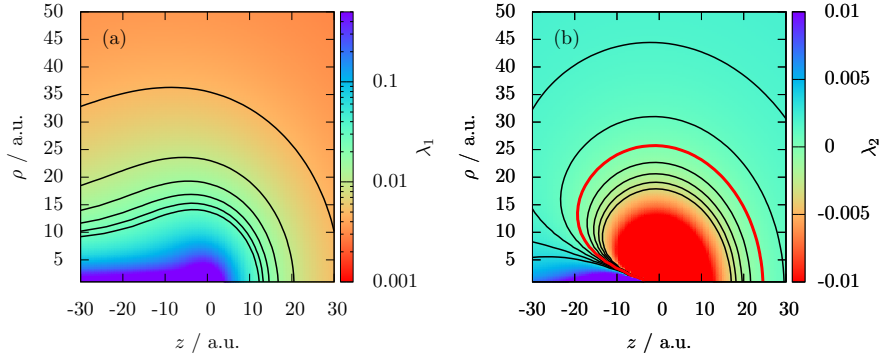


Figure 4.6: The eigenvalues λ_1 (a) and λ_2 (b) of Eq. (4.8) as functions of (ρ_C, z_C) . For better visibility λ_1 is shown on a logarithmic scale. Laser parameters $\tau = 3\pi/\omega$, $\omega = 0.0228$ au and $F = 0.0534$ au. The critical line is marked in red in (b).

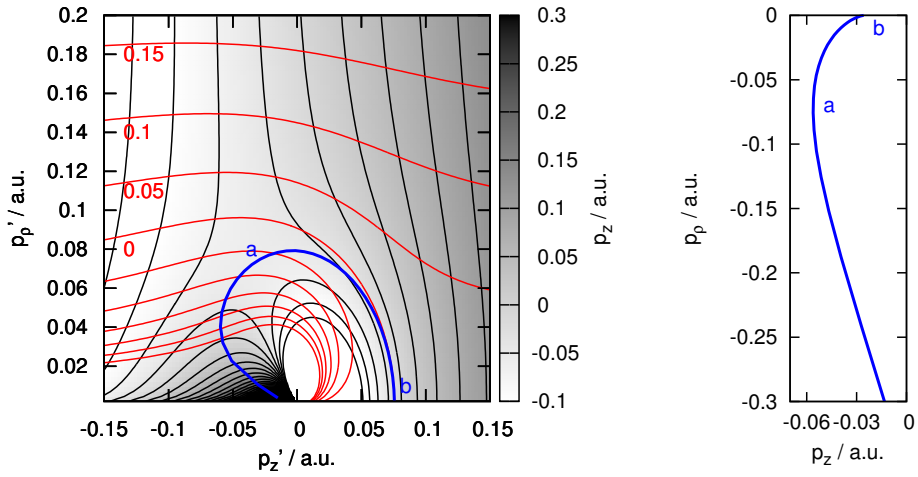


Figure 4.7: Left: The deflection functions for the recollision model of Section 4.2. Black contour lines and shading: p_z , red contour lines with labels: p_ρ . The critical line is shown in blue. Right: The shape of the caustic in the final momentum spectrum. Letters show the corresponding initial and final values; (a) marks a saddle point in p_z . Laser parameters as in Fig. 4.6.

dependence of Eq. (4.9) with the laser parameters, the shape has universal features and only slightly change for different parameters. Fig. 4.7b shows the shape of the caustic.

4.2.4 Conclusion

The scattering process itself is approximated by using the electron trajectories Eq. (4.1) and the momentum shift at interaction Eq. (4.2). This leads to a model of "instantaneous" potential scattering, which is diagonalizable. Using simplifying assumptions Eq. (4.7) the whole process, from initial momentum to final, can be described in an analytical, diagonalizable way. The diagonalization reveals that one eigenvalue vanishes at a certain line \mathbf{r}_C of recollision positions, and the corresponding line in initial momentum. This means that the spectral determinant is zero there, giving a caustic structure in final 2D joint momentum spectrum. Within the model, analytical expressions for both the critical line of initial momentum and the shape of the caustic in final momentum can be obtained.

4.3 VLES recollision

For the first order VLES recollision, taking place after one full laser cycle, Eq. (4.7) holds to a high degree of accuracy. The Coulomb potential at the tunneling exit focuses the momentum distribution in the ρ -direction; this effect is very small and neglected here [61]. Including the tunneling exit point which can be approximated as $z_0 \approx -I_p/F_0$, we get the recollision position:

$$\begin{aligned}\rho_C &= p'_\rho \tau \\ z_C &= p'_z \tau - z_0\end{aligned}$$

which has exactly the structure of Eq. (4.7). Thus the results of previous sections carry over unchanged. The VLES recollides however when the field in Eq. (4.1) is negative and the trajectory comes from negative z , so that the previous situation is mirrored around the $z = 0$ axis. The shape of the caustic is the mirror image of that found in Fig. 4.7.

This model is compared to numerical simulations in Fig. 4.10 together with the LES model.

4.4 LES recollision

The first order LES process is more complicated due to the motion before the recollision.

We limit the initial discussion to the first order LES trajectory in a cw field, in order to make the essential features apparent. The recollision event by itself is similar in higher order collisions, but analytical estimates are increasingly complicated. The aim of the analytical discussion is not to make exact predictions for all cases, but to give an intuitive understanding of the physical process.

The actual behaviour of classical recolliding trajectories needs to be treated first.

4.4.1 Transverse momentum change at pass by the core

The 1st order LES trajectory passes by the core exactly once before recolliding, see Fig. 4.8. The momentum change due to the pass $\delta p_\rho^{(\text{pass})}$ can be estimated in the following way.

Since the recollision takes place after three half-periods, the fly-by takes place after three quarter-periods $t_p = \tau/2 = 3\pi/2\omega$. At this instant the laser field is $F = F_0 \cos(3\pi/2) = 0$, so the situation is that of Rutherford scattering of a charged particle off an ion. The electron thus follows a hyperbolic Kepler orbit. For the situation of Fig. 4.8, the following holds [81]

$$L = d\sqrt{2E}$$

$$\tan \frac{\theta}{2} = \frac{1}{L\sqrt{2E}} = \frac{1}{2Ed}$$

d is the point of intersection of the asymptotic motion before and after deflection, θ the deflection angle, L is the angular momentum and E the energy. d can be assumed to lie on the ρ -axis, which does not introduce a major error since the electron motion is almost parallel to the z -axis. We write the velocity in z -direction as $v_z = p'_z + A(t_p)$. We then have

$$d = p'_\rho t_p$$

$$L = v_z d = v_z p'_\rho t_p$$

$$E = \frac{p_\rho'^2 + v_z^2}{2} - \frac{1}{d} \approx \frac{v_z^2}{2}$$

since $v_z \gg p'_\rho$ and d is assumed to be far enough from the ion so that $\delta p_\rho^{(\text{pass})}$ is just a small perturbation. Thus

$$\tan \frac{\theta}{2} = \frac{1}{2Ed} = \frac{1}{v_z^2 p'_\rho t_p}$$

Since we are looking at small scattering angles θ we use $\tan x \approx x$ to get

$$\theta = \frac{2}{v_z^2 p'_\rho t_p}$$

and, using once more the smallness of θ , the transverse momentum after scattering is found to be

$$p'_\rho + \delta p_\rho^{(\text{pass})} = p'_\rho \cos \theta - v_z \sin \theta \approx p'_\rho - v_z \theta = p'_\rho - \frac{2}{v_z p'_\rho t_p}$$

v_z is known from Eq. (3.5) to be $v_z \approx A_0(1 + 2/(3\pi))$ with $A_0 = F_0/\omega$.

The higher order LES trajectories pass by the core several times, making further corrections necessary. Since the times $t_p^{(i)}$ of the i^{th} passage are given by the Eq. (3.2) setting $z(t_p^{(i)}) = 0$, and the momentum $p_z(t_p^{(i)})$ is also known, it is possible to compute the corrections $\delta p_\rho^{(i)}$ at each pass. We thus can write

$$p_\rho^{(i+1)} = p_\rho^{(i)} + \delta p_\rho^{(i)} = p_\rho^{(i)} - \frac{2}{p_z^{(i)} d^{(i)}} \quad \text{with } p_\rho^{(1)} = p'_\rho$$

$$d^{(i+1)} = d^{(i)} + p_\rho^{(i+1)}(t_p^{(i+1)} - t_p^{(i)}) \quad \text{with } d^{(0)} = 0 \text{ and } t_p^{(0)} = 0. \quad (4.11)$$

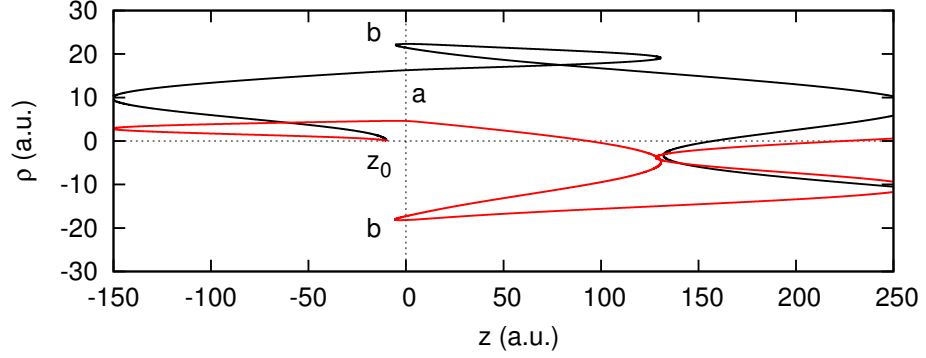


Figure 4.8: Two kinds of LES trajectories. The tunnel exit is at z_0 , the transverse momentum change (fly-by) happens at a , and the LES soft recollisions at b .

4.4.2 Recollision model

We get for the 1st order LES recollision location

$$\rho_C(p'_\rho, p'_z) = \tau p'_\rho + \delta p_\rho^{(\text{pass})} \tau / 2 = p'_\rho \tau - \frac{2}{A_0(1 + 2/(3\pi))p'_\rho} \quad (4.12)$$

$$z_C(p'_\rho, p'_z) = \tau p'_z - \frac{2F}{\omega^2} - z_0 = \tau(p'_z - p_{\text{LES}}) - z_0 \quad (4.13)$$

where p_{LES} is the 1st order LES momentum from Eq. (3.5).

There is a qualitative difference to the VLES model, since the pass by the core can change the sign of p_ρ , so that recollision can happen on either side of the core; see Fig. 4.8. Thus the caustic will consist of two parts, one from recollision at positive ρ_C , one at negative. (We adapt here the viewpoint of Section 3.4.5 and let also the radial position be negative.) The two parts are almost mirror images of each other since the recollision event itself is symmetric in ρ_C ; only slight changes due to the different kind of recollision trajectories occur. This approximate mirror symmetry is not around $p_\rho = 0$, but around that p_ρ which gives $\rho_C = 0$. Since for $\rho_C = 0$ no transverse force is acting during the recollision, for this specific trajectory $\delta p_\rho = 0$. The required value of p'_ρ is easily found from Eq. (4.12):

$$\rho_C = 0 \implies p'_\rho = \sqrt{\frac{2}{A_0(1 + 2/(3\pi))\tau}} = \omega \sqrt{\frac{2}{F_0(3\pi + 2)}} \quad (4.14)$$

Since $\delta p_\rho = 0$ it follows that $p_\rho = -p'_\rho$. Eq. (4.14) thereby predicts the (negative) final transverse momentum p_ρ of a 1st order LES trajectory recolliding at $\rho_C = 0$.

The second term in ρ_C in Eq. (4.12) makes the expression for the Jacobian J cumbersome. It is no longer diagonal. We can still use Eq. (4.12) and Eq. (4.13) to compute the deflection function, and then use a numerical root finding in order to find the zeroes of $\det J$. The deflection function and caustic is shown in Fig. 4.9. In addition to the splitting into two parts, centered around the value given by Eq. (4.14), there are two additional cusps being formed in the caustic.

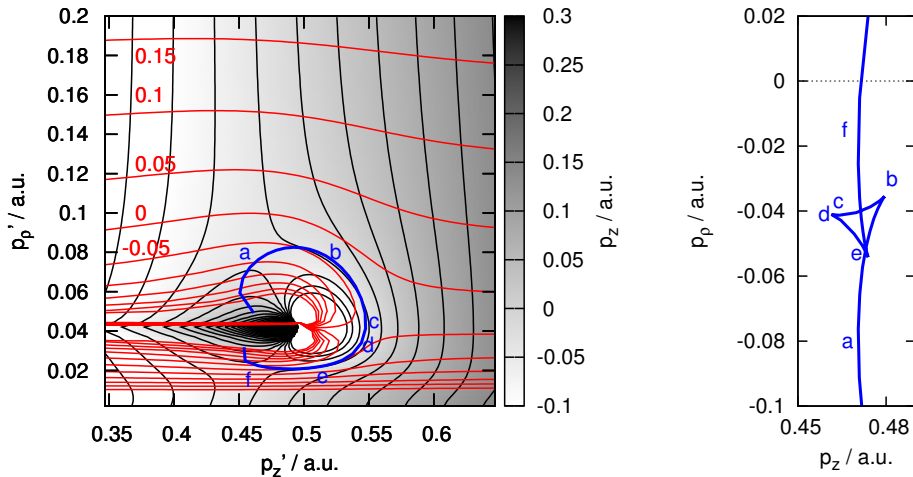


Figure 4.9: Left: The deflection functions for the analytical LES model of Section 4.4, including a pass by the core. Black contour lines and shading: p_z , red contours with labels: p_ρ . The critical line is shown in blue. Right: The shape of the caustic. Letters show the corresponding initial and final values at the saddle points in p_z (a, f), the saddle point in p_ρ (c) and the three cusps (b, d, e).

For a more general discussion of the relation between features in the deflection function and the shape of the caustic, see Appendix A.5.

The analytical caustics obtained within this model is compared to full numerical CTMC simulation results in Fig. 4.10. They agree with the numerical result to a surprising accuracy, given the coarse-looking assumptions underlying the trajectory model. A few contributing trajectories are shown at the rescattering event in Fig. 4.11, together with the critical \mathbf{r}_C from the model, which is clearly an excellent estimate of the numerical turning point position. For comparison the symmetrized line from the simple model is shown, which is accurate enough to give a good estimate of the recollision position.

4.5 Conclusions

The low energy recollision causing the LES has been analyzed in detail. The trajectory model with the approximations Eq. (4.1) and Eq. (4.2) allows one to disentangle the contributions to the final spectrum. In particular the recollision process by itself, described in Section 4.2, is diagonalizable. In the initial phase space we can study its two eigenvalues, the product of which gives the final spectral weight of that phase space point. It is seen that one eigenvalue dominates the process. The fact that this eigenvalue is zero for a line of initial conditions gives a caustic in the final joint momentum distribution, like in the general case of Appendix A.5.

The VLES caustic is formed directly by the diagonalizable model. The LES caustics are more complicated due to the dynamics before recollision. This gives a caustic with two extending lines, almost symmetric around a certain p_ρ -value,

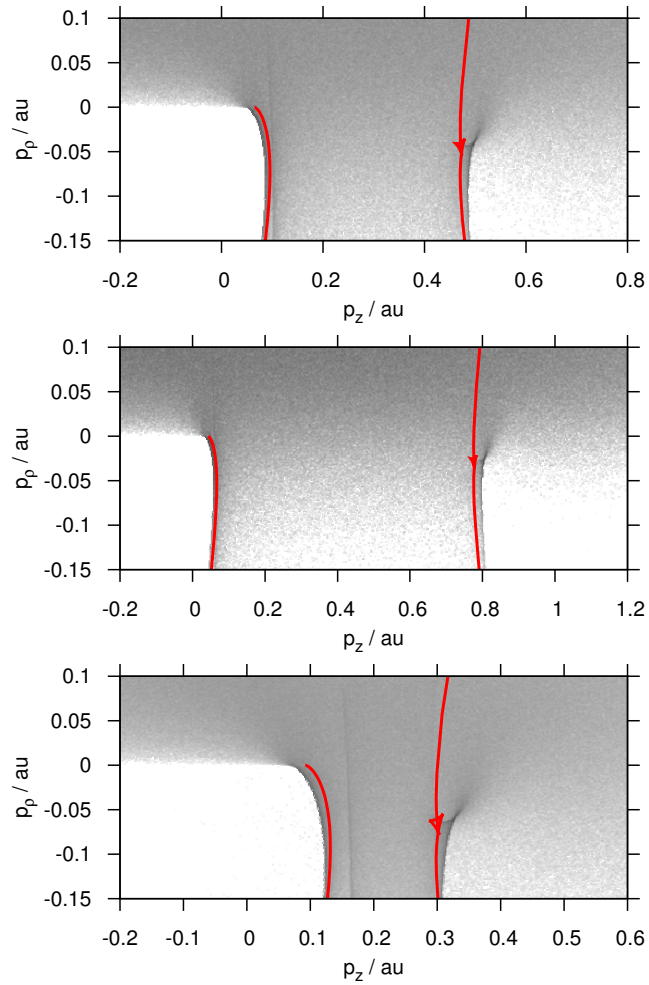


Figure 4.10: Comparison of numerical result and analytical caustic shape (red), for (a) $\lambda = 2 \mu\text{m}$, (b) $\lambda = 3.2 \mu\text{m}$ and (c) $\lambda = 1.32 \mu\text{m}$; intensity 10^{14} W/cm^2 . The VLES is well reproduced; for the LES the analytic caustic reproduces all qualitative features and gives a good quantitative estimate.

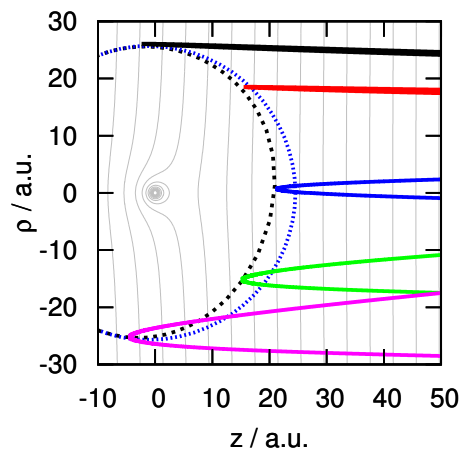


Figure 4.11: Numerical recolliding trajectories contributing to the 1st LES caustic in Fig. 4.10b. The dashed line shows the predicted critical recollision points according to the complete model; the dotted line according to the simple model of Section 4.2, with symmetrization around $\rho = 0$. The complete model gives an excellent approximation of actual recollision positions, while the simple model gives a good first estimate.

and three cusps.

Due to the weak scaling of the whole recollision process with laser parameters (Eq. (4.9)) the model is equally valid for a large range of parameters, as testified by Fig. 4.10. Therefore it gives reliable results in the whole parameter range where the trajectory model is valid, cf. Chapter 3.

Chapter 5

Realistic LES collision

In this chapter the insight gained from the model in Chapter 4 is used to understand photoelectron spectra from full numerical simulations. The assumption of a quantum mechanical tunneling process followed by classical motion is still made, but no approximations are made regarding the classical motion, which is solved numerically (see Appendix C). Details of the tunneling process are not important, since they only modify the weight of initial conditions of classical motion. Furthermore, a semiclassical treatment, where a quantum mechanical phase is included, still contains the classical motion as a starting point, so that the prominent classical features we find should still leave traces in a fully quantum mechanical treatment.

Like in Chapter 4 we investigate how spectral features develop by studying the Jacobian, and we will discuss the different spectra obtained. The joint distribution and the formation of the LES caustic is described in Section 5.1, referring to the model of Section 4.4. Then the marginal distributions in longitudinal and transverse directions are treated in Section 5.2.

Particular focus is on the conditional forward spectrum, treated in Section 5.3, since this is the measurement where most LES work - experimental and theoretical - was hitherto focused. We use a numerical diagonalization of the Jacobian to obtain information about this process. Specifically, the question of which force direction - longitudinal or transverse - dominates, can be given a definite meaning. At the same time it is shown to be only of small interest; the problem is really a 2D one.

One single set of laser parameters is investigated to large detail, in order to clarify the understanding. In Section 5.4 simulations are included for different parameters that show qualitatively similar behaviour. As seen in Section 4.2 the recollision depends little on the laser parameters, so that all cases are qualitatively similar. By including focal averaging, numerical spectra are shown that directly correspond to measured ones, making it clear how the ideal recollision features show up in a real situation.

5.1 The joint spectrum

The numerical deflection function for a laser wavelength of $\lambda = 2 \mu\text{m}$, intensity 10^{14} W/cm^2 and pulse length of 3 cycles (FWHM) is shown in Fig. 5.1. See

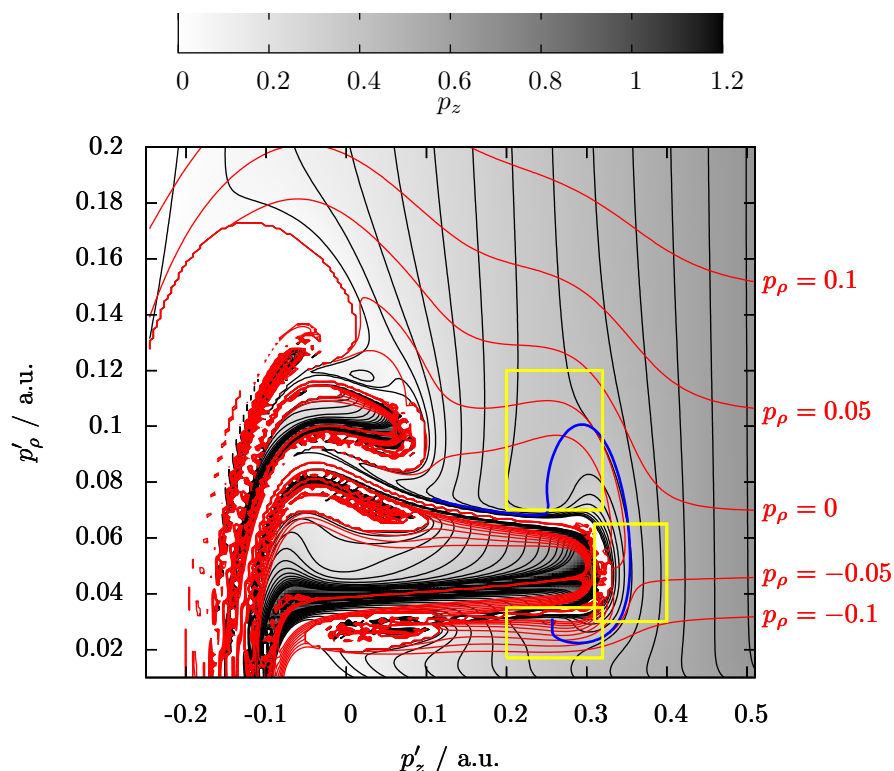


Figure 5.1: Deflection functions $p_\rho(p'_\rho, p'_z)$ (red) and $p_z(p'_\rho, p'_z)$ (black). $I = 10^{14}$ W/cm², $\lambda = 2 \mu\text{m}$, 3 cycle pulse, argon target. The critical line is indicated by the blue line. Details of the areas within yellow rectangles are shown in Fig. 5.2.

Appendix C for a description of the computational method used. There is a large white area to the left in the figure, where no electrons can escape to the detector; these are the FTI electrons. The main recollision feature (around $p'_z = 0.3$ au, $p'_\rho = 0.05$ au) looks rather similar to Fig. 4.9. In the "hard" recollision region, where contour lines are very dense, the dynamics is essentially chaotic [63, 77]. This region gives contributions to the whole spectrum, but is only visible when the non-chaotic background is very weak, that is, for high energies (ATI plateau). For the low energy part of the spectrum we can simply disregard the chaotic contributions. The regular part gives the major contribution to the LES and will easily drown any weak chaotic features in the spectrum.

The deflection function clearly indicates that there are two saddle points (and two maxima) in p_z , and one saddle point in p_ρ , see Fig. 5.2. The critical line (shown in blue) runs through all these points, as necessary (cf. Section A.5.1).

The final momentum distribution is shown in Fig. 5.3. In accordance with the general discussion of Appendix A.5 the critical line shows up in the final 2D momentum spectrum as a caustic. Its exact shape depends on the laser parameters in a nontrivial way. Characteristically it is however mainly visible for negative p_ρ (see Section 3.4.5 for the interpretation of the sign of p_ρ). These are

5.1 The joint spectrum

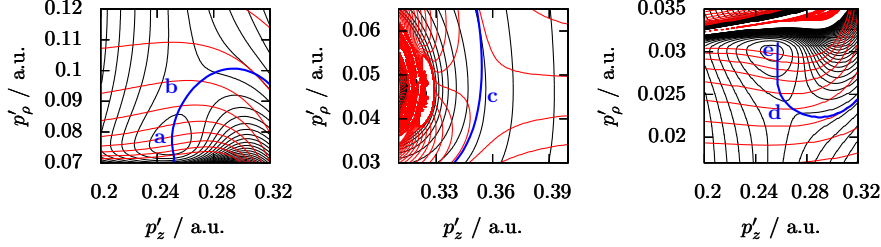


Figure 5.2: Details of Fig. 5.1 showing the three saddle points and the critical line (blue) through them. See the text for discussion of the letters.

coming from recollision at positive ρ_C , while recollisions at negative ρ_C is only possible after fly-by with large change of transverse momentum, giving a washed out feature. The higher tunneling probability for higher p'_ρ also contributes to making the features at negative p_ρ much more pronounced.

There is a long "tail" extending to large negative p_ρ . It is still significant when p_ρ is so large that the direct electrons are very improbable, thus forming a visible feature. This corresponds to the fork-like structures described in [82]. The tail is strongest for the VLES recollision since this occurs early on in the dynamics before the wave packet has spread too much in ρ , and is hardly visible beyond the first order LES.

The caustic was observed in [65] where however the transverse force alone was held responsible for the feature. Here we see that it is formed due to the critical line in the deflection function, the shape of which follows from the full interaction which is similar to the diagonalizable model of Section 4.2.

We follow the critical line in Fig. 5.1 in clockwise direction, starting from the chaotic region, and encounter the following features, corresponding to visible signs in Fig. 5.4. The letters correspond to Fig. 5.2.

- A maximum in p_z at (a), corresponding to the shape $p_z \sim p_\rho^2$ for the caustic around $p_\rho = -0.3$ au.
- A character change, given by the inflection point of the caustic at $p_\rho \approx -0.2$ au.
- A saddle point in p_z at (b): corresponds to the point where the caustic runs parallel to the p_ρ -axis at $p_\rho \approx -0.1$ au. This gives a peak in the marginal distribution in p_z since $\text{grad } p_z = 0$.
- A cusp. The whole process is distorted by the negative momentum kick received at pass by the core, as already discussed. Therefore this cusp does not coincide with a saddle point in p_ρ .
- A saddle point (c) in p_ρ at $p_\rho \approx -0.04$, cf. Eq. (4.14):
- Two additional cusps.
- A saddle point (d) in p_z at $p_\rho \approx 0.02$ au: corresponds to an additional peak in the marginal p_z spectrum, overshadowed by the first one.

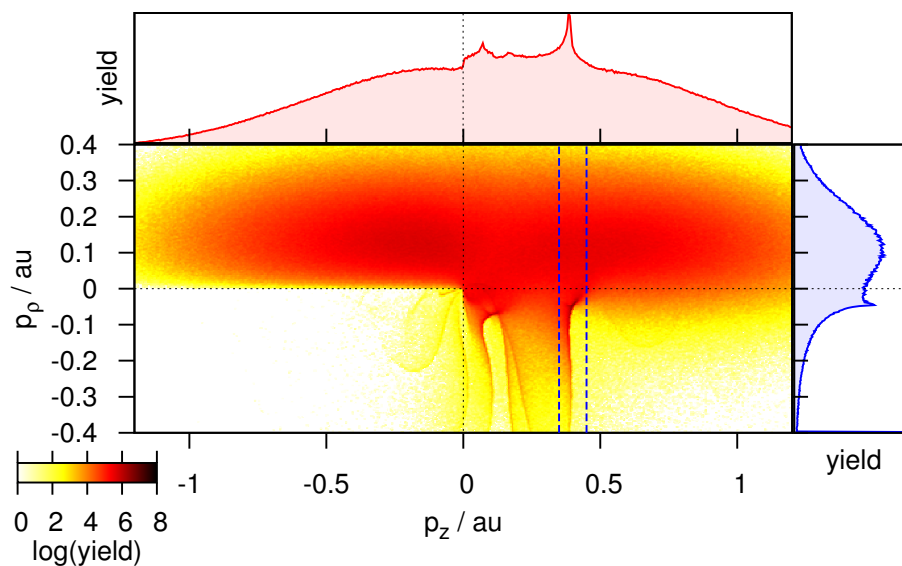


Figure 5.3: Distribution of final momentum. Laser parameters as in Fig. 5.1; ionization restricted to the central laser cycle. Marginal distributions are shown of p_z (red) and p_ρ (blue), where integration in the second case is restricted to the interval $0.035 \text{ au} < p_z < 0.045 \text{ au}$ indicated in the figure.

- A character change, giving another inflection point, at $p_\rho \approx 0.1 \text{ au}$.
- A maximum (e) in p_z close to $p_\rho = 0.2 \text{ au}$; the tunneling probability here is low so it is hardly visible.

5.2 Marginal distributions

5.2.1 Longitudinal momentum

In the deflection function for p_z there are two saddle points, corresponding to collisions at close to $\varphi = \pm 117^\circ$ where bunching is purely longitudinal ($\mathbf{e}_2 \parallel \mathbf{e}_{p'_z}$) in the idealized model (Fig. 4.4). The recollision point radius is approximately given by the critical distance at this angle, (Fig. 4.5). We can compute δp_z at this point from Eq. (4.2) to get an estimate for the final longitudinal momentum of the saddle point trajectory. Since the whole LES caustic structure is concentrated in a small p_z -range, this value can be used to estimate the whole structure. In Fig. 3.9 this was used to take the Coulomb potential at recollision into account, giving an overall redshift (smaller momentum) of the LES of a few percent. Fig. 5.5 shows a few trajectories close to the two saddle point, together with their drift momentum as function of time. At the recollision event, their initially different drift momenta are bunched together by the different influence of the Coulomb potential along the three trajectories.

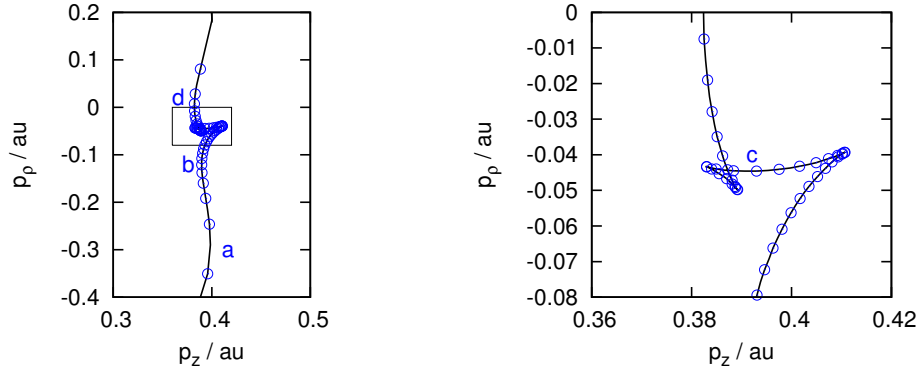


Figure 5.4: Left: Shape of the caustic in final momentum spectrum, with circles at equidistant points in initial phase space, showing the concentration around the cusps. Right: Detail. The letters correspond to those of Fig. 5.2.

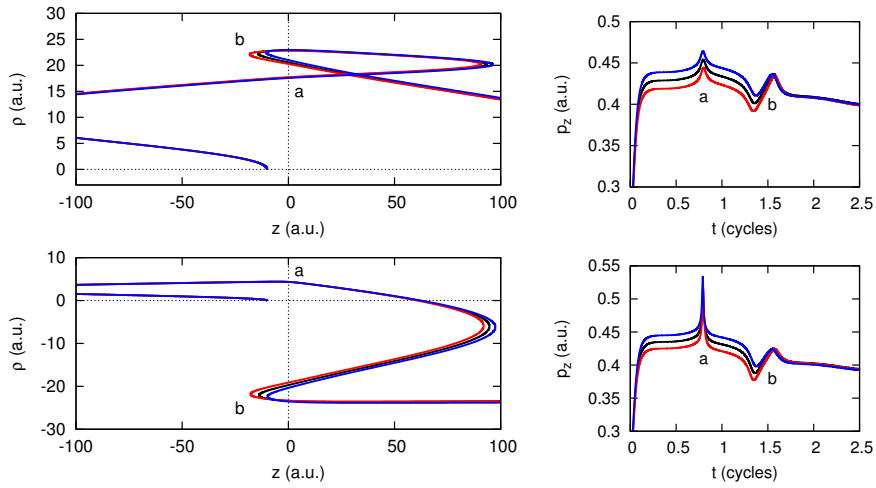


Figure 5.5: Upper: LES trajectories close to the first saddle point in p_z . (b) "Bunching" of drift momentum of the three trajectories. a indicate the fly-by, b the soft recollision. Lower: Similar for the second saddle point in p_z .

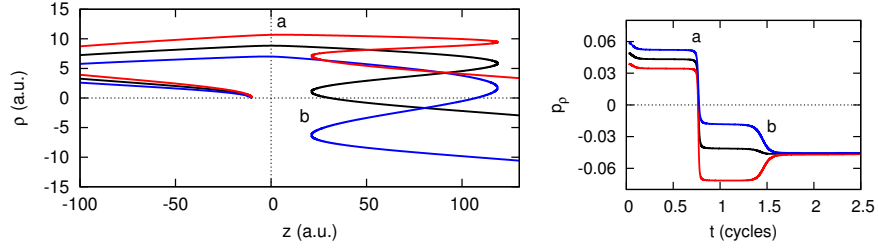


Figure 5.6: Trajectories close to the p_ρ saddle point. Bunching occurs in transverse momentum p_ρ .

5.2.2 Transverse momentum

In the deflection function for p_ρ there is one saddle point, corresponding to a collision close to $\varphi = 0^\circ$ where bunching is purely transverse ($\mathbf{e}_2 \parallel \mathbf{e}_{p_\rho}$) in the idealized model (cf. Fig. 4.4). The recollision distance is approximately given by the analytical expression Eq. (4.10). Fig. 5.6 shows a few trajectories close to the saddle point, and their transverse momentum. The bunching event is more intuitive in this case: the central trajectory stays close to $\rho = 0$ throughout the recollision so it is hardly influenced, while the other two each get a "kick" towards $\rho = 0$ during their motion.

The final p_ρ of the 1st order trajectory recolliding at $\rho = 0$ can be estimated by Eq. (4.14). Since the cusp singularity occurs for initial values close to this saddle point, Eq. (4.14) is proposed to estimate the transverse momentum of the cusp; typically the most prominent part of the 2D LES structure. For higher orders a numerical determination, using the system of difference equations Eq. (4.11) and looking for a recollision with $\rho = 0$ can be used.

Together with the basic estimate Eq. (3.5) of the LES longitudinal momentum (or Eq. (3.9) for a short pulse), this gives a prediction of the cusp location in the joint 2D spectrum. It is compared with simulations in Fig. 5.7.

The peak in transverse momentum has not been observed experimentally, presumably since the data was not evaluated in this way. It is hoped that the transverse momentum distribution of the LES structure will be measured experimentally, to allow comparison with Eq. (4.14).

Naturally the longitudinal and transverse directions are not unique in showing a peak in their marginal distribution. In the light of Appendix A.5.2 the marginal distribution along any direction has a divergence wherever the caustic is running perpendicular to it.

5.3 Conditional spectrum along $p_\rho = 0$

The original observation of the LES was done in the forward direction, i.e. collecting outgoing electrons within a small opening angle around the laser polarization direction (cf. Fig. 3.5). Considering the bivariate distribution as we have done here (cf. Appendix A.2), this means the LES occurred in the conditional distribution for $p_\rho = 0$. Due to the increasing availability of 2D distributions in the literature, other observed features have been identified as the LES [65], without making the relation completely clear. In this thesis we have used the

5.3 Conditional spectrum along $p_\rho = 0$

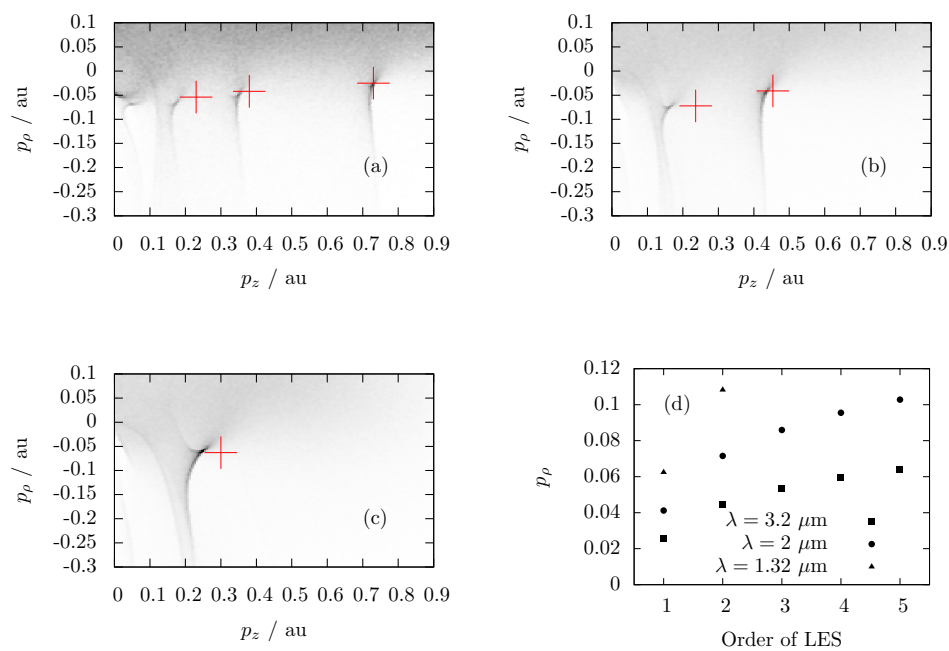


Figure 5.7: Details of photoelectron momentum spectrum for (a) $\lambda = 3.2 \mu\text{m}$, (b) $\lambda = 2 \mu\text{m}$ and (c) $\lambda = 1.32 \mu\text{m}$. Crosses show the predicted cusp locations by Eq. (3.9) and Eq. (4.14). (d) shows the expected maxima in p_ρ from the theoretical model. 4 cycle pulse, intensity 10^{14} W/cm^2 , tunneling in centre half-cycle only.

term "LES" for the complete 2D structure resulting from a low energetic recollision. The connection to the forward direction conditional LES remains to be made.

The main objective of this section will be to clarify whether the LES, as viewed in the conditional spectrum in the forward direction, is a predominantly longitudinal or transverse effect. By the section Section 4.2 we know that the directions of the eigenvectors of the Jacobian gives the direction of bunching, so we are able to give a quantitative answer to this question. As opposed to the model in Section 4.2 the full Jacobian is however not diagonalizable in an orthogonal basis.

The exact numerical results will depend on the laser parameters and the atomic species. For a given situation, only the full numerical treatment gives the full information. The qualitative features are however very general.

5.3.1 Contributions to the determinant

The conditional spectrum is in general given by the expression Eq. (A.5). The laser parameters are chosen as in Section 5.1.

The function $1/\det J$ is plotted in Fig. 5.8. The initial coordinates giving $p_\rho = 0$ are shown by the yellow dashed line (disregarding the small contribution in the forward direction coming from the chaotic region). The function plotted contains, together with the tunneling probability, the full information about the spectrum and the shading along the yellow line therefore directly gives the spectrum in the forward direction.

The matter is simplified since the final momentum p_z is growing monotonously along the line. Therefore we have an invertible mapping

$$(p'_\rho, p'_z) \mapsto (p_\rho = 0, p_z)$$

so that we can consider the final p_z or the final energy $E_{\text{final}} = p_z^2/2$ as a parametrization of the line of initial conditions.

We can gain information about the recollision by studying the elements of the Jacobian independently. Figure Fig. 5.9 shows a plot of the four elements, as function of final energy, in the vicinity of the recollision.

5.3.2 Non-orthogonal diagonalization

The Jacobian is not symmetric, due to the motion before recollision (see Section 4.4.1). One sees in Fig. 5.9 that the off-diagonal elements are not equal; they do however follow each other closely. We can still find the eigenvalues λ_1, λ_2 and eigenvectors $\mathbf{e}_1, \mathbf{e}_2$ of the Jacobian, but \mathbf{e}_1 and \mathbf{e}_2 are not orthogonal.

Finding the eigenvalues and plotting them as function of final energy leads to Fig. 5.11. In the figure also their product is shown, giving the dynamical factor in the spectrum, together with the total final spectrum, including tunneling probability.

Fig. 5.11 further illustrates how the weighting of initial conditions due to the tunneling process shifts the spectral peak a little to lower energy. The recollision distance r is also shown, giving the illustrative picture that the LES peak occurs for trajectories that turn around closest to the ion. In the light of Fig. 4.4, where the angle-dependency of the eigenvalue μ_2 is weak for recollisions in the first

5.3 Conditional spectrum along $p_\rho = 0$

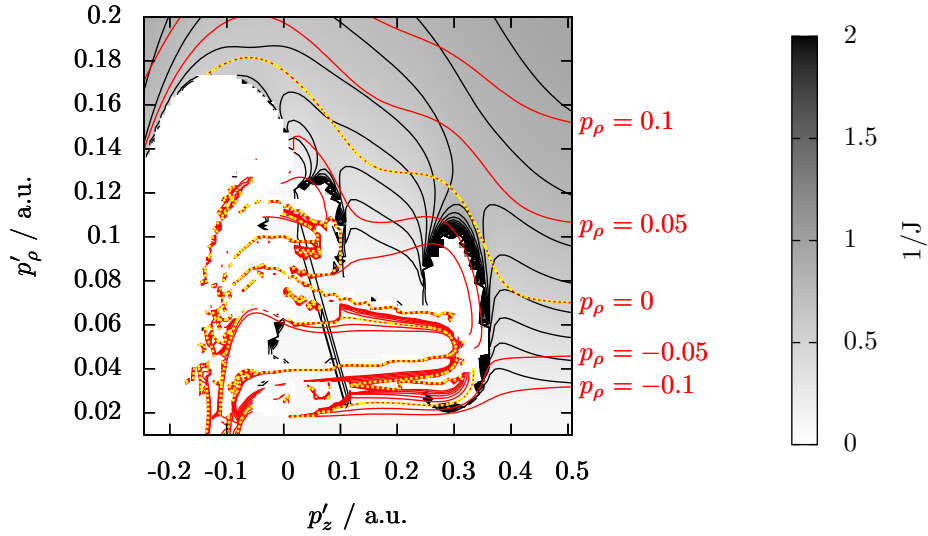


Figure 5.8: The function $1/\det J$ (black contour lines and shading) giving the final spectrum. Red contour lines indicate constant final p_ρ ; $p_\rho = 0$ is the yellow-red dashed line.

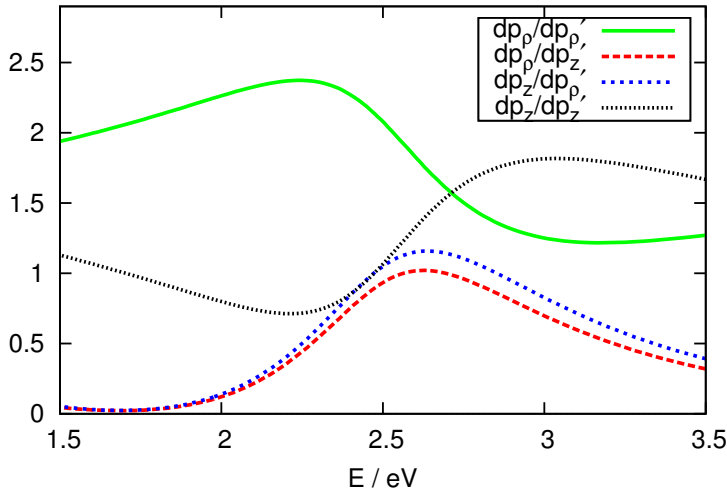


Figure 5.9: Elements of the Jacobian close to the recollision. 2.5 eV corresponds to initial momentum $p'_z = 0.33$ au, $p'_\rho = 0.11$ au in Fig. 5.8.

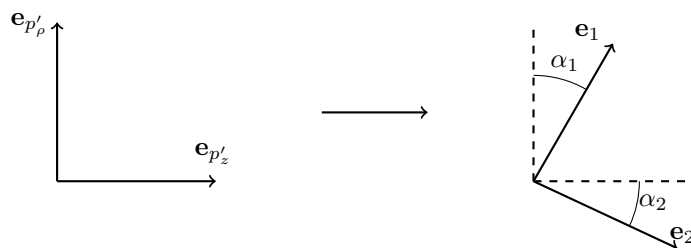


Figure 5.10: Definition of the angles α_1 and α_2 diagonalizing the Jacobian.

quadrant, this is not surprising; the eigenvalue λ_2 of the full J is dominantly governed by r , cf. Eq. (4.8). See also Fig. 5.12.

In the upper part of Fig. 5.11 the angle α_2 of the bunching eigenvalue is shown, defined by $\cos \alpha_2 = \mathbf{e}_2 \cdot \mathbf{e}_{p'_z}$ (cf. Fig. 5.10). It gives the direction along which the bunching eigenvalue is acting. Fig. 5.11 shows that, at the peak maximum, bunching takes place at an angle of approximately $\alpha_2 \approx 30^\circ$, which is more longitudinal than transverse. 45° is reached at around 2.7 eV, where the peak is lower, but still noticeable. The maximum angle reached, towards 3.4 eV, is close to 60° .

Since the eigenvectors are not orthogonal, the interpretation of the angle α_2 is less straightforward than the angle θ of Section 4.2. As shown in Fig. 5.11 the rotation angle α_1 defined as $\cos \alpha_1 = \mathbf{e}_1 \cdot \mathbf{e}_{p'_rho}$ is however very close to α_2 . The non-orthogonality is measured by $\Delta\alpha = \alpha_1 - \alpha_2$, which stays less than 5° throughout the LES peak. This angle can be taken as an uncertainty in the determination of the bunching angle.

A few recolliding trajectories are shown in Fig. 5.12. For forward motion recollision takes place along a line, which can be mapped directly onto the final energy. As this line passes nearby the line corresponding to the caustic, the LES is formed.

In Fig. 5.13 similar figures are shown for $\lambda = 3.2 \mu\text{m}$. Even though the peak energy is quite different, the qualitative shape of the plots are very similar to the $2 \mu\text{m}$ -case, pointing to the general applicability of the understanding presented here.

The exact values depend on the laser parameters and the order of the recollision. Still we stress again that the recollision event by itself is always similar to the model of Section 4.2 - only the motion before recollision, and the laser field strength at recollision, changes.

5.4 Experimental detection of the discussed features

There are several additional considerations when applying the conclusions of this chapter to the typical strong field experiment. In particular three effects are important:

- Tunneling takes place at several cycles within the pulse. For a short pulse this is suppressed due to the exponential dependence of tunneling probability on field strength (Eq. (2.10)), but for longer pulses one needs to

5.4 Experimental detection of the discussed features

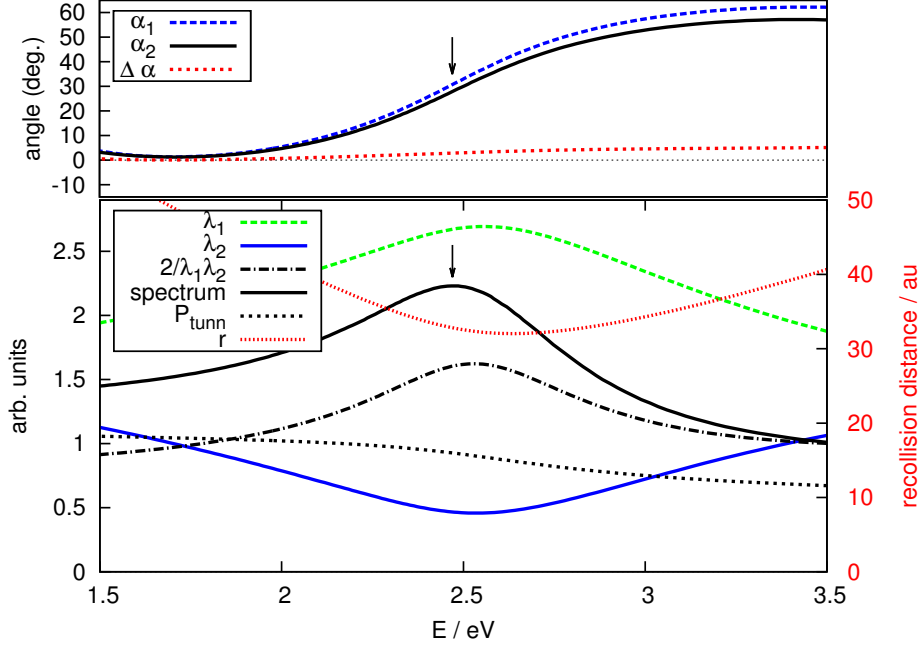


Figure 5.11: The eigenvalues λ_1, λ_2 of the Jacobian, the unweighted spectrum given by $\propto 1/\lambda_1\lambda_2$ (scaled by a factor 2 for visibility), the full spectrum including tunneling weighting of initial conditions, the tunneling probability P_{tunn} , and the recollision distance r . Upper panel shows the diagonalizing angles α_1 and α_2 , and their difference $\Delta\alpha$. The arrow points to the spectral peak.

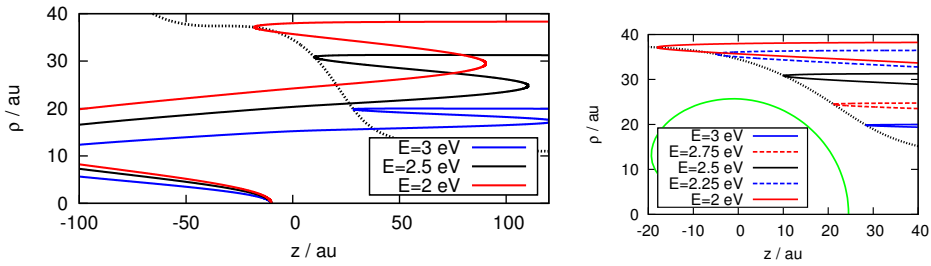


Figure 5.12: Left: Recolliding trajectories giving forward motion; the line of all recollision points is included. Right: Similar but with equal axis scaling and including the critical recollision distance, illustrating how the forward LES is formed by trajectories recolliding in the vicinity of the line of criticality.

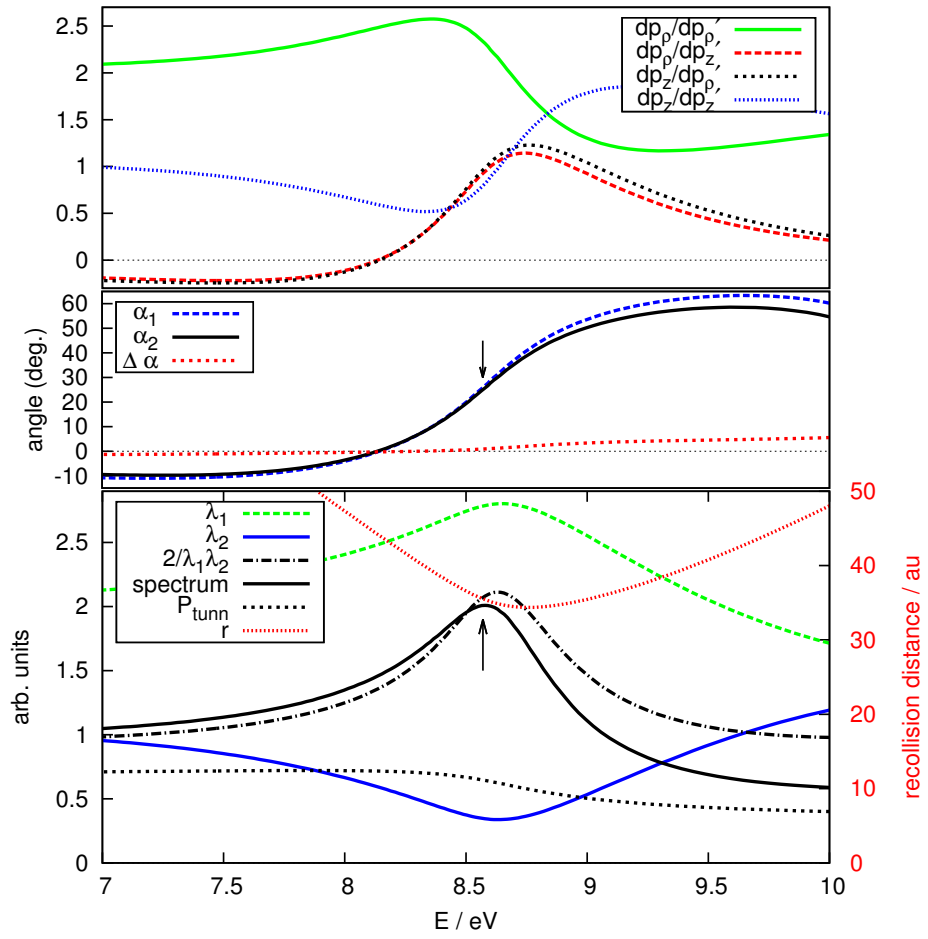


Figure 5.13: Similar to Figs. 5.9 and 5.11 for $\lambda = 3.2 \mu\text{m}$, 8 cycle pulse.

5.5 Summary

sum up the slightly different LES structures resulting from each tunneling event. This weakens the visibility of the divergence considerably.

- Focal averaging (see Section 2.2.2) similarly weakens the divergence, since the caustic location has to be averaged over the intensity distribution.
- Quantum mechanical effects tend to smear out classical divergencies due to the presence of a phase, meaning that measured distributions will typically be even smoother.

A divergence should not be expected in a real experiment; rather a broad maximum is found.

Fig. 5.14 shows the gradual inclusion of the classical effects into the simulation, for a 12 cycle pulse at $\lambda = 1.8 \mu\text{m}$ and $I = 1.8 \cdot 10^{13} \text{ W/cm}^2$ ionizing xenon. The parameters are chosen to coincide with those of [82]. Panel (a) has ionization artificially limited to the center half-cycle only, giving clear caustics for the LES. Also the extension of the VLES is visible, corresponding to the main prong of the fork structure [83]. In (b) ionization takes place in the full pulse, giving symmetric recollision features and overall broader features. Finally (c) shows the focal averaged result, giving broad features shifted to lower energy, according to Section 3.5.1. In (d) the corresponding distribution is shown as it could be measured, without desymmetrization (cf. Section 3.4.5. While less sharp the LES structures are still visible; especially the maximum at p_ρ according to the model Eq. (4.14), resulting from the cusp singularity, is prominent, as is the forward direction LES at the z -axis. Fig. 5.15 shows a detail including the marginal distributions, showing how the LES features could be observed.

By initially disregarding these complications, it is possible to understand the recollision by itself and the divergence which results in the ideal case, which is the main purpose of this chapter.

5.5 Summary

The critical line is the central feature of the low energy recollision, and it governs the whole spectrum in an intuitive way - for initial conditions close to the critical line the spectrum is enhanced, far away from it there is no effect. The different features that have been associated with the LES in the past can all be linked to the critical line in the following ways:

5.5.1 The caustic

The caustic itself, which is the image of the critical line in the joint momentum spectrum, was discussed in [65], without discussion of the deflection function or the diagonalization treated here, but rather as a phenomenological result from classical calculations. In measured 2dPMD from experiments, caustic-like structures appear [73]. They are rather weak due to the effects of Section 5.4 and quantum effects, that generally tend to smear out classical divergencies [65, 84].

The "transverse LES" discussed in [82], manifested there as a fork-like structure, is identified here as the "tail" of the caustics, which extends to large transverse momenta. The elastic recollision assumptions of [82] reproduce the structure for large energies; for small energies the inelastic recollision treated in

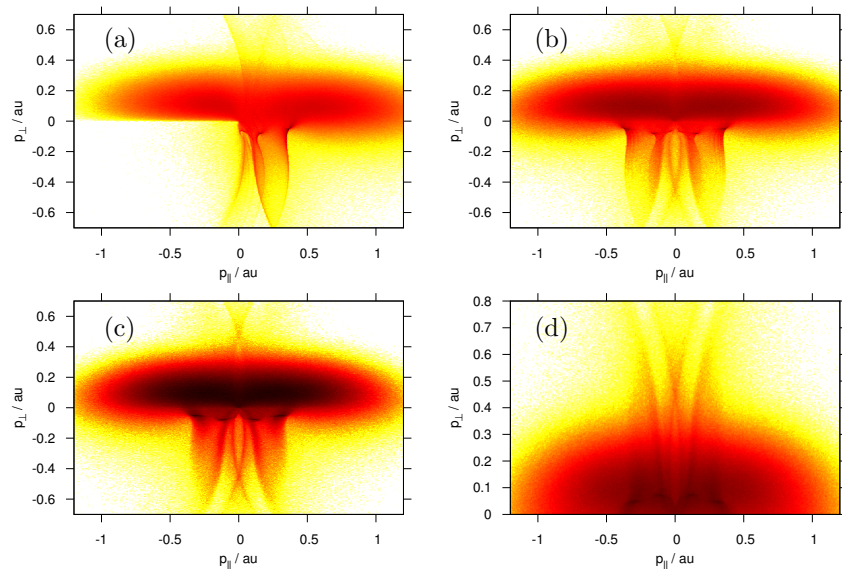


Figure 5.14: Different stages of realism in simulations. (a) ionization at central cycle only. (b) Ionization in full pulse. (c) Including focal averaging. (d) Measurable result without desymmetrization. 12 cycle pulse, $\lambda = 1.8 \mu\text{m}$ and $I = 1.8 \cdot 10^{13} \text{ W/cm}^2$ ionizing xenon. Logarithmic color scale.

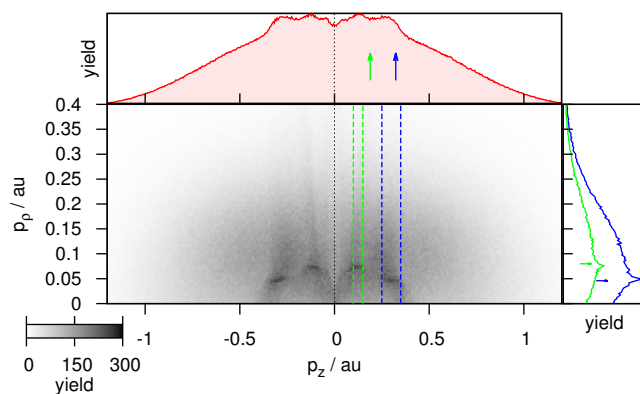


Figure 5.15: Detail of Fig. 5.14 (d) using a linear color scale making the LES more prominent, with marginal distributions showing the visibility of LES features. Arrows point to the predicted momenta by the LES trajectory model.

this chapter gives a more detailed view and reproduces the shape of the caustic. There is no essential disagreement in the results; in particular it is clear in Fig. 5.14 that the caustics extend to large energies where they take the shape described in [82].

We further point out that the shape of the VLES caustic strongly resembles the "v-shape" that has been observed in several experiments and simulations. It seems likely that this v-shape is indeed due to recollisions of the VLES type.

The question that has been raised in previous discussions, whether the effect is predominantly along the polarization direction ("bunching") or the transverse direction ("focusing") is somewhat inappropriate for the caustic, since the bunching effect we discuss here is acting in *all* directions, and depends on the angle φ from the origin to the turning point. Pure bunching in one or the other direction does occur for specific values of φ but has no fundamental importance - all bunching directions are on an equal footing. The underlying reason is the potential Φ of Eq. (4.3), which is almost radially symmetric for the relevant angles, thus allowing bunching in a large range of angles. The *strength* of bunching is not equal for all angles but also not sharply peaked anywhere, though a quantitative treatment of this question requires studying the higher derivatives of Φ which is beyond the scope of this work.

5.5.2 Longitudinal bunching

The general properties of caustics, outlined in Appendix A.5 show that the marginal distribution will have a divergent peak wherever the caustic runs perpendicular to the direction. Equivalently, there will be a saddle point in the deflection function of the momentum in that particular direction. The marginal spectrum along the laser polarization axis will have two such peaks per LES recollision due to the general shape of the caustic. This is the longitudinal bunching discussed in [67]. Simulations show that this is a very strong effect and gives a clear series of peaks. The VLES peak tends to be hidden by FTI unless the pulse is very short. The visibility is further obscured by averaging over the focal intensities and different ionization cycles within the pulse (for longer pulses), giving the appearance of a "double hump" that has been observed many times [59, 71].

5.5.3 Forward-direction LES

One major advantage of the method discussed here, where fully differential information about the momentum spectrum is available, is the ability to analyze the conditional spectrum along arbitrary direction. This is the setting where the LES was discovered and where most of the discussions have been centered. From the deflection functions one immediately sees that the spectrum in forward direction will have a peak when the initial conditions giving forward motion are close to the critical line.

Important in shaping the conditional forward spectrum is the restriction on initial conditions leading to forward motion. This gives a line in initial phase space, which comes close to the critical line only once for each LES event, thus giving a peak. Using an approximate diagonalization the angle of bunching is typically around 30° at the peak maximum, i.e. more longitudinal than

transverse. It is however quite rapidly changing also within the peak, due to the recollision angle φ changing rapidly.

Since the matrix $G(\varphi)$ is almost constant for the relevant angles, the r -dependence is dominating the bunching eigenvalue. Thus the maximum of the LES peak roughly corresponds to the trajectory with turning point closest to the origin.

5.5.4 Final remarks

The LES should therefore best not be seen as a purely directional effect but rather a signature of a divergence in the spectrum: a critical line in the initial conditions giving a caustic in the final joint momentum distribution. This caustic is not directly visible in one-dimensional spectra: it manifests itself as a (in principal divergent) peak in the marginal distributions along any direction, and traces of it can be visible in the conditional spectra. Specifically in the forward direction, the effect is seen by an accumulation (but not divergence) which is due to bunching in rapidly changing angle, typically centered around 30° .

The longitudinal bunching of [67] thus describes the effect in the marginal spectrum in the polarization direction, and the saddle point in the deflection function discussed there is a special case of the critical line. The "Coulomb focusing" of [63] is more dubious to interpret in our context - while there is pure bunching in the transverse direction, this does not give a peak in the forward direction but with quite some offset, due to the negative transverse momentum (resulting from passing by the ion) of electrons recolliding at $\rho = 0$. Due to the pure geometric effect, the *differential* distribution along z will diverge [85], but this is true for *all* longitudinal momenta since, from the passing of the ion, there are electrons present with $p_\rho = 0$.

Chapter 6

The Zero-energy-structure

In this chapter a recently discovered [6] feature at the extreme low end of the photoelectron energy spectrum is discussed. The basic experimental setup remains the same as in previous chapters. The observation was made through combination of the high precision COLTRIMS detection method [23] with a high intensity mid-IR laser ($\lambda = 3.2 \mu\text{m}$), thereby probing a new parameter regime.

The origin of the observed peak in [6] was unknown. Compared to the LES, which was also detected in the experiment, it occurred at a much smaller energy scale. Its peak momentum value was in fact indiscernible from zero, within the experimental resolution. Its high concentration around zero made it a pronounced visible peak in the momentum spectrum, even though its total weight was small compared to larger scale features. It was speculated to be formed by either some recollision mechanism distinct from the LES one, or by ionization of bound states initially formed by the FTI mechanism Section 2.5. It soon became referred to as the zero-energy-structure, ZES.

The structure was confirmed experimentally in [86], together with a qualitative theoretical description in [73]. A fully quantitative theory in agreement with experiments was given in [8], where the results were reported that are described in more detail in this thesis.

In this chapter and the next a complete classical theory of the ZES is presented, along with numerical simulations. The explanation relies on the FTI mechanism of Section 2.5 for population of highly excited atomic states, followed by ionization of these states by an external electric field. This field is present in the detectors used in [6] and similar experiments. The ZES can thus be regarded as an experimental artefact which does not indicate unknown features of the laser-atom interaction, as was speculated initially. On a more positive side, it does show the result of a physical process which is susceptible to a complete analysis, and could potentially resolve very fine details about the physics of the problem, especially with an increase in precision from that of today.

In Section 6.1, the experiment and the workings of the detection apparatus is described from a theoretical point of view. In Section 6.2 our hypothesis is put forth and the different time scales of the motion is discussed. This indicates that the physics of ZES formation is that of the Stark problem, which is described in Section 6.4. Only the aspects important for the ZES are discussed.

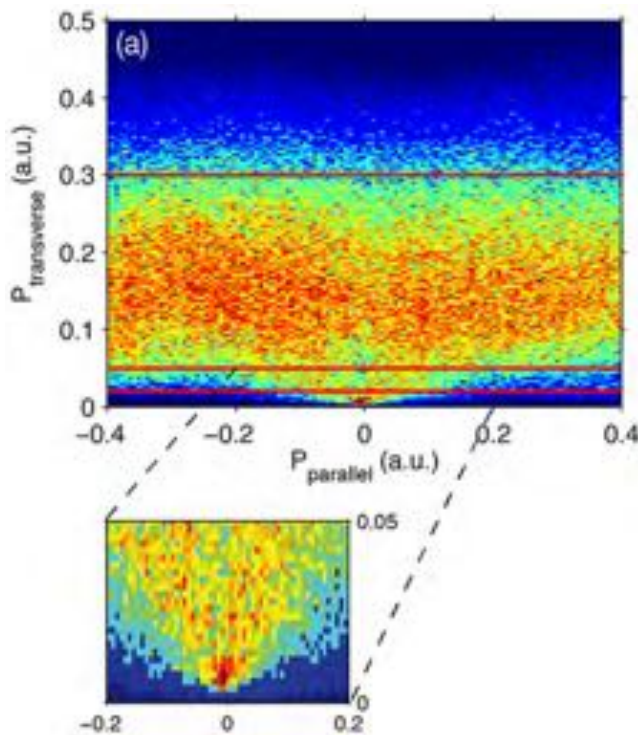


Figure 6.1: Experimental detection of ZES, from [6].

A detailed analysis of the motion is postponed until Chapter 7, in order to keep the reasoning in direct connection with the experiment clear. Simulation results are shown in Section 6.5, demonstrating that the simple scaling properties resulting from the Stark model are indeed reproduced by a full numerical treatment. In Section 6.6 a comparison with experimental data is made, confirming the validity of the Stark scaling.

6.1 Experimental observation

6.1.1 Properties of the ZES

The first observation of the ZES [6] was done in an experiment with laser wavelength of $3.2 \mu\text{m}$ and intensity of $I = 10^{14} \text{ W/cm}^2$, with a pulse length of ca 50 fs corresponding to around 6 cycles, ionizing argon atoms. The full 3D photoelectron momentum distribution was measured; the central part is shown in Fig. 6.1. The experiment is clearly in the classical regime since no interference patterns are visible; the LES was also detected. The ZES is the narrow peak very close to zero, at momenta where previous studies have not shown any particular features.

[6] reported the following characteristic properties of the peak:

1. A significant single peak on top of a comparatively flat background.
2. Peak energy at a few meV, within experimental resolution from 0.

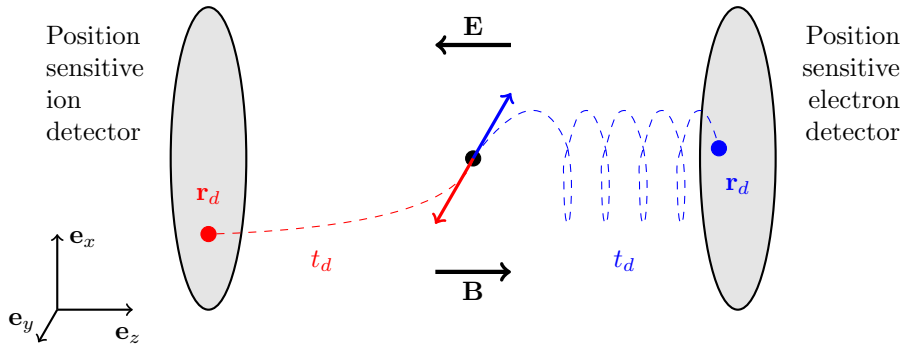


Figure 6.2: Sketch of the reaction microscope setup. The z -axis is antiparallel to the electric field. The magnetic field makes the real experimental situation more complicated but the measurement in z -direction is untouched.

3. A small shift towards negative momentum, however also within experimental resolution from 0.

The peak also appeared in the experiments of [73,86], where a shift was not clearly seen.

6.1.2 Principle of the reaction microscope

All ZES experiments were done using a so-called reaction microscope (REMI) [23] utilizing the COLTRIMS (cold target recoil ion momentum spectroscopy) technique. Its purpose is to measure the full 3D momentum spectrum of electrons and ions, resulting from some interaction process (not limited to photoionization but including all kinds of scattering processes). For single-ionization processes, the ability to simultaneously measure the electron and ion products enhances the precision [87].

The central part of the reaction microscope is a vacuum chamber, where the target atoms are inserted as a dilute gas. On each side, a detector plate is placed at a macroscopic distance (typically decimeters) from the interaction region. Charged particles are guided towards the detector plates by a weak electric field, sending positive particles to one plate and negative particles to the other. In order to handle the large possible velocities of light particles (in our case, electrons) and keep them confined within the chamber until they reach the detector plate, a magnetic field is applied parallel to the electric field, giving the particles a spiralling motion. For technical details on the setup, the reader is referred to [23].

Important from the theoretical side are the following points only. The scattering process under study takes place under influence of external electric and magnetic fields, that guide the electrons and ions to the detector plates. The magnetic field is irrelevant for our problem, since it only has significant influence at very high electron velocities that are only reached on macroscopic distance from the ion. It is neglected in the following. The electric field typically ranges between 1–10 V/cm, which is much weaker than other fields in the experiment, leading one to assume that it does not change the scattering process appreciably.

Having escaped the scattering region, the electrons are accelerated by the external field, deflected by the magnetic field, and then hits the detector at a specific position \mathbf{r}_d and time t_d . The time of interaction t_0 is precisely known due to the shortness of the laser pulse, so the time of flight to the detector $t_d - t_0$ is known to high accuracy. So is the position at the detector plates (x_d, y_d) . Thus one obtains the initial momentum in two directions (x, y) - the plane of the detector plate - from its position and flight time, and the momentum in the third direction z - that of the detector field - from time of flight only:

$$p_z^{(m)} = Ft_{\text{ref}} - Ft_d . \quad (6.1)$$

t_{ref} is a reference time corresponding to motion from the laser focus to the detector under influence of the extraction field only; it is typically not calculated but instead the line $p_z^{(m)} = 0$ is manually calibrated from measured data.

It is immediately seen from Eq. (6.1) that the REMI cannot distinguish between an electron with a certain initial momentum in the direction opposite to the detector plate, and an electron which, for whatever reason, spends a certain amount of time in the interaction region before escaping, with low velocity, to the detector.

6.2 Hypothesis

Our model for ZES formation relies on two points:

1. FTI populating excited atomic states across threshold (Section 2.5).
2. The electric field of the detector ionizing some of these states.

Field ionization of Rydberg states by an external electric field is a common experimental technique [88], but it is not clear from the outset how electrons from that process will be detected in the REMI setup. For bound states, it is meaningless to talk about a definite final electron velocity after interaction, since the electron moves in Kepler ellipses around the ion. What we will show is that in an intermediate energy range the electron does escape to the detector, but only after spending a long time in the vicinity of the ion. This means that compared to what one expects without taking the electric field of the detector into account:

1. The liberated electrons show up at the detector, forming a peak (as will be shown).
2. They are detected with very low energy.
3. They are most likely to arrive a little later than t_{ref} , due to the delay time in escaping the influence of the ion.

The three essential features of the ZES are thus reproduced.

6.3 Separation of time scales

The creation of bound states by FTI and the ionization by the extraction field occur on vastly different time and length scales, so they can be viewed as sequential processes.

The first step, the FTI, is already contained in a complete description of the strong-field ionization process, and serves essentially as giving initial conditions for the second step. The second step by itself is field ionization of Rydberg states, as widely used in studying high-lying atomic states and their response to external fields. The generality of our model does not even require step 1 to be a strong-field laser experiment; any physical process (broadband one-photon excitation, inelastic collisions etc) producing a rather flat spectrum across threshold would lead to the same physical situation. We will therefore make less reference to the strong-field excitation and discuss the field ionization in as general terms as possible.

The total Hamiltonian is

$$H = \frac{\mathbf{p}^2}{2} - \frac{1}{|\mathbf{x}|} + \mathbf{x} \cdot \mathbf{E}_L(t) + \mathbf{x} \cdot \mathbf{E}_C$$

where $\mathbf{E}_L(t)$ is the time-dependent electric field of the laser, and \mathbf{E}_C the constant field of the detector. The combined potential of the ion and the laser field during tunneling is shown in Fig. 6.3, compared with the potential of the ion and the detector field. The axes scales differ by many orders of magnitude. While the laser-atom interaction in the strong-field regime takes place on a length scale of nanometers and a typical energy scale of eV, the detector field perturbs the Coulomb potential only on a μm scale, and in meV of energy. This also leads to a similar separation of time scales. The laser oscillates on a fs time scale, while the escape of electrons with $E = 0$ typically takes nanoseconds for experimental field strengths. Closer to the barrier, the delay is even longer.

For motion in the potential of Fig. 6.3b, the motion of Fig. 6.3a gives only initial values. Once the laser pulse is over at time t_1 , we still have $r(t_1) \ll 1 \mu\text{m}$ for low energy electrons. The spectral features produced by step 1 - LES, VLES and others - are typically not resolved at the order of meV, giving an almost flat spectrum. The same is true for quantum features not included in the classical simulations, where ATI peaks (single photon peaks) still have a width $\gg 1 \text{ meV}$.

We are thus led to study step 2 separately, for a given initial distribution that can be obtained in simulation from step 1, or approximated by some reasonable assumptions. One complication is that we are not only interested in the *momentum* distribution of the liberated electrons, but also their *time of flight* to the detector, since this is the measured quantity that enters into Eq. (6.1) in order to calculate the initial velocity along the extraction field axis.

6.4 Stark problem

The situation in the extraction field (step 2) is the well-known Stark problem [89] of an electron under the combined influence of an ionic potential and a constant electric field.

Since we are interested in motion on a μm length scale of a single liberated electron, multi-electron and polarization effects are neglected (like in the laser-driven motion in previous chapters) giving the single-electron hydrogenic Hamiltonian:

$$H = \frac{\mathbf{p}^2}{2} - \frac{1}{|\mathbf{x}|} - Fz \quad (6.2)$$

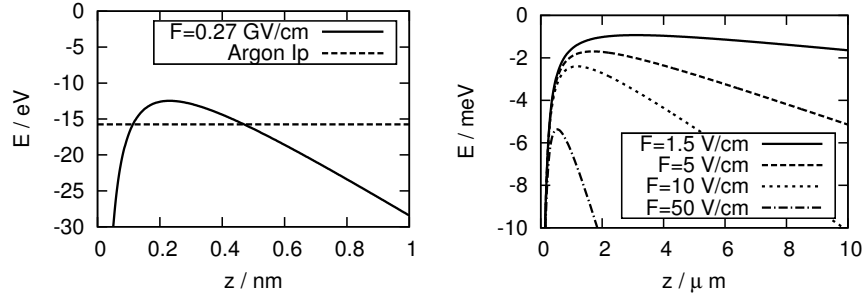


Figure 6.3: Comparison of the maximal electric field of the laser (left), and the extraction field (right) for a few different field strengths. Both fields point along the z -axis. Note the different axes scales!

where as always in the following the field is oriented antiparallel to the z -axis; $\mathbf{E}_C = -F\mathbf{e}_z$. The difference to Eq. (2.1) lies simply in the constant final term, as opposed to a time-dependent laser term. This gives a drastic simplification and allows fully analytical solutions.

6.4.1 Scaling properties

Eq. (6.2) allows the general scaling [90]

$$\begin{aligned} \mathbf{p} &= \mathbf{p}' F^{1/4} \\ \mathbf{x} &= \mathbf{x}' / F^{1/2} \end{aligned} \quad (6.3)$$

which is seen by introducing the scaled quantities in Eq. (6.2), arriving at

$$H = \frac{\mathbf{p}'^2 \sqrt{F}}{2} - \frac{\sqrt{F}}{|\mathbf{x}'|} - \frac{\mathbf{x}'}{\sqrt{F}} \cdot \mathbf{F} = \sqrt{F} H'$$

Since an overall factor in the Hamiltonian does not enter into the equations of motion, this is equivalent to the original Hamiltonian with energy scaled as

$$E = \sqrt{F} E' . \quad (6.4)$$

The scaling of time is also obtained as

$$t = x/p = x'/p' F^{-3/4} = t' F^{-3/4} \quad (6.5)$$

It therefore suffices to study the scale-free ($F = 1$) Hamiltonian

$$H = \frac{\mathbf{p}'^2}{2} - \frac{1}{|\mathbf{x}'|} - \mathbf{x}' \cdot \mathbf{e}_F \quad (6.6)$$

and then scale all results according to Eqs. 6.3-6.5 for arbitrary field strengths. Here \mathbf{e}_F is a unit vector in the direction of the constant field \mathbf{F} .

The scaling alone tells a great deal about the motion. The overall ionization threshold, being a limit in energy, must scale as $\sim \sqrt{F}$. Any structure in the final momentum, as measured in the experiment, must scale as $\sim F^{1/4}$.

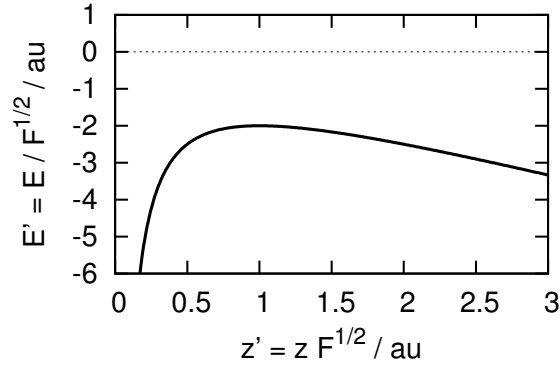


Figure 6.4: The Stark potential along the field axis in scaled units. The barrier is located at $z' = 1$ and its maximum is at $E' = -2$

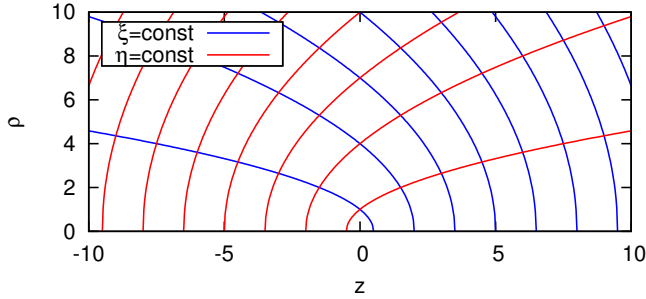


Figure 6.5: Level curves of the parabolic coordinates defined by Eq. (6.8)

We always take the constant field along the z -axis. The potential of Eq. (6.6) is then, dropping the primes,

$$V = -\frac{1}{|\mathbf{x}'|} - z' .$$

The potential along the z -axis is shown in Fig. 6.4. It has a minimum at $z' = 1$, taking the value $V(1) = -2$. Combined with the scaling Eq. (6.4) this is the well-known limit for field ionization [88]

$$E_{\min} = -2\sqrt{F} \quad (6.7)$$

which is widely used in the context of static field ionization of Rydberg states. It is the lower limit of accessible energies; whether a state is actually ionized depends also on the motion in other directions. This is analyzed by properly separating the problem, as is done next.

6.4.2 Separation of variables

From now on we drop the primes and use exclusively scaled units unless otherwise noted. The Hamiltonian Eq. (6.6) is separable in parabolic coordinates.

Define in 3D [91]

$$\begin{aligned}
 \rho &= \sqrt{\xi\eta} & \xi &= r + z \\
 z &= (\xi - \eta)/2 & \eta &= r - z \\
 x &= \rho \cos \varphi, \quad y = \rho \sin \varphi & \varphi &= \arctan(y/x) \\
 r &= \sqrt{\rho^2 + z^2} = (\xi + \eta)/2 & \xi, \eta &\geq 0
 \end{aligned} \tag{6.8}$$

See Fig. 6.5. Restricting to the planar problem gives $\varphi = 0$ or $\varphi = 180^\circ$. Since the parabolic coordinates are always positive, φ makes a discontinuous jump whenever the z -axis is crossed.

The Hamiltonian doesn't depend on φ , so it is a cyclic coordinate; in our problem we can to good approximation set $p_\varphi = 0$, leading to a 2D situation.

The Hamiltonian Eq. (6.6) in parabolic coordinates then becomes

$$H = 2 \frac{\xi p_\xi^2 + \eta p_\eta^2}{\xi + \eta} - \frac{2}{\xi + \eta} - \frac{\xi - \eta}{2}$$

Since energy is conserved, we can write the Hamilton-Jacobi equation [92] as

$$2\xi \left(\frac{\partial S}{\partial \xi} \right)^2 + 2\eta \left(\frac{\partial S}{\partial \eta} \right)^2 - 2 - \frac{\xi^2 - \eta^2}{2} - E(\xi + \eta) = 0$$

which separates into

$$\begin{aligned}
 2\xi \left(\frac{\partial S}{\partial \xi} \right)^2 - 1 - \xi^2/2 - E\xi &= \beta \\
 2\eta \left(\frac{\partial S}{\partial \eta} \right)^2 - 1 + \eta^2/2 - E\xi &= -\beta
 \end{aligned}$$

where β is a constant of motion that can be identified as

$$\beta = -\left(-\frac{z}{r} + p_x(zp_x - xp_z)\right) - \frac{x}{2}. \tag{6.9}$$

This gives expressions for p_ξ and p_η :

$$p_\xi = \frac{\partial S}{\partial \xi} = \sqrt{\frac{E}{2} + \frac{\beta}{2\xi} + \frac{1 + \xi^2/2}{2\xi}} \tag{6.10}$$

$$p_\eta = \frac{\partial S}{\partial \eta} = \sqrt{\frac{E}{2} - \frac{\beta}{2\eta} + \frac{1 - \eta^2/2}{2\eta}} \tag{6.11}$$

and the action is given by

$$S = \int p_\xi d\xi + \int p_\eta d\eta. \tag{6.12}$$

The separation constant β can be given an intuitive meaning when considering the limiting case of trajectories passing through the origin. (All trajectories of interest in our case are of this kind, since they start very close to the origin in the scaled coordinates.) For such trajectories, close to the origin $\mathbf{r} \parallel \mathbf{p}$, so in

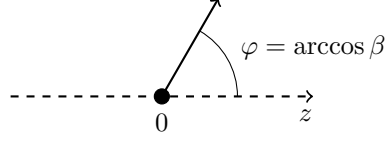


Figure 6.6: Definition of β for trajectories starting at the origin.

polar coordinates $z = r \cos \varphi$, $\rho = r \sin \varphi$, $p_z = p \cos \varphi$, $p_\rho = p \sin \varphi$. Eq. (6.9) goes into

$$\beta = \cos \varphi - p^2 r \sin \varphi (\sin \varphi \cos \varphi - \cos \varphi \sin \varphi) - \frac{r \sin \varphi}{2} \longrightarrow \cos \varphi$$

as $r \rightarrow 0$. β is simply the cosine of the angle of the escaping trajectory towards the z -axis, cf. Fig. 6.6. $\beta = 1$ means the trajectory goes along the z -axis to infinity, while $\beta = -1$ means it starts in negative z -direction. Since a trajectory cannot go through the origin, such a motion will never result in ionization, so $\beta = -1$ gives a trapped electron for all energies. This is a periodic orbit of the Stark problem [93, 94]; for $E \geq 0$, it is the only one. For lower energies, there is a range of periodic orbits, as is seen by studying the motion given by Eq. (6.10) and ((6.11) in detail as follows.

6.4.3 Initial conditions

We always have the initial condition

$$\rho(0) = z(0) = 0 .$$

The initial momentum is given in terms of E and β by

$$\begin{aligned} p_\rho &= \sqrt{2E} \sin \arccos \beta = \sqrt{2E} \sqrt{1 - \beta^2} \\ p_z &= \sqrt{2E} \beta . \end{aligned}$$

E and β must in principle be distributed according to the full laser-induced dynamics. They can for a first treatment however be approximated as constant in the allowed range:

$$\begin{aligned} w(E) &= 1/2 \quad \text{for } -2 \leq E \leq 0 \\ w(\beta) &= 1/2 \quad \text{for } -1 \leq \beta \leq 1 . \end{aligned}$$

The real distribution in β does change depending on the setup, especially when changing the angle between the laser polarization and the extraction field direction. The change induced by this is too small to be seen in the experiments discussed here; it could possibly be observed in future experiments with higher resolution and/or stronger extraction field (which makes features easier to see due to the scaling Eq. (6.3)). Some other excitation mechanism, e.g. broadband single-photon excitation, would also lead to a different β -distribution. The *dynamical* features presented here do in most cases still prevail, since only the relative weight of the contribution to the spectrum is changed (cf. Appendix A.3).

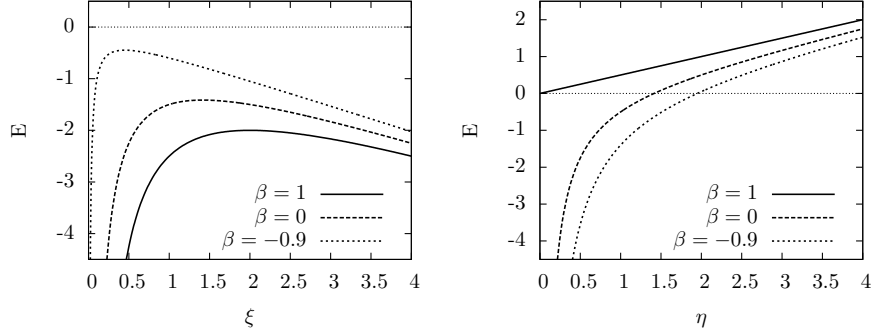


Figure 6.7: Potentials in ξ , Eq. (6.13), and η , Eq. (6.14), for a few β -values.

6.4.4 Field ionization threshold

We can rewrite the expressions Eq. (6.10)-(6.11) as

$$p_\xi = \sqrt{\frac{1}{2}(E - V_\xi(\xi))} \quad , \quad V_\xi = -\frac{1+\beta}{\xi} - \frac{\xi}{2} \quad (6.13)$$

$$p_\eta = \sqrt{\frac{1}{2}(E - V_\eta(\eta))} \quad , \quad V_\eta = -\frac{1-\beta}{\eta} + \frac{\eta}{2} \quad (6.14)$$

The two potentials depend parametrically on β ; they are plotted in Fig. 6.7. Motion in η is clearly bound for all energies and separation constants, with a turning point at

$$p_\eta = 0 \implies \eta = E + \sqrt{E^2 + 2(1-\beta)} .$$

In ξ there are turning points at

$$p_\xi = 0 \implies \xi = -E \pm \sqrt{E^2 - 2(1+\beta)}$$

which are only real if the condition

$$E \leq -\sqrt{2(1+\beta)} \implies \beta \leq E^2/2 - 1$$

is fulfilled. Thus we get the more precise ionization condition corresponding to Eq. (6.7), but including the fully separated problem

$$E_{\text{lim}} = -\sqrt{2(1+\beta)} . \quad (6.15)$$

For linear motion in positive direction (going over the saddle point in the potential towards the detector), $\beta = 1$ so the value $E_{\text{lim}} = -2$ is recovered, corresponding to Eq. (6.7) and Fig. 6.4.

A schematic picture of the ionized states in the E, β -plane of initial coordinates is shown in Fig. 6.8. For all energies $E < 0$, there is an interval of β -values giving bound motion, i.e. periodic orbits. The total weight of the bound states (for a flat initial distribution) is found as

$$\frac{\int_{-2}^0 dE (E^2/2 - 1)}{\int_{-2}^0 dE} = \frac{[E^3/6 - E]_{-2}^0}{2} = \frac{1}{3} . \quad (6.16)$$

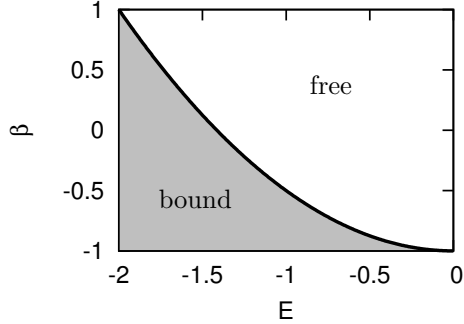


Figure 6.8: The square of initial conditions, with bound and free states indicated.

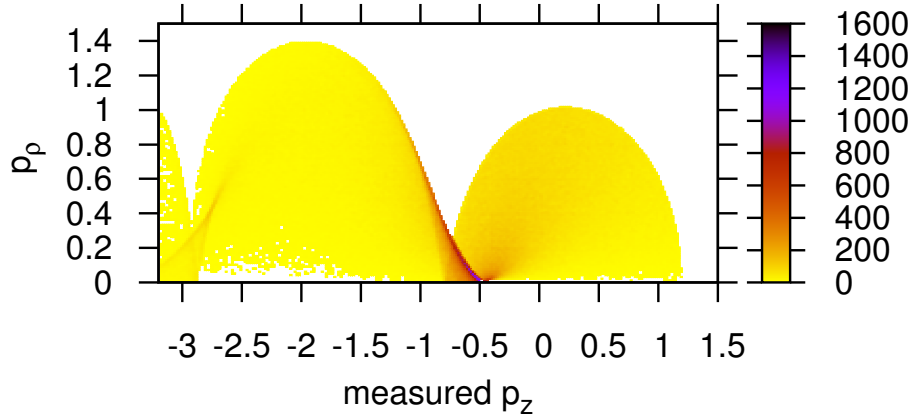


Figure 6.9: Final measured momentum distribution in scaled units.

6.4.5 Final momentum distribution

The measured momentum spectrum of the Stark motion, with initial conditions evenly distributed within the allowed range, is shown in Fig. 6.9.

Note that the measured momentum along the field $p_z^{(m)}$ is given by the physical time of flight, according to Eq. (6.1).

A peak is clearly formed close to the z -axis, at $p_z^{(m)} \approx -0.6$. In addition to this a series of peaks with decreasing magnitude appear at larger negative p_z . The main peak, which is very prominent compared to its the background, is identified with the ZES.

The formation of the spectrum is discussed further in Chapter 7.

It is important to note that, due to the scaling properties of Eq. (6.3), Fig. 6.9 is completely general and depicts the spectrum for *any* extraction field strength. By scaling the axes by $F^{1/4}$ (atomic units) the momentum spectrum for a specific field strength is obtained.

This points to the universality of the ZES; its qualitative properties are completely independent of the field strength. The quantitative change of these

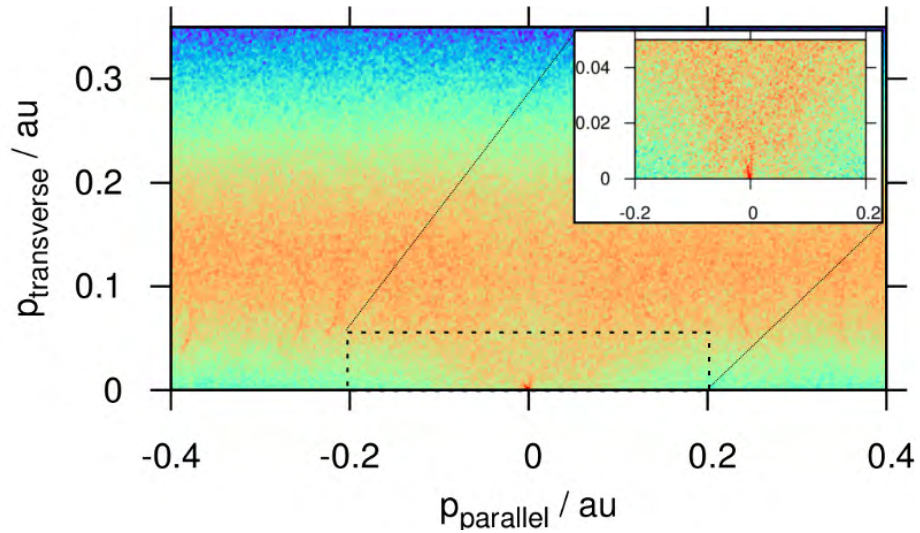


Figure 6.10: CTMC simulation including the detector field. $\lambda = 3.2 \mu\text{m}$, intensity 10^{14} W/cm^2 , extraction field strength $F = 1.5 \text{ V/cm}$, argon target.

properties are directly predicted by the Stark scaling.

6.5 Simulation results

Simulations were carried out for the full problem of laser driven dynamics under the additional extraction field, by modifying the CTMC method; see Appendix C.

The results of a simulation including the detector field is shown in Fig. 6.10. The parameters were chosen according to those of [6]: laser wavelength $\lambda = 3.2 \mu\text{m}$, intensity 10^{14} W/cm^2 , extraction field strength $F = 1.5 \text{ V/cm}$. The ZES turns up close to zero momentum, very similar to the experimental result of [6]. Looking in detail there is a slight shift towards negative momentum in the direction of the detector field.

A second simulation result is shown in Fig. 6.15. Here the detector field is turned 90° with respect to the laser polarization, giving a small shift towards negative y -momentum.

The simulations clearly show that the ZES can result from including the detector field in the simulation. While this does not prove that this is indeed what was seen in [6] it gives clear evidence for this. Most importantly the simulations presented here are a very accurate description of the experiment (within the limits of classical physics, see Section 6.7 for a discussion on this point). If the ZES is due to something else, why is the peak described here not visible?

6.5.1 Scaling of momentum

We investigate the scaling properties of the ZES peak numerically and compare to the expected scaling in Section 6.4. In the simulation this is simply done by

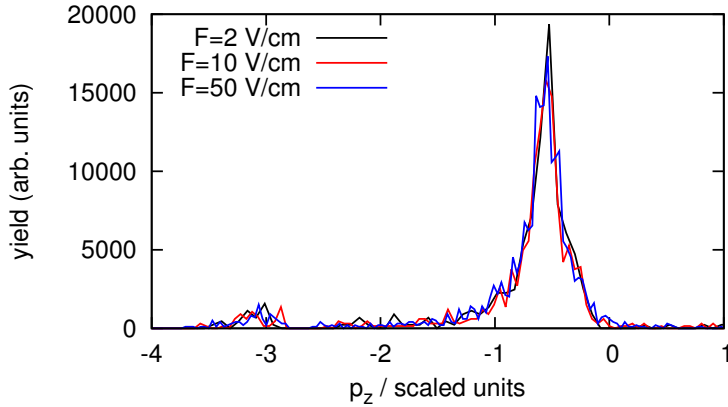


Figure 6.11: Momentum spectra along the extraction field axis z with laser polarization in the x -direction. Integration limited to $|p_z| \leq 0.1$ and $|p_y| \leq 0.1$, in scaled units.

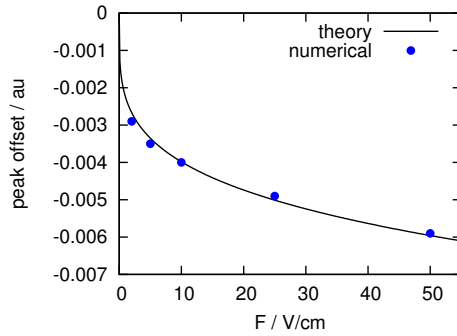


Figure 6.12: Scaling of the ZES peak position with extraction field strength. The theoretical value $-0.6F^{1/4}$ is compared to simulated results.

changing the value of the extraction field strength F .

Fig. 6.11 shows the momentum spectra in p_z , i.e. integrated over a narrow range p_x and p_y , for three different field strengths and the setup of Fig. 6.15 of an extraction field perpendicular to the laser polarization. The axes have been scaled according to Eq. (6.3), in order to illustrate the generality of the peak shape. Then all three spectra lie on top of each other, confirming the overall scaling. The integration limits in other directions are also scaled: here, the scaled limit $|p| \leq 0.1$ was used for p_x and p_y . Since the peak is centered on the z -axis choosing different limits will not affect its location much, but the shape may change slightly. For direct comparison, the proper scaling should be applied for all coordinates.

The excellent agreement between the curves of Fig. 6.11 shows that the laser-driven motion is indeed unimportant for the ensuing extraction dynamics. Only the latter can be rescaled by Eq. (6.3); the length- and momentum scales of the laser driven electron is the same for all field strengths in real coordinates; hence in scaled coordinates they are different in each case. Since time is also scaling according to Eq. (6.5), we are effectively changing both laser wavelength

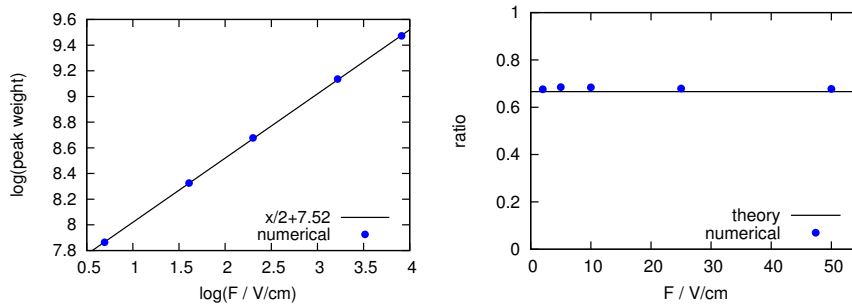


Figure 6.13: Left: Scaling of the number of ionized states with field strength. Theoretically a slope of $1/2$ is expected. Right: Ratio of ionized states to initially occupied ones in $-2 \leq E \leq 0$. A small, almost constant offset from the value $2/3$ predicted by Eq. (6.16) is observed, pointing to a somewhat non-flat distribution of β .

and intensity in the scaled problem for each different extraction field strength. That the universal shape of Fig. 6.11 survives untouched is clear evidence for the separation of the two processes.

Another feature of Fig. 6.11 is the second peak located around $p_z = -3$. While much weaker than the main peak, it is visible and corresponds to the peak close to $p_z^{(m)} = -3$ in Fig. 6.9. Due to its weakness it may be hard to detect experimentally; it would however give strong support to our model if observed.

The location of the momentum peak (in real, unscaled coordinates) is shown in Fig. 6.12. The theoretical curve is obtained by combining the $F^{1/4}$ -scaling of Eq. (6.3) with the absolute peak location in scaled coordinates, approximated as $p_z \approx -0.6$. This value was extracted from Fig. 6.11.

6.5.2 Scaling of energy

In simulation the number of escaped electrons can simply be counted and is plotted as function of field strength is shown in Fig. 6.13. Since the absolute scale has no meaning here it is plotted as a log-log plot, so that the square-root behaviour of Eq. (6.4) gives a line with slope 0.5. Such a line fits the simulated points extremely well, confirming the energy scaling $\sim F^{1/2}$.

The number of liberated electrons divided by the total number of electrons in the energy range $(-2\sqrt{F}, 0)$ is also shown in Fig. 6.13 and roughly agrees with the value $2/3$. The small, but systematic, offset is caused by the nonhomogeneous distribution of β -values. The β -distribution is almost independent of energy, so the small correction necessary is the same for all field strengths, giving a constant shift of the numerical points.

Numerically also the measured energy spectrum can be compared before and after the extraction. (We mean here the *detected* energy; the physical energy is of course constant.) It is shown in Fig. 6.14. The flat pre-extraction (and physically correct) spectrum is distorted, and a narrow peak is formed above threshold with a corresponding dip below it. Note however that not all states are ionized; there are still populated states in the region $E \in (-2, 0)$, in direct correspondence to Fig. 6.8.

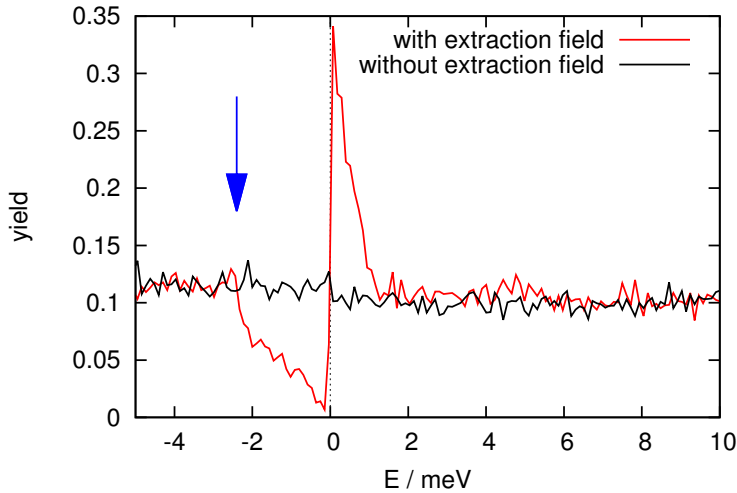


Figure 6.14: Example of a spectrum with and without inclusion of the extraction field. The arrow points to the barrier value $E = -2\sqrt{F}$.

In an experiment, the peak above threshold is certainly measurable, and since it is sitting on a constant background, its area could be determined. This area then directly corresponds to the area missing in the "dip" region below threshold. The ZES could in this way be used to gain information about the occupation of Rydberg states after FTI. Unfortunately, in the experiments described in Section 6.6 the energy spectra were not detailed enough for a reliable analysis. The idea was however put forward in [73], where a discrepancy between their experimentally measured ZES weight and their theoretically expected one can be explained exactly by a failure of taking the factor $3/2$ into account.

6.6 Comparison with experiment

The scaling of the ZES momentum peak was measured experimentally in a collaborative work [8]. The offset from zero was measured by orienting the extraction field perpendicular to the laser polarization axis. Due to the cylindrical symmetry of the laser-induced process, the distribution of higher energy electrons (not significantly influenced by the extraction field) must be symmetric around the polarization axis; the offset of the ZES from this axis can then be measured very accurately. This breaks however the cylindrical symmetry of the full problem.

A typical measurement result together with a corresponding simulation is shown in Fig. 6.15. In order to increase the contrast the experiment was done at laser wavelength of 800 nm, in a regime where the CTMC simulation does not reproduce overall features well. The symmetry axis and ZES is however clearly visible and makes a comparison possible. The agreement illustrates that the details of the laser driven motion is not important for the ZES peak formation.

The scaling of the peak location with field strength is shown in Fig. 6.16. There is no parameter fitting involved; the curve comes directly from theory, while the experimental dots are the direct measurement results. While agree-

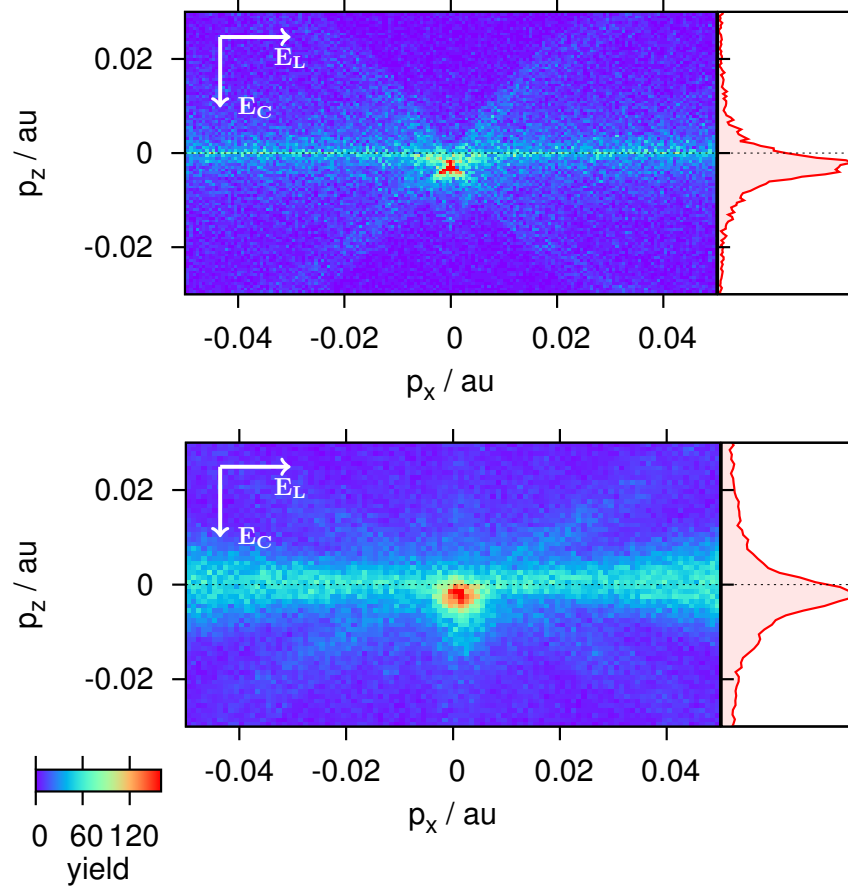


Figure 6.15: Comparison of the ZES in simulation (top) and experiment (bottom). Laser wavelength $\lambda = 800$ nm, polarization perpendicular to the extraction field. Only momenta with $|p_y| < 0.01$ are recorded. For the marginal spectra, an integration interval $|p_x| < 0.005$ was used.

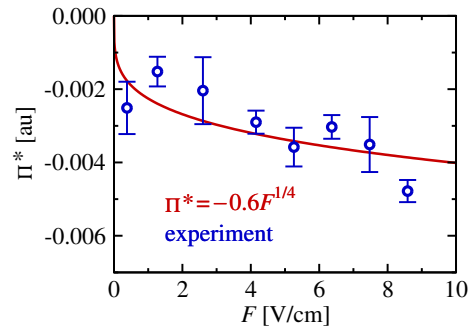


Figure 6.16: Position of the ZES peak as function of field strength, theoretical (curve) vs. experimental (dots). Π^* denotes the momentum of the ZES peak, with the value -0.6 in scaled coordinates and the scaling $F^{1/4}$ with the field strength. From [8].

ment is not perfect, it is a strong indication that Stark dynamics is at play, and that the model described here is the mechanism behind the peak, as conjectured in Section 6.2.

6.7 Quantum effects

The separation of variables used here is identical to the one used when describing the strong-field tunneling process (Section 2.3.2) [38]. Physically, quantum tunneling must certainly be possible also in the case of a constant field. The very weak fields involved in the extraction process makes this a highly improbable event that can be neglected.

This is seen by studying the scaling of the action corresponding to Eq. (6.3):

$$S = \int \mathbf{p} \cdot d\mathbf{q} = F^{-1/4} \int \mathbf{p}' \cdot d\mathbf{q}' .$$

The intermediate step between quantum mechanics and classical mechanics is semiclassics, where the idea is to assign a phase given by $\exp(-iS/\hbar)$ to each classical trajectory. Changing the field strength and seeing how the phase changes in this expression, is then equivalent to scaling \hbar according to

$$\hbar = F^{1/4} \hbar'$$

so in the weak field limit, \hbar similarly gets smaller, leading to a suppression of quantum effects. The semiclassical aspects of the Stark problem for field-ionized trajectories has been studied extensively [95–97], showing excellent agreement with experiments [98–100]. Interference structures from field ionization was seen at field strengths around $F \sim 1$ kV/cm. At our field strengths 1 – 10 V/cm \hbar is about 3 – 5 times smaller, and the interference patterns will be accordingly denser and harder to resolve. Mainly however the classical trajectories were found to describe the dynamics very accurately [100], supporting our fully classical treatment.

We can estimate the breakdown of classical mechanics by using the analytical expression for p_ξ in Eq. (6.10). Quantum tunneling and reflection could happen close to the ionization barrier in ξ , for energies close to -2 . A quantitative measure of the "quantumness" of a trajectory is given in semiclassical theory by the quantality function [101, 102] (sometimes referred to as the "badlands function"):

$$Q = \hbar^2 \left(\frac{3 p'^2}{4 p^4} - \frac{p''}{2 p^3} \right) \quad (6.17)$$

It is shown in Fig. 6.17, using the momentum at the barrier, $p = p_\xi(1)$, where quantum effects are most severe, for a field strength of $F = 10$ V/cm. Changing the field strength means scaling the y -axis by $F^{1/4}$. In practice therefore the extraction fields used, in the range of 1 – 10 V/cm, will only slightly modify Fig. 6.17. The arrows are pointing to the β -values corresponding to the first and second return to $p_\rho^{(m)} = 0$, for each energy. It is seen that, at least for the first two returns, the quantality functions stays well below 1, so that a classical treatment is very accurate. Further, the interval of significant quantum behaviour is limited to a narrow range around $\beta = E^2/2 - 1$ (i.e. close to the

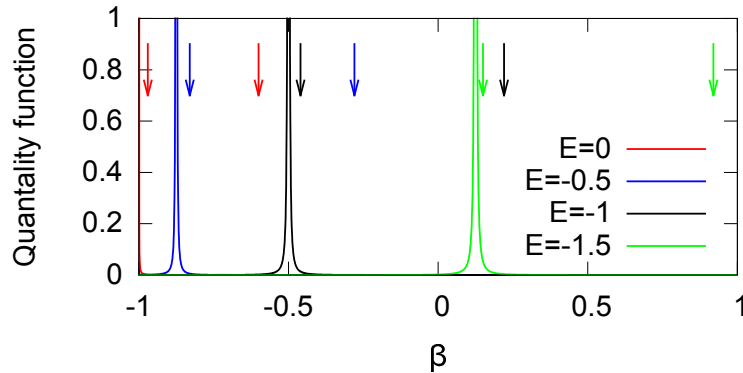


Figure 6.17: The quantity function of Eq. (6.17) for $F = 10$ V/cm, evaluated at the barrier top $\xi = 1$. Arrows point to the β -values giving the first two returns to $p_\rho^{(m)} = 0$ for the corresponding energies.

barrier), so the trajectories in that range will only give small contributions to the spectrum and the classical features coming from the large over-the-barrier region, is dominating the final spectrum.

All in all, the prominent *classical* features that do arise will not be destroyed by a small quantum correction - semiclassically they form the basics of the spectrum, with interferences modifying them. This agrees with the conclusion of [100].

6.8 Summary

The hypothesis presented in Section 6.2 is supported by simulation results, where inclusion of the extraction field leads to a ZES in the measurement. Due to separation of time and energy scales, the extraction step is reduced to Stark motion, obeying the general scaling Eq. (6.3) and leading to a peak in the momentum spectrum, as shown in Fig. 6.9. The peak location together with the scaling agrees with simulation results of the full problem for a large range of extraction field strengths, and shows reasonable agreement with experimental results, without any free parameters. It was further shown that measuring the peak weight can in principle lead to information about the population of negative energy states, that would remain bound were it not for the extraction field.

The experimental ZES is thus explained in a consistent way. At first glance this may be a negative result, since the ZES is created by the experimental detector and does not indicate any unknown physical process. There are however more positive aspects as well. Firstly, it does not signal a breakdown of the description in use of the laser driven ionization, so that the understanding of that process remains intact. Secondly, the presence of a ZES in a measurement indicates that Rydberg states were populated by the laser-atom interaction, with energies above $E = -2\sqrt{F}$ where ionization by the extraction field is possible. It is therefore a probe of high-lying Rydberg states, and could be used to obtain additional information about the final energy distribution after the laser pulse. In experiments with laser ionization of atomic clusters, release of

6.8 Summary

bound electrons through an external field has been used to retrieve information about the cluster [103–105]. That the ZES has exactly the same origin suggests that similar ideas may be used.

Chapter 7

Stark dynamics

In this chapter the motion in the Stark field is discussed in detail and analytical results are obtained. The overall goal is to understand the momentum spectrum of liberated electrons Fig. 6.9. In particular the time dynamics corresponding to the measurement $p_z^{(m)}$ will be discussed, since discussions of the Stark problem typically do not address this question, while it is essential for our situation. The time development of an ensemble of trajectories is the new aspect of the Stark problem that we highlight, as discussed in Section 7.1.

The individual classical trajectories of the 2D Stark problem are known and have been described e.g. in [106] and [96]. A full discussion, including the time evolution and the 3D situation, is contained in [107]. The rich and surprisingly complex dynamics can be solved fully analytically. Since we are only interested in a limited energy range (cf. Section 6.4.3) we need not investigate all the different solutions that arise. We will outline the derivations with particular focus on how to obtain the asymptotic momentum and time delay, which show up in the ZES measurements.

7.1 Background

The interest in the Stark problem - an atom in an external electric field - dates back at least to [89], where it was seen that absorption lines of atomic spectra (the most powerful tool available to atomic physics at the time) were split and shifted when an electric field was applied to the atom. This so-called Stark effect was among the early successes of quantum mechanics [108], which could predict quantitatively the magnitude of the shift and the reason for the splitting (lifting of degeneracy due to breaking of rotational symmetry).

The Stark effect arises as an energy shift of a single atomic state; it is easily measured for low quantum numbers where different energy shells remain well separated even with the Stark shift, but gets increasingly complicated close to threshold where even a small energy splitting makes the energies overlap. Close to threshold a classical treatment gets increasingly accurate.

The tunneling induced by a weak electric field has also been used to study atomic states. The goal of this so-called ZEKE spectroscopy has been to resolve excited atomic states on a very fine energy scale, by laser excitation followed by tunneling ionization of specific Stark states. Due to the exponential dependence

of tunneling probability on energy, different energy states can be resolved very exactly by measuring the ionization time depending on the field strength. The focus has also here been on exciting one or a few states only, in order to retrieve information about them.

In the high-intensity excitation process described in this thesis, a very different energy distribution is obtained, one that is broad and almost flat across threshold. The energy scale of strong field processes is the ponderomotive energy U_p which is typically tens of eV:s, meaning that state-selective excitation is impossible. Due to the large number of photons involved, the selection rules for angular momentum also play little role, so that all available angular momenta states are typically populated. In effect, a wave packet with an energy width of several U_p and containing, for each energy, many different angular momenta, is created. This further supports the application of the classical method, which was used already for the excitation process itself in previous chapters.

Classical trajectories in a Stark field has been studied in various contexts. In atomic physics the most spectacular result is probably the observation of interference of different paths, leading to a diffraction pattern on a detector screen [100,109] as predicted by [96]. In these studies a semiclassical picture was used (classical trajectories + quantum phase) for electric fields around $F \sim 1$ kV/cm. However, the time dynamics did not have to be taken into account.

On a completely different scale, time dynamics of single trajectories have been studied. Due to Newtonian gravitation having the identical form to Coulomb attraction, the Stark situation arises in astrophysics when studying a body moving in a gravitational field, combined with a constant field. A spaceship with a constant propulsion force, pointing in a certain fixed direction in space while passing close by (or orbiting) a planet, is the typical situation. In this situation time dynamics is of interest, asking questions like: how long does it take, after switching on the engines, to escape a planet's gravitational field? Naturally the interest is however focused on single trajectories, and not ensembles of bodies as in the atomic situation.

The question: "for a given distribution of initial conditions for the Stark problem, what is the final distribution in momentum and time of escaping trajectories", seems not to have been asked before.

7.2 Stark trajectories

We pick up where the discussion ended in Section 6.4.2, stating here the relevant equations Eq. (6.10), ((6.11)) and ((6.12)) again:

$$\begin{aligned}
 p_\xi &= \frac{\partial S}{\partial \xi} = \sqrt{\frac{E}{2} + \frac{\beta}{2\xi} + \frac{1 + \xi^2/2}{2\xi}} \\
 p_\eta &= \frac{\partial S}{\partial \eta} = \sqrt{\frac{E}{2} - \frac{\beta}{2\eta} + \frac{1 - \eta^2/2}{2\eta}} \\
 S &= \int p_\xi d\xi + \int p_\eta d\eta .
 \end{aligned} \tag{7.1}$$

From the expression Eq. (7.1) we proceed by forming the derivatives of S

7.2 Stark trajectories

with respect to the two constants of motion, E and β .

$$\begin{aligned} t &= \frac{\partial S}{\partial E} = \int \frac{1}{4p_\xi} d\xi + \int \frac{1}{4p_\eta} d\eta \\ 0 &= \frac{\partial S}{\partial \beta} = \int \frac{1}{4\xi p_\xi} d\xi - \int \frac{1}{4\eta p_\eta} d\eta \\ &\implies \int \frac{1}{2\xi p_\xi} d\xi = \int \frac{1}{2\eta p_\eta} d\eta \equiv \tau \end{aligned} \quad (7.2)$$

$$t = \int \frac{\xi + \eta}{2} d\tau = \int r d\tau. \quad (7.3)$$

The definition of the "scaled time" τ is commonly called a Sundman regularization [110]. It was introduced to handle the divergency of the Coulomb potential at the origin; it falls out naturally of the treatment as the quantity which links motion in ξ with motion in η .

In order to obtain the time evolution of the problem, i.e. $\xi(\tau)$ and $\eta(\tau)$, it is necessary to invert Eq. (7.2):

$$\begin{aligned} \tau &= \int \frac{1}{2\xi p_\xi} d\xi = \int \frac{d\xi}{\sqrt{2E\xi^2 + 2\xi(1+\beta) + F\xi^3}} \\ \tau &= \int \frac{1}{2\eta p_\eta} d\eta = \int \frac{d\eta}{\sqrt{2E\eta^2 + 2\eta(1-\beta) - F\eta^3}} \end{aligned} \quad (7.4)$$

and then find the time t from Eq. (7.3). Eq. (7.4) have the form of elliptic integrals [106], so their inverse will be (combinations of) elliptic functions [111].

Depending on how the roots of the polynomial under the square root sign in Eq. (7.4) are distributed in the complex plane, the final result takes different forms. Our interest here is limited to the case of ionizing trajectories, starting at the origin, below the field-free ionization threshold $E = 0$. This corresponds to a single case. Referring to Appendix D for details on the calculation, we state here the results

$$\begin{aligned} \xi(\tau) &= \lambda_\xi^2 \frac{1 - \text{cn}(\lambda_\xi \tau | m_\xi)}{1 + \text{cn}(\lambda_\xi \tau | m_\xi)} \\ \eta(\tau) &= B \text{sd}^2(\lambda_\eta \tau | m_\eta) \end{aligned} \quad (7.5)$$

where

$$\begin{aligned} \lambda_\xi &= [2(1+\beta)]^{1/4} \\ m_\xi &= \frac{1}{2} - \frac{E}{2\lambda_\xi^2} \\ \lambda_\eta &= \frac{1}{\sqrt{2}} [E^2 + 2(1-\beta)]^{1/4} \\ m_\eta &= \frac{1}{2} + \frac{E}{4\lambda_\eta^2} \\ B &= \frac{1-\beta}{\sqrt{E^2 + 2(1-\beta)}}. \end{aligned}$$

sd and cn are Jacobi elliptic functions [78].

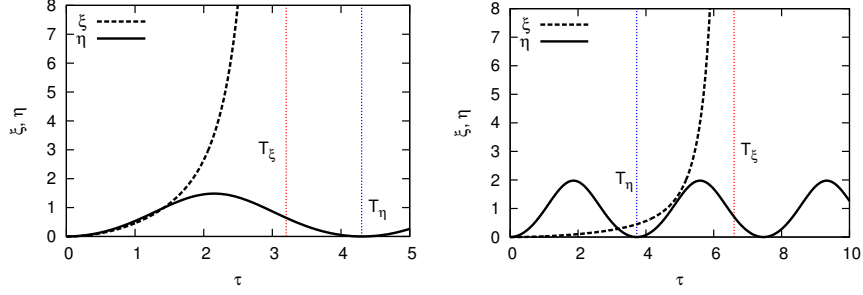


Figure 7.1: Two examples of evolution of ξ and η as functions of the scaled time τ .

The motion starts at the origin, $\xi = \eta = 0$. It is characterised by the two times

$$T_\xi \equiv \frac{2K(m_\xi)}{\lambda_\xi}; \quad \xi \longrightarrow \infty \text{ as } \tau \longrightarrow T_\xi$$

$$T_\eta \equiv \frac{2K(m_\eta)}{\lambda_\eta}; \quad \eta(\tau) = \eta(\tau + T_\eta)$$

with $K(m)$ the complete elliptic integral of the first kind. Motion is periodic in η , while it is monotonously increasing in ξ , diverging in a finite scaled time $\tau = T_\xi$. Typical plots are shown in Fig. 7.1.

7.3 Obtaining the measured momentum

Our main interest is the measured momentum $(p_\rho^{(m)}, p_z^{(m)})$. Far away from the ion motion is like that in a constant field only; the Coulomb potential no longer affects the escaping particle. We see by direct derivation that

$$p_\rho = \dot{\rho} = \frac{\xi\dot{\eta} + \eta\dot{\xi}}{2\sqrt{\xi\eta}}$$

$$p_z = \dot{z} = \frac{\dot{\xi} - \dot{\eta}}{2} \quad (7.6)$$

with the inverse

$$\dot{\xi} = \frac{\rho\dot{\rho} + z\dot{z}}{r} + \dot{z}$$

$$\dot{\eta} = \frac{\rho\dot{\rho} + z\dot{z}}{r} - \dot{z}. \quad (7.7)$$

Asymptotically the constant-field motion can be expressed as

$$\dot{z} \sim t$$

$$z \sim t^2/2$$

and $\rho/r \rightarrow 0$, $z/r \rightarrow 1$. Eq. (7.7) then gives

$$\dot{\xi} \longrightarrow 2\dot{z} \sim 2t$$

$$\dot{\eta} \longrightarrow 0$$

7.3 Obtaining the measured momentum

so that we can write

$$\dot{\xi} \longrightarrow 2t \sim 2\sqrt{2z} \sim 2\sqrt{\xi} .$$

This together with Eq. (7.6) gives in turn the asymptotic expressions for p_ρ and p_z in terms of the parabolic coordinates

$$\begin{aligned} p_\rho &\longrightarrow \frac{\dot{\xi}\eta}{2\sqrt{\xi\eta}} = \sqrt{\eta} \\ p_z &\longrightarrow \frac{\dot{\xi}}{2} = \sqrt{\xi} \end{aligned} \quad (7.8)$$

We are interested in detection at a very large distance ξ . We therefore can take the detector position at $\xi \longrightarrow \infty$, so that detection happens at $\tau = T_\xi$. The measured p_ρ is then obtained using Eq. (7.8) and Eq. (7.5); it can be written explicitly as

$$p_\rho^{(m)} = \sqrt{B} |\text{sd}(\lambda_\eta T_\xi | m_\eta)| . \quad (7.9)$$

Note that

$$p_\rho^{(m)} = 0 \implies \lambda_\eta T_\xi = 2nK(m_\eta) \implies T_\xi = T_\eta . \quad (7.10)$$

For the measured p_z , it is not enough to consider the evolution in τ , since the experimental measurement concerns the time of flight. Hence we need to compute the physical flight time t , and compare to the reference flight time t_{ref} without the Coulomb field. As is shown in Appendix D.3, it is possible to obtain the time delay from the integration of Eq. (7.3), with the expressions Eq. (7.5) inserted, by removing the field-free escape time. This results in the time delay

$$t^{(m)} = \lambda_\xi (K(m_\xi) - 2E(m_\xi)) + \frac{A}{\sqrt{2}} \left(\frac{E(\text{am}u | m_\eta) - m_{\eta 1} u - m_\eta \text{sn}u \text{cd}u}{m_\eta m_{\eta 1}} \right) \quad (7.11)$$

where

$$\begin{aligned} u &= 2 \frac{\lambda_\eta}{\lambda_\xi} K(m_\xi) \\ A &= \frac{1 - \beta}{(E^2 + 2(1 - \beta))^{3/4}} \end{aligned}$$

and the parameter of the elliptic functions in Eq. (7.11) is m_η . Finally then

$$p_z^{(m)} = -t^{(m)} . \quad (7.12)$$

We note that the time delay takes a simpler form in the case $\beta = 1$ (motion straight in the "downhill" field direction)

$$t^{(m)}(\beta = 1) = \sqrt{2}(K(m_\xi) - 2E(m_\xi)) \quad \text{with } m_\xi = 1/2 - E/4 \quad (7.13)$$

and in particular this gives the minimal time delay, for $E = 0 \implies m_\xi = 1/2$:

$$t^{(m)}(\beta = 1, E = 0) = \sqrt{2}(K(1/2) - 2E(1/2)) = -\sqrt{\frac{2}{\pi}} \Gamma^2\left(\frac{3}{4}\right) \approx -1.2$$

where we have used the general identity $K(1/2) - 2E(1/2) = -\Gamma^2(3/4)/\sqrt{\pi}$ [78].

With Eq. (7.9) and Eq. (7.11)-(7.12) we now have the final measured momentum as a function of the initial conditions E and β .

The successive build up of the momentum spectrum, as the initial conditions E and β are varied, is shown in Fig. 7.2. The final result is the distribution shown in Fig. 6.9. Due to intersection of lines with constant E , a pronounced caustic structure is formed, giving a peak in the spectrum.

The motion is illustrated by a few representative trajectories in Fig. 7.3.

7.4 Periodicity in the measured momentum spectrum

The presence of periodic orbits in a dynamical system gives it a structure, and often a lot of the dynamics can be understood by studying them. Here the periodic orbits of the Stark problem stand in direct correspondence to the final shape of the momentum spectrum.

The periodic behaviour of the momentum spectrum can be analyzed by the analytic expressions. For this consider for each energy $E \in (-2, 0)$ the value of β separating bound and free motion:

$$E = -\sqrt{2(1+\beta)} \implies \beta = \frac{E^2}{2} - 1 .$$

At this specific $\beta(E)$ there exists a single trajectory with motion purely in η , sitting on top of the barrier in ξ with a constant value $\xi = |E|$. These trajectories form a specific family of periodic orbits which we call barrier orbits. They are inaccessible in our problem due to our initial condition $\mathbf{r}_0 = 0$; they nevertheless shape the motion of neighbouring trajectories. It is clear that trajectories spending a long time in the potential before escaping do so with ξ close to the barrier, where motion in ξ is slow. They can make several oscillations in η during this time, essentially approximating the barrier orbit before escaping. The period of the single barrier orbit therefore characterises the period of the structure in the momentum spectrum. Approaching the barrier orbits:

$$\begin{aligned} \lambda_\eta &\longrightarrow \frac{1}{\sqrt{2}}[2(1+\beta) + 2(1-\beta)] = 1 \quad \text{as } \beta \rightarrow E^2/2 - 1 \\ m_\eta &\longrightarrow \frac{1}{2} + \frac{E}{4} \\ T_\eta &\longrightarrow 2K\left(\frac{1}{2} + \frac{E}{4}\right) \\ B &\longrightarrow 1 - \frac{E^2}{4} \\ \eta(T_\xi) &= Bsd^2\left(T_\xi\left|\frac{1}{2} + \frac{E}{4}\right.\right) \end{aligned}$$

The period of a barrier orbit in physical time t can be calculated, as shown in Appendix D.4

$$T_E = \int_0^{T_\eta} \frac{\xi(\tau) + \eta(\tau)}{2} d\tau = -2K(m_\eta) + 4E(m_\eta) ; \quad (7.14)$$

7.4 Periodicity in the measured momentum spectrum

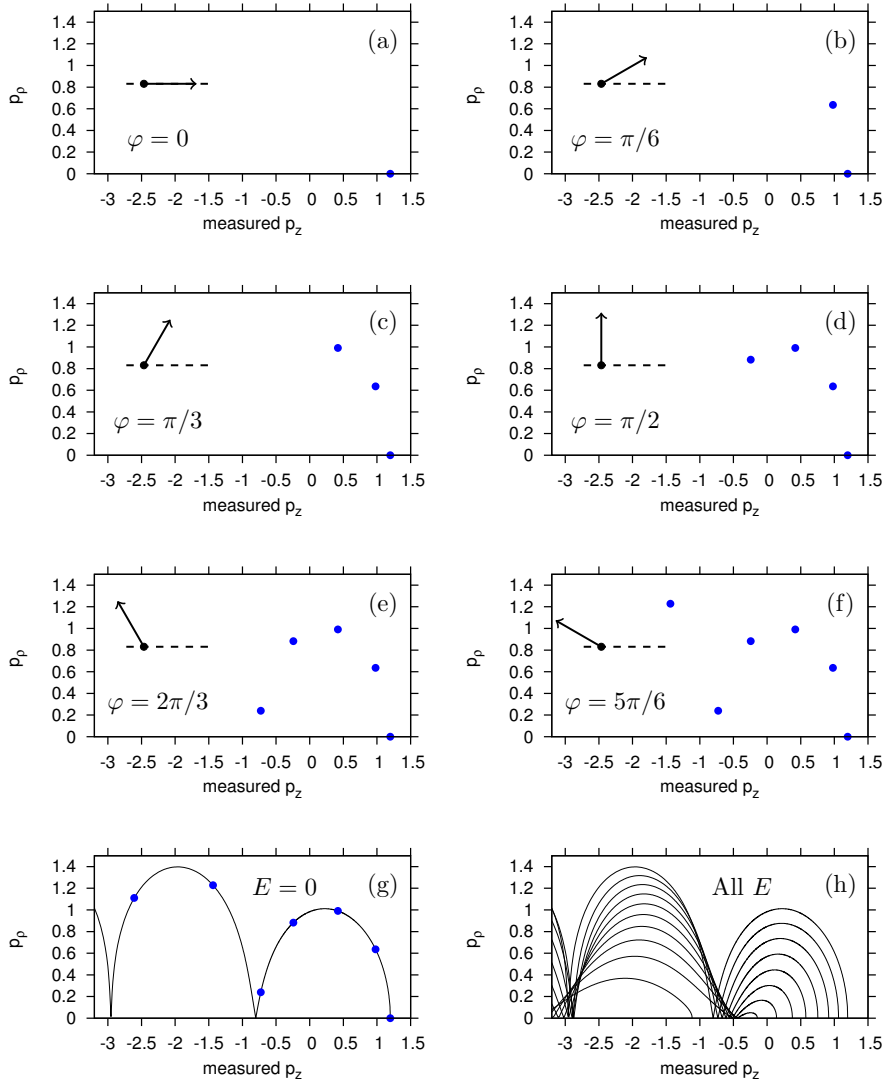


Figure 7.2: Development of the caustic structure. (a)-(f) shows the final momentum for $E = 0$ and the initial angle indicated. In (g) a line is drawn for all initial angles (i.e. all β) for $E = 0$, and (h) shows similar lines for several constant energies. Caustics are formed when the lines intersect around measured $p_z \approx -0.6$ and $p_z \approx -3$.

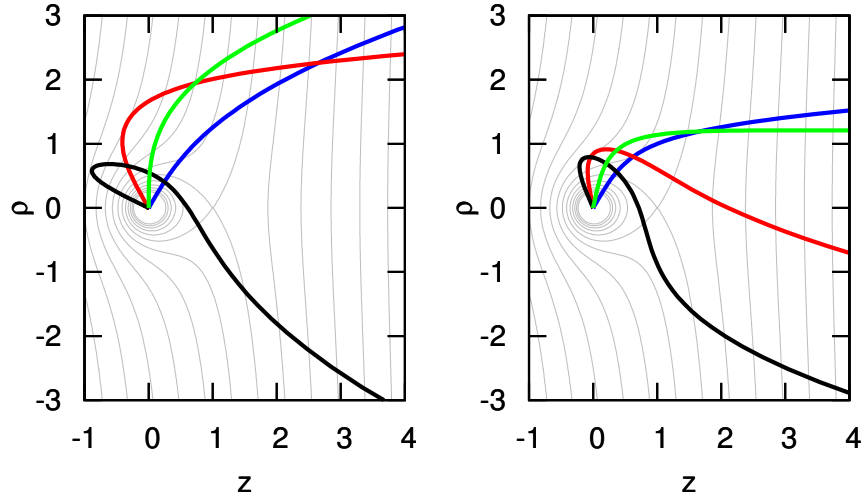


Figure 7.3: Escaping trajectories. Left: $E = 0$, right: $E = -1$. Note how, at the lower energy, a smaller ejection angle gives qualitatively similar motion.

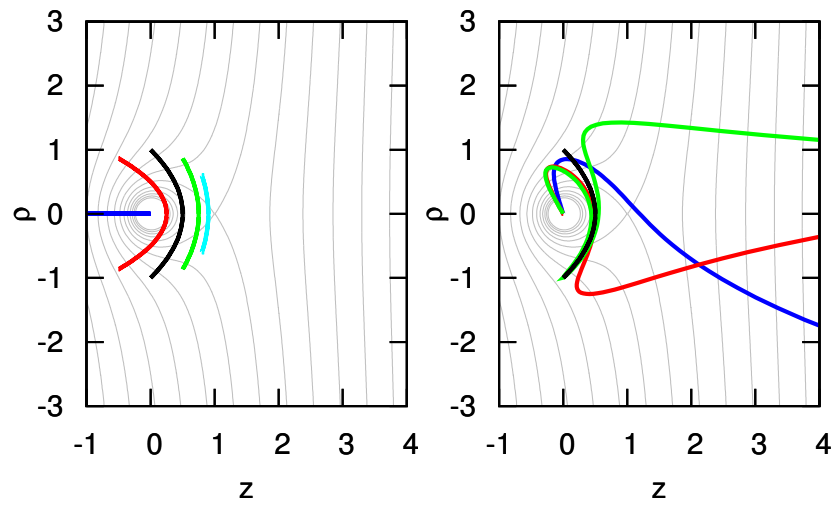


Figure 7.4: Left: Barrier orbits for different energies (blue $E = 0$, red $E = -0.5$, black $E = -1$, green $E = -0.5$, cyan $E = -0.8$). (b) Trajectories for $E = -1$, ending up in three consecutive lobes in measured momentum spectrum, increasingly approximating the barrier orbit (black).

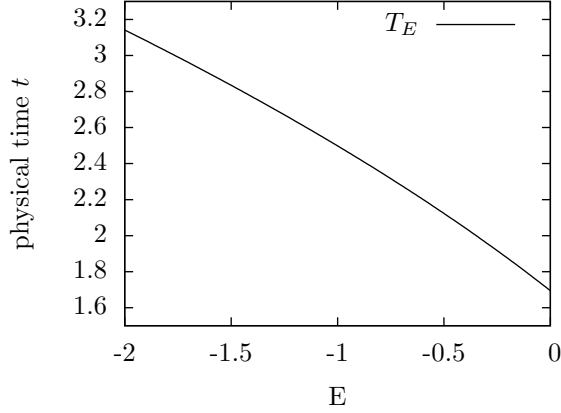


Figure 7.5: Period of the barrier orbit as function of energy, from Eq. (7.14). (Scaled units.)

an expression similar in form to Eq. (7.13) for the forward-direction trajectories.

We can now understand the periodic structure of Fig. 6.9. Successive periods are created by trajectories that, due to $\beta \rightarrow E^2/2 - 1$ spend increasing time approximating the barrier orbit. The period from Eq. (7.14) is shown in Fig. 7.5. It corresponds well to the distance between the first and second returns, indicating that already then one is in the asymptotic region. Plotting a few corresponding trajectories in Fig. 7.4b illustrates this point further.

Fig. 6.9 (and equivalently Fig. 7.2h) is thus characterised on the one hand by Eq. (7.13), giving the maximum $p_z^{(m)}$ of each constant energy (and in particular the overall maximum, for $E = 0$), and on the other hand by the characteristic period for each energy, given by Eq. (7.14) corresponding to the barrier orbit. This also indicates that the periodic structure will deteriorate for long delay times, since the periods are not identical for different energies. They are however close enough that the first few returns are almost "in phase" and produce spectral peaks.

7.5 Analytic expressions

We collect here a few analytical expressions that can be found describing the features of Fig. 6.9. Unfortunately the location of the main peak (the ZES) at $p_z \approx -0.6$ cannot be obtained exactly through an analytical treatment. However, in particular for the special case $E = 0$, the expressions simplify and a few characteristic values can be written down.

$$p_\rho^{(m)} = 0 \text{ for } E = 0$$

For $E = 0$ we have $m_\xi = m_\eta = 1/2$ so that Eq. (7.10) gives

$$T_\xi = nT_\eta \implies \lambda_\eta = n\lambda_\xi \implies (1 - \beta) = 4n^4(1 + \beta)$$

so that the asymptotic motion is purely along z if

$$\beta = \frac{1 - 4n^4}{1 + 4n^4}$$

and the time delay for these trajectories simplifies to

$$t^{(m)} = -\frac{\sqrt{2}}{\sqrt{\pi}}\Gamma^2\left(\frac{3}{4}\right)\frac{1 - 2n^2}{(1 + 4n^4)^{1/4}}.$$

This can be used to approximate the location of the peaks along the $z = 0$ axis. Note that the prefactor is the period T_E of the barrier orbit, since $K - 2E = -\Gamma^2(3/4)/\sqrt{\pi}$, and the second factor $\rightarrow n$ for large n , giving the expected asymptotically periodic behaviour.

Limit for E such that η completes at least one period

For $\beta = 1$, we have $\lambda_\xi = \sqrt{2}$, $\lambda_\eta = \sqrt{|E|/2}$, $m_\xi = 1/2 - E/4$ and $m_\eta = 0$ so that the condition $T_\xi = nT_\eta$ reduces to

$$\sqrt{|E|}K\left(\frac{1}{2} - \frac{E}{4}\right) = 2K(0) \cdot n = n\pi.$$

For $n = 1$ this gives $E = -1.55$. For lower energies there is no β which can fulfill the condition, meaning that an asymptotic value of $\eta = 0$ is only possible after one oscillation in η is completed - i.e. there are no trajectories escaping without crossing the z -axis. In [100] this was called a limit for direct electrons. The measured momentum for this energy is $p_z^{(m)} = -1.41$, thus marking the on-axis beginning of the caustic structure in the final momentum spectrum. In [100], where a narrow range of energies were excited and only $p_\rho^{(m)}$ and not $p_z^{(m)}$ was measured, a bright spot was reported close to this energy, clearly manifesting the same divergence as that seen in Fig. 6.9.

7.6 Summary

The fact that the motion in a combined constant electric field and a Coulombic potential can be treated analytically gives insight into the development of the spectral features contributing to the ZES. The exact expressions for the trajectories and the time delay give an immediate connection between the initial conditions (E, β) and the observed momentum spectrum $(p_\rho^{(m)}, p_z^{(m)})$, where as before $p_z^{(m)}$ is really not a momentum measurement but the negative time delay in escaping the Coulomb potential. In particular the apparent periodicity of the momentum spectrum is seen to stem from the presence of periodic orbits. Unfortunately the conditions for a divergence in the spectrum can in general only be written implicitly. For $E = 0$ the expressions simplify and the conditions giving $p_z^{(m)} = 0$ can be given in explicit form. Further the divergent ZES structure is related to the necessity of indirect ionization, with trajectories making at least one oscillation in η before escaping. That a divergence is known to occur experimentally in pure p_ρ -measurements [100] for the corresponding energy connects the peak found here with previously described aspects of Stark motion.

Chapter 8

Summary and outlook

This thesis has treated two features of modern day strong-field ionization experiments using IR lasers and momentum imaging of electrons. The low energy structure is by now an established experimental result. Probing more extreme laser parameters - in particular shorter pulses - is an experimental challenge, meaning that a sufficiently complete theoretical understanding is a prerequisite for finding interesting parameter ranges, and deciding which experiments could contribute to a progress in understanding.

The classical trajectory model was shown in Chapter 3 to give very accurate predictions of the LES peak energy for the mid-IR laser regime. This supports the overall validity of classical modelling of IR driven electron motion in general and the three-step trajectory model in particular. The general scaling with pulse length and ponderomotive energy, as illustrated in Fig. 3.9 by the different targets and intensities used, comes naturally from the three-step model.

Chapter 4 shows that each LES stems from a critical line in the initial phase space, resulting in a caustic in the final momentum spectrum. It is formed during a soft recollision at around ~ 20 au distance from the ion, and its shape can be reproduced by an analytical model. That the electron never comes close to the ion, and that furthermore the recollision distance scales very slowly with laser parameters as seen in the model, shows the validity of a universal classical recollision model, since the internal structure of the ion plays a negligible role at the relevant distances.

The analytical results of Chapters 4 and 5 are supported by numerical simulations and consistent with available experimental results.

The validity of the model is restricted to wavelengths in the approximate span $1 \mu\text{m} < \lambda < 3.2 \mu\text{m}$ for an intensity of $I = 10^{14} \text{ W/cm}^2$. The lower limit comes from the onset of discrete ATI peaks in the spectrum overshadowing the LES, and the fact that the recollision model is less valid the shorter the wavelength gets. The upper limit comes from a breakdown of the dipole approximation, so that the Lorentz force drives the electron trajectories away from those of the model. This effect grows gradually and depends on the intensity. However for a large span of laser parameters where present strong-field experiments take place the model is valid and is expected to give quantitative predictions of the peak locations.

Several interesting experimental investigations are suggested by the LES results of this thesis. Using even shorter pulses (1-2 cycles), and in particular

detectors capable of measuring energies down to threshold, could possibly resolve the VLES and clarify its formation. In order to resolve the higher order LES and VLES it is desirable that U_p be large, since this increases the overall scale of the features. Measuring the full 2D momentum distribution using the reaction microscope setups presently available, together with a few-cycle pulse duration, is expected to show the caustic structures clearly, since their contrast increases in an ultrashort pulse where ionization takes place predominantly during the center half laser cycle. One could then see a single, clear caustic and possibly even resolve the cusp structures, though quantum mechanical effects will smoothen its appearance.

However as seen in Chapter 5 extreme parameters are not necessary, and the transverse structure of the LES, in particular the maximum given by Eq. (4.14), could be measured in rather long pulses at a wide range of U_p . It may even be beneficial to use a shorter wavelength since this increases the contrast due to the narrower overall energy distribution, so that less ionization events are necessary for a high precision measurement. Using the setup of Fig. 5.15 (which was used in [82]) coupled with high precision 2D momentum measurement could resolve the transverse peak and furthermore show how the prolongation of the VLES and LES caustics form the fork structure and joins onto the rings coming from the elastic collisions discussed in [82].

The understanding of the LES caustic formation and the soft recollision event may open doors to using the LES as a probe of the properties of the ion itself. Since the trajectory and recollision models are equally valid for small molecules, strong field ionization of a molecule with an internal structure may lead to a perturbed LES. Since the shape of the LES does not depend on the tunneling probabilities but on the dynamics, the effect of the molecule's structure on the tunneling event could be disentangled from its effect on the recollision.

The zero energy structure is shown in Chapter 6 to result from a weak external electric field ionizing Rydberg states that were created by the strong field interaction. Its features are universal: they result from Stark dynamics, as described in Chapter 7, and will result from any broadband excitation of the energies between the field ionization threshold and the field-free threshold. The combined measurement of final transverse momentum and time-of-flight is necessary for the shape described here; the time delay gives the characteristic peak location. The ionization of Rydberg states by a weak external field has previously been used to study clusters. With the ZES resulting from such states, its presence shows that the laser-atom interaction populated Rydberg states, while its absence indicates that no such states were populated, or that they decayed by other means before the electron could escape over the field-induced threshold. Its possible use in connection with the study of autoionizing states [74] should be mentioned.

The Stark dynamics gives a direct image of the initial distribution, created by the laser, on the measured momentum. With increased precision and/or stronger extraction fields, this could possibly be used to get a glimpse of the initial distribution. The features of the final momentum distribution will shift around as the initial distribution changes, although not so sensitively as to be seen in the current results. Such a measurement could include varying the angle between the laser polarization axis and the extraction field direction, and studying how the ZES structure changes. Another possibility would be to use an ultrashort laser pulse so as to create an asymmetric initial distribution.

Appendix A

Classical spectra

A.1 Basic theory

The state of a system in Hamiltonian mechanics is described by a point in phase space; the set of all possible generalized coordinates \mathbf{q} and generalized momenta \mathbf{p} . If configuration space is n -dimensional, the dimension of phase space is $2n$. For simplicity, we assume in the following that the configuration space is \mathbb{R}^n . We can write the time evolution of a specific state $(\mathbf{q}', \mathbf{p}')$ formally using the flow g :

$$g_t : \mathbb{R}^{2n} \rightarrow \mathbb{R}^{2n} \\ (\mathbf{q}', \mathbf{p}') \mapsto (\mathbf{q}, \mathbf{p})$$

where the evolution at each instant is governed by Hamilton's equations of motion

$$\dot{\mathbf{q}} = \frac{\partial H}{\partial \mathbf{p}} \\ \dot{\mathbf{p}} = -\frac{\partial H}{\partial \mathbf{q}} .$$

In atomic physics one typically does not measure single trajectories, but rather an ensemble of trajectories corresponding to e.g. evolution of an initially bound state wave packet. One thus computes the evolution of a probability density in phase space.

In this view the outcome of a single measurement (e.g. of particle energy) is a stochastic variable, distributed according to some final distribution (e.g. the energy spectrum). A large number of single measurements are done, giving information about the full distribution.

Several notations are in use; in probability theory one typically writes $f_X(x)$ for the probability density of the stochastic variable X taking a value (in a small neighborhood of) x . We will mostly use the simpler notation

$$w(x) = f_X(x) .$$

Denote the full state vector in phase space by \mathbf{x} :

$$\mathbf{x} = (q_1, \dots, q_n, p_1, \dots, p_n) \in \mathbb{R}^{2n} .$$

The probability density w_t of the ensemble at time t is then calculated from the initial ensemble w_0 as

$$w_t(\bar{\mathbf{x}}) = \int d\mathbf{x}' w_0(\mathbf{x}') \delta(\bar{\mathbf{x}} - g_t(\mathbf{x}')) = \int d\mathbf{x}' w_0(\mathbf{x}') \left| \frac{\partial g_t}{\partial \mathbf{x}'} \right|^{-1} \delta(\mathbf{x}' - g_t^{-1}(\bar{\mathbf{x}})). \quad (\text{A.1})$$

\mathbf{x}' denotes initial variables; $\bar{\mathbf{x}}$ a specific value of the final coordinate, and $\frac{\partial g_t}{\partial \mathbf{x}'}$ is the Jacobian of the mapping g_t . This Jacobian is the central object influencing the final spectrum, and contains the effect of the dynamics.

The probability distribution of a scalar observable, i.e. the energy E or a single momentum p_i , given as a function of the state of the system $E = E(\mathbf{x})$, is similarly given by

$$w_t(\bar{E}) = \int d\mathbf{x} \delta(\bar{E} - E(\mathbf{x})) = \int d\mathbf{x} \frac{1}{|\text{grad } E|} \Big|_{E(\mathbf{x})=\bar{E}}. \quad (\text{A.2})$$

where the integral is evaluated along the $6n - 1$ -dimensional subspace defined by $E(\mathbf{x}) = \bar{E}$. The two expressions Eq. (A.1) and Eq. (A.2) can be combined to give

$$w_t(\bar{E}) \int d\mathbf{x}' \frac{1}{|\text{grad}_{\mathbf{x}'} E|} \Big|_{E(g_t(\mathbf{x}'))=\bar{E}}$$

A.2 Bivariate probability distributions

A probability distribution of two stochastic variables X, Y is called a bivariate distribution. There are several different distributions that are used in the bivariate case:

Joint probability distribution

The 2D distribution of X, Y simultaneously taking specific values x, y is called the *joint* probability distribution:

$$P_{X,Y}(x, y) = P(X \in (x, x + dx), Y \in (y, y + dy))$$

Marginal probability distribution

The 1D distributions of X (Y) taking a specific value x (y), regardless of the value of the other variable, is called the *marginal* distribution.

$$P_X(x) = \int dy P_{X,Y}(x, y)$$

$$P_Y(y) = \int dx P_{X,Y}(x, y)$$

Conditional probability distribution

The 1D distribution of X (Y) taking a specific value, while the other variable has a fixed value, is called the *conditional* probability distribution.

$$P_X(x)|_{y=\bar{y}} = \frac{P_{X,Y}(x, y = \bar{y})}{\int dx' P_{X,Y}(x', y = \bar{y})}$$

A.3 2D momentum spectra

In this thesis dynamics in two dimensions is studied. Phase space is then four-dimensional. However the initial values \mathbf{q}' depend on the initial \mathbf{p}' , while the final observable is the asymptotic \mathbf{p} only, without regard to final \mathbf{q} ; we can write

$$\begin{aligned} \mathbf{p}(\mathbf{p}') &= \lim_{t \rightarrow \infty} g_t(\mathbf{p}', \mathbf{q}'(\mathbf{p}')) . \\ w(\bar{\mathbf{p}}) &= \int d\mathbf{q} w(\bar{\mathbf{p}}, \mathbf{q}) = \lim_{t \rightarrow \infty} \int d\mathbf{q} d\mathbf{p}' w_0(\mathbf{p}') g_t(\mathbf{p}', \mathbf{q}'(\mathbf{p}')) . \end{aligned} \quad (\text{A.3})$$

We thus have the bivariate situation.

Since the 2D situation arises from a cylindrically symmetric 3D case, we call the variables ρ and z . In contrast to common definition, ρ is often allowed to take on negative values, since this eases physical intuition.

By analogy with scattering problems, the final momentum, as function of initial momentum, is called the deflection function. It is useful to look at the 1D deflection functions in p_ρ and in p_z separately, i.e.

$$\begin{aligned} p_\rho &= p_\rho(p'_\rho, p'_z) \\ p_z &= p_z(p'_\rho, p'_z) \end{aligned}$$

Eq. (A.3) takes the form

$$w(\bar{p}_\rho, \bar{p}_z) = \int_{\mathbf{p}' | \mathbf{p}(\mathbf{p}') = \bar{\mathbf{p}}} dp'_\rho dp'_z w_0(p'_\rho, p'_z) \left| \frac{\partial(p_\rho, p_z)}{\partial(p'_\rho, p'_z)} \right|^{-1} . \quad (\text{A.4})$$

The central role in shaping the spectrum is played by the Jacobian of the mapping from initial to final momentum. In particular a vanishing determinant gives a divergent distribution.

The marginal distribution in p_z is similarly given by

$$w(\bar{p}_z) = \int_{\mathbf{p}' | p_z(\mathbf{p}') = \bar{p}_z} dp'_\rho dp'_z w_0(p'_\rho, p'_z) \frac{1}{|\text{grad } p_z|} .$$

Finally the (unnormalized) conditional distribution at $p_\rho = 0$ is:

$$w(0, \bar{p}_z) = \int_{\mathbf{p}' | p_z(\mathbf{p}') = \bar{p}_z, p_\rho(\mathbf{p}') = 0} dp'_\rho dp'_z w_0(p'_\rho, p'_z) \left| \frac{\partial(p_\rho, p_z)}{\partial(p'_\rho, p'_z)} \right|^{-1} \quad (\text{A.5})$$

where again the spectrum is governed by the Jacobian determinant, evaluated at initial conditions giving final $p_\rho = 0$.

A.4 Singularities in the spectrum

Of special interest are the critical points of the deflection function(s), since a vanishing gradient leads to a divergence in the marginal spectrum. In the joint probability a vanishing Jacobian determinant has the similar effect. Critical points lead to so-called van Hove singularities [112], in the case of an observable given by a scalar function, e.g. energy or a marginal momentum distribution. In a joint probability distribution, divergencies appear in the form of *caustics*.

They are commonly discussed in the context of semiclassical dynamics [113]. A caustic is the result of a generalized critical point [114], what we will call a critical line, in the initial conditions.

The study of singularities of mappings is called singularity theory, or catastrophe theory [115]. There is a wealth of mathematical results in the field, starting with the work of Morse [116, 117]. The 2D case was treated thoroughly by Whitney [118], where most of our necessary results appear in a more general context. We will in the following state some basic results, without mathematical rigour; for a detailed treatment see e.g. [119]. In particular we will discuss how the two basic 2D singularities, the *fold* and the *cusp* arise in our context, and their relation to the divergence in the derived 1D marginal distributions.

Critical points

We call a point in initial phase space \mathbf{x}_0 a critical point of the scalar observable A if

$$\text{grad } A = 0 .$$

The spectral characteristic of the critical point is given by the eigenvalues of the Hessian matrix H of A .

- $\det H > 0$: the critical point is an extremum, giving not a divergence but a cut-off in the spectrum.
- $\det H < 0$; the critical point is a saddle point, gives a divergence (in principle always visible, can however be weak)
- $\det H = 0$; the critical point is singular and gives a weak divergence in the spectrum

A.5 Critical lines and caustics

Now consider the joint probability distribution of two final observables, f and g . The function under study is denoted

$$\mathbf{f}(\mathbf{x}) = \begin{cases} f(x, y) \\ g(x, y) \end{cases}$$

and is assumed to be a smooth function. The space of initial conditions may contain chaotic regions which are not included in the discussion, since they will typically not contribute to the essential features of the spectrum if there are also regular regions present. The Jacobian matrix of the function (f, g) is denoted as J and its determinant by $|J|$.

For connection with the previous paragraph, replace f and g by p_ρ and p_z . We choose here the more general notation f and g since the results are general and can also be applied also to rotations of the final coordinates.

A divergent spectrum is obtained from Eq. (A.4) if

$$|J| = \det \frac{\partial(f, g)}{\partial(x, y)} = 0 . \tag{A.6}$$

In analogy to the critical points of a 1D mapping, this condition defines a set of critical lines in the plane of initial conditions. We use the term "critical line" for the initial values giving a zero Jacobian, and the term "caustic" for the image of that line, i.e. the final values where the spectrum is divergent.

Although naturally arising in this context, the concept of critical lines of deflection functions is not very widespread. The concept is introduced in [120] and used in e.g. [121].

A.5.1 Properties of the critical line

- The critical line cannot begin or end in a regular domain, i.e. where (f, g) is continuously differentiable. This follows since the critical line is a contour line of the smooth function $|J|$.
- One and only one critical line is passing through each nonsingular ($H_f \neq 0$) critical point of f and g . Clearly if $\text{grad } f = 0$, Eq. (A.6) is fulfilled, so that the contour line $|J| = 0$ passes through this point. Uniqueness follows since contour lines of the function $|J|$ only intersect when $\text{grad } |J| = 0$ which implies $H_f = 0$. For g the same reasoning holds.
- The previous point also holds for any linear combination of f and g . In fact since the determinant $|J|$ is invariant under rotations

$$\begin{aligned} f' &= f \cos \varphi - g \sin \varphi \\ g' &= f \sin \varphi + g \cos \varphi \end{aligned} \tag{A.7}$$

we can at any point along the critical line find new functions f', g' such that $\text{grad } f' = 0$ by rotation. If the line is parametrized smoothly by a parameter s , the rotation angle $\varphi(s)$ is a smooth function.

By the aforementioned rotation, we can in the following always assume that the critical line is caused by a singular point in the function f . The nature of the singular point cannot change suddenly, since the Hessian matrix is a continuous function along the critical line and continuous under the rotations Eq. (A.7); its determinant has to go through 0 when going from positive to negative values.

Hence the critical line has a definite character, given by the sign of the determinant of $H_{f'}$, of either extremal, degenerate, or saddle point kind.

A.5.2 Properties of the caustic

We can now translate these results to apply to the image of the critical line, i.e. the caustic. Let $\mathbf{c}(s)$ be a parametrization of the critical line \mathbf{c} . Assume $\text{grad } f = 0$ for some $s = s_0$. We can write the caustic as a function $f(g)$ close to the critical point. Its derivative is

$$\frac{df}{dg} = \frac{df/ds}{dg/ds} = 0 \text{ at } s_0 \quad \text{since } \text{grad } f(s_0) = 0 .$$

Hence the critical line runs perpendicular to the f -axis. The converse is also clear: if the caustic runs perpendicular to a coordinate axis, it must hold that $\text{grad } f = 0$, so that there is a singular point in the deflection function along that coordinate axis.

We can carry this one step further and expand the caustic around the image of the point s_0 as

$$f(s) = f_0 + \left. \frac{d^2 f}{ds^2} \right|_{s_0} (s - s_0)^2$$

$$g(s) = g_0 + \left. \frac{dg}{ds} \right|_{s_0} (s - s_0) .$$

We can now write the image of the critical line as a function $f(g)$:

$$s - s_0 = \frac{g(s) - g_0}{dg/ds} \implies$$

$$f(s) = f_0 + \left. \frac{d^2 f}{ds^2} \right|_{s_0} \left(\frac{g(s) - g_0}{dg/ds} \right)^2 = f_0 + \left. \frac{d^2 f}{dg^2} \right|_{s_0} (g(s) - g_0)^2 .$$

This means that the caustic has the shape $f \sim g^2$. This is the general shape of a *fold* [118].

Change of character

Let the Hessian be degenerate at a critical point x_0 and \mathbf{e}_1 the eigenvector associated with the zero eigenvalue. We parametrize the critical line through x_0 as $\mathbf{c}(s)$. Since

$$\text{grad } f = H(x_0)(\mathbf{x} - \mathbf{x}_0) = 0 \quad \text{along } \mathbf{e}_1 \implies$$

$$J = 0 \quad \text{along } \mathbf{e}_1 \implies$$

$$\mathbf{c}'(s) \parallel \mathbf{e}_1$$

we also have

$$\frac{d^2 f}{ds^2} = 0 .$$

We can translate this to the image of the critical line since along the line

$$\frac{d^2 f}{dg^2} = \frac{d^2 f/ds^2}{d^2 g/ds^2} = 0 \tag{A.8}$$

meaning that at a point where the character of the critical line changes, the second derivative of $f(g)$ vanishes. The converse also holds: if the second derivative $f''(g)$ vanishes, Eq. (A.8) holds, so that $d^2 f/ds^2 = 0$ which means the Hessian H_f has a zero eigenvalue associated with the direction of $\mathbf{c}'(s)$.

Thus the points where the character changes correspond to inflection points of the caustic.

At points where $\text{grad } f \parallel \text{grad } g \parallel \text{grad } |J|$, the caustic has a cusp

If the gradient of the Jacobian determinant is parallel to the gradients of the functions (which are always parallel to each other at the critical line) the parametrized critical line $\mathbf{c}(s)$ runs perpendicular to the gradients of f and g , i.e.

$$\frac{df(s)}{ds} = \frac{dg(s)}{ds} = 0 \text{ at } s_0 .$$

We can expand the image $\mathbf{f}(\mathbf{c}(s))$ around the point $\mathbf{f}(\mathbf{c}(s_0))$:

$$\mathbf{f}(s) = \mathbf{f}(s_0) + (s - s_0) \left. \frac{d\mathbf{f}}{ds} \right|_{s_0} + (s - s_0)^2 \left. \frac{d^2\mathbf{f}}{ds^2} \right|_{s_0} = \mathbf{f}(s_0) + (s - s_0)^2 \left. \frac{d^2\mathbf{f}}{ds^2} \right|_{s_0} .$$

As the parameter s is taking values going through s_0 , the critical line c makes an abrupt turn and goes back through its old trace, since the vector drawing the line is quadratic in $s - s_0$. It forms a *cusp* singularity. The limiting angle φ in the f, g -plane is found as $\varphi = \arctan(g''/f'')$.

Visibility of the caustic

The existence of the critical line does not necessarily mean that its image, the caustic, will be visible everywhere. It will typically be strongest close to the cusps, since there both f and g are changing slowly. In our LES situation this is the case. Secondly, the weight of initial condition always also come into play - if the initial probability is small, even the divergence at the caustic will not be a prominent spectral feature since it is easily drowned in the background.

We stress that the divergence is a purely mathematical result. In a real measured spectrum there is always a coarse-graining process involved, since any detector has a finite resolution. The same is true in numerical trajectory simulations, where the final spectrum is obtained by counting the number of points within a "bin" in final momentum, or by convolution with some smoothing function. If this is taken into account the divergence is regularized and instead shows up as a peak with finite height. If the caustic is very weak, this peak can then be hidden by background noise or other effects.

Appendix B

Explicit expression for $G(\varphi)$

Here we state explicit expressions for the derivatives of Φ that enter into the Jacobian and the expression $\delta\mathbf{p}$. Start by noting that

$$\begin{aligned}\frac{\partial r}{\partial \rho} = \frac{\rho}{r} = \sin \varphi & & \frac{\partial r}{\partial z} = \frac{z}{r} = \cos \varphi \\ \frac{\partial \varphi}{\partial \rho} = \frac{z}{r^2} = \frac{\cos \varphi}{r} & & \frac{\partial \varphi}{\partial z} = -\frac{\rho}{r^2} = -\frac{\sin \varphi}{r}\end{aligned}$$

so that

$$\begin{aligned}\frac{\partial \Phi}{\partial \rho} &= \frac{\partial \Phi}{\partial r} \frac{\partial r}{\partial \rho} + \frac{\partial \Phi}{\partial \varphi} \frac{\partial \varphi}{\partial \rho} = -\sqrt{\frac{2}{F}} \left\{ -\frac{1}{2r^{3/2}} \frac{\partial r}{\partial \rho} I(\varphi) + \frac{1}{r^{1/2}} \frac{\partial \varphi}{\partial \rho} I'(\varphi) \right\} \\ &= -\sqrt{\frac{2}{F}} \frac{1}{r^{3/2}} f_1(\varphi) \quad \text{where } f_1(\varphi) = -\frac{\sin \varphi}{2} I(\varphi) + \cos \varphi I'(\varphi) \\ \frac{\partial \Phi}{\partial z} &= \frac{\partial \Phi}{\partial r} \frac{\partial r}{\partial z} + \frac{\partial \Phi}{\partial \varphi} \frac{\partial \varphi}{\partial z} = -\sqrt{\frac{2}{F}} \left\{ -\frac{1}{2r^{3/2}} \frac{\partial r}{\partial z} I(\varphi) + \frac{1}{r^{1/2}} \frac{\partial \varphi}{\partial z} I'(\varphi) \right\} \\ &= -\sqrt{\frac{2}{F}} \frac{1}{r^{3/2}} f_2(\varphi) \quad \text{where } f_2(\varphi) = -\frac{\cos \varphi I(\varphi)}{2} - \sin \varphi I'(\varphi)\end{aligned}$$

and we further get

$$\begin{aligned}f_1' &= -\cos \varphi I/2 - 3 \sin \varphi I'/2 + \cos \varphi I'' \\ f_2' &= \sin \varphi I/2 - 3 \cos \varphi I'/2 - \sin \varphi I'' .\end{aligned}$$

From this $\delta\mathbf{p}$ is found directly by Eq. (4.2).

The second derivatives show similar behaviour, e.g.:

$$\begin{aligned}\frac{\partial^2 \Phi}{\partial \rho^2} &= -\sqrt{\frac{2}{F}} \left\{ -\frac{3}{2r^{5/2}} \frac{\partial r}{\partial \rho} f_1(\varphi) + \frac{1}{r^{3/2}} \frac{\partial \varphi}{\partial \rho} f_1'(\varphi) \right\} \\ &= -\sqrt{\frac{2}{F}} \frac{1}{r^{5/2}} g_1(\varphi) \quad \text{where } g_1(\varphi) = -\frac{3}{2} \sin \varphi f_1(\varphi) + \cos \varphi f_1'(\varphi)\end{aligned}$$

and similarly

$$\begin{aligned}\frac{\partial^2 \Phi}{\partial z^2} &= -\sqrt{\frac{2}{F}} \frac{1}{r^{5/2}} \left\{ -\frac{3}{2} \cos \varphi f_2(\varphi) - \sin \varphi f_2'(\varphi) \right\} \\ \frac{\partial^2 \Phi}{\partial \rho \partial z} &= -\sqrt{\frac{2}{F}} \frac{1}{r^{5/2}} \left\{ -\frac{3}{2} \sin \varphi f_2(\varphi) + \cos \varphi f_2'(\varphi) \right\} \\ \frac{\partial^2 \Phi}{\partial z \partial \rho} &= -\sqrt{\frac{2}{F}} \frac{1}{r^{5/2}} \left\{ -\frac{3}{2} \cos \varphi f_1(\varphi) - \sin \varphi f_1'(\varphi) \right\}\end{aligned}$$

It is straightforward to check that the latter two are equal. Thus

$$\begin{aligned}g_2(\varphi) &= -\frac{3}{2} \cos \varphi f_1(\varphi) - \sin \varphi f_1'(\varphi) \\ g_3(\varphi) &= -\frac{3}{2} \sin \varphi f_2(\varphi) + \cos \varphi f_2'(\varphi) = -\frac{3}{2} \cos \varphi f_1(\varphi) - \sin \varphi f_1'(\varphi)\end{aligned}$$

and we can define

$$G(\varphi) = \begin{pmatrix} g_1(\varphi) & g_3(\varphi) \\ g_3(\varphi) & g_2(\varphi) \end{pmatrix}$$

so that the Hessian of Φ takes the form

$$H_\Phi = -\sqrt{\frac{2}{F}} \frac{1}{r^{5/2}} G(\varphi).$$

For $\varphi = 0$ the expressions simplify:

$$\begin{aligned}I(0) &= \pi \\ I'(0) &= 0 \\ I''(0) &= \frac{\pi}{8} \\ f_1(0) &= 0 \\ f_2(0) &= -\frac{\pi}{2} \\ g_1(0) &= -\frac{3\pi}{8} (= \mu_2(0)) \\ g_2(0) &= \frac{3\pi}{4} (= \mu_1(0)) \\ g_3(0) &= 0\end{aligned}$$

so that $G(\varphi = 0)$ is diagonal in the original basis, and the bunching eigenvalue $\mu_2 = g_1 = -3\pi/8$.

Appendix C

Simulation method

Exact numerical treatment of strong-field physics, by propagating the time-dependent Schrödinger equation, is challenging, since due to the laser driving large electron velocities are reached, while at the same time the details of the ionic core and its interaction with the possibly recolliding electron needs to be treated in detail. One needs short time steps and dense spatial representation for the interaction, which however makes it very costly to calculate the high velocity driven motion, regardless of using a large space-time grid [122, 123] or expansion in some basis sets [124–126].

The classical trajectory Monte Carlo method simulates classical motion after tunneling. The initial conditions are given by a model of the tunneling, which is non-classical. For this reason it is sometimes called a semiclassical method. In other branches of quantum physics the word "semiclassical" is typically used for approximations where Planck's constant is assumed to be small, taken $\hbar \rightarrow 0$ [11]. The reasoning here is completely unrelated since it is purely classical motion, with the initial conditions obtained by a quantum mechanical argument. We therefore avoid the designation "semiclassical".

C.1 Tunneling

The tunneling process is treated in line with the PPT theory, assuming an adiabatic response of the atomic ground state to the laser field. We use the instantaneous tunneling rate (probability/time) [61]:

$$w_{\perp}(p'_{\perp}, t') = \frac{1}{\mathcal{F}^2(t')} \frac{1}{\sqrt{1 + p'^2_{\perp}/2I_p}} \exp \left\{ -\frac{2}{3\mathcal{F}(t')} \left(1 + \frac{p'^2_{\perp}}{2I_p} \right)^{3/2} \right\} \quad (\text{C.1})$$

where $\mathcal{F} = F/(2I_p)^{3/2}$ is the reduced field strength. One should stress that this is the instantaneous rate, and not averaged over one laser period as is typically done in an SFA situation, which leads to Eq. (2.11) describing the final, observable spectrum.

We assume that tunneling occurs from the ground state with magnetic quantum number $m = 0$. With linear polarization the system has cylindrical symmetry around the laser polarization axis z . We therefore use cylindrical coordinates. There is no motion in the azimuthal angle $\varphi = \arctan(x/y)$ around the

polarization axis (see Fig. 3.5), so the problem is reduced to 2D. The presence of the extra dimension does however show up in the initial probability. Eq. (C.1) is written in terms of a single perpendicular component of the initial momentum; it is a conditional probability e.g. for $\varphi = 0$:

$$w(p'_x, t')|_{p'_y=0} = w_\perp(p'_\perp, t')$$

and similarly for all other angles. In order to get the total probability of a particular p_ρ one must integrate over the azimuthal angle φ , giving an additional geometrical factor of p_ρ :

$$\begin{aligned} w(p'_\rho, t') &= \int dp'_x dp'_y w(p'_x, p'_y, t') \delta\left(p'_\rho - \sqrt{p'^2_x + p'^2_y}\right) \\ &= \int d\varphi p'_\rho w_\perp(p'_\rho, t') = 2\pi p'_\rho w_\perp(p'_\rho, t') \end{aligned} \quad (\text{C.2})$$

The distribution is sampled by first normalizing $w(p_\rho, t)$ so that its maximum value is 1, which is attained when the field is maximal. Then random values \bar{t}' and \bar{p}'_ρ is chosen, and $w(\bar{p}'_\rho, \bar{t}')$ is computed for these values. Another random number ξ between 0 and 1 is generated, and if $w(\bar{p}'_\rho, \bar{t}') > \xi$, a trajectory is started. Typically between 1 and 10 million trajectories are run in order to get detailed final momentum spectra.

In the realistic simulations t' is allowed throughout the pulse. For illustration in several cases, e.g. Fig. 5.3, it is limited to the center half cycle, i.e. the range $t' \in (-\pi/2\omega, \pi/2\omega)$.

For computing deflection functions like in Fig. 5.1, the value of p_ρ and t' are chosen on an equally spaced grid, with no tunneling probability involved.

C.2 Motion

The motion after tunneling takes place in the combined field of the ion and the driving laser, governed by the Hamiltonian Eq. (2.1). It leads to the equations of motion

$$\begin{aligned} \ddot{\rho} &= \frac{\rho}{r^3} \\ \ddot{z} &= \frac{z}{r^3} - F(t) . \end{aligned}$$

Tunneling instant t' and initial radial momentum p'_ρ is randomly chosen according to Eq. (C.2). The initial conditions are then calculated as

$$\begin{aligned} p_\rho(t') &= p'_\rho \\ p_z(t') &= 0 \\ \rho(t') &= 0 \\ z(t') &= \text{tunnel exit} \end{aligned}$$

By separation in parabolic coordinates, the tunneling exit is found by numerical root finding of [38, 127]

$$0 = -2I_p z^2 + z + \frac{1}{4} + 2|F(t')|z^3$$

C.3 Focal averaging

Numerical propagation is performed by a Stoermer rule algorithm with adaptive stepsize [128, 129] until the pulse is over at $t_1 = 4\tau$, with τ the FWHM. The final energy is given directly by

$$E = \frac{\mathbf{p}^2(t_1)}{2} - \frac{1}{|\mathbf{r}(t_1)|}$$

The asymptotic momentum in pure Coulomb motion is fully determined due to conservation of energy, angular momentum and the Laplace-Runge-Lenz vector. It is computed as [91]

$$\mathbf{p} = \sqrt{2E} \frac{\sqrt{2E}(\mathbf{L} \times \mathbf{A}) - \mathbf{A}}{1 + 2E|\mathbf{L}|^2} \quad (\text{C.3})$$

where $\mathbf{L} = \mathbf{r}(t_1) \times \mathbf{p}(t_1)$ is the angular momentum and $\mathbf{A} = \mathbf{p}(t_1) \times \mathbf{L} - \mathbf{r}(t_1)/|\mathbf{r}(t_1)|$ is the Laplace-Runge-Lenz vector.

C.3 Focal averaging

Focal averaging is included by also randomizing the intensity according to the distribution $w_I(I)$ of Eq. (2.8). Extending the method for choosing the initial transverse momentum p'_ρ and tunneling instant t' , a relative intensity $i' \leq 1$ is also chosen at random. The probability Eq. (C.1), which depends parametrically on intensity through the field strength, is computed giving a value $w' = w_i(i')w(p'_\rho, p'_z, I_0 i') \in (0, 1)$. Here $w_i(i')$ is computed from Eq. (3.12). The value is then compared with an equidistributed random number $\xi \in (0, 1)$, and the trajectory is released whenever $w' > \xi$.

C.4 The Jacobian

For finding the Jacobian in Fig. 5.8, the procedure is similar to that used in calculating the deflection function. Instead of just computing the final momentum \mathbf{p} at each grid point $(p'_\rho, A(t'))$, it is also computed at four surrounding points offset by a distance Δ typically taken as $\Delta = 0.001$ au. The partial derivatives are then found by linear approximation, e.g. for the first element of the Jacobian

$$\frac{\partial p_\rho}{\partial p'_\rho} = \frac{p_\rho(p'_\rho + \Delta, A(t')) - p_\rho(p'_\rho - \Delta, A(t'))}{2\Delta}$$

C.5 The critical line

The critical line is the contour line where $\det J = 0$; however using a grid calculation, as when computing the deflection function in Fig. 5.1, and then looking for a zero does not give a sufficient accuracy unless the grid spacing is very small, making the computation costly. Instead the line is found step by step, by computing for each point the value at a distance h away in the initial phase space, at varying the angle $\arctan(p_\rho/p_z)$. See Fig. C.1. A root search is then performed, giving an accurate value of the next point along the line. An

initial value is found by searching for a root along a specific A' and varying p'_ρ in a narrow range, which is manually chosen from a low-resolution grid calculation of the Jacobian; for Fig. 5.1, the initial interval was $p'_z = 0.3$, $0.08 < p'_\rho < 0.12$.

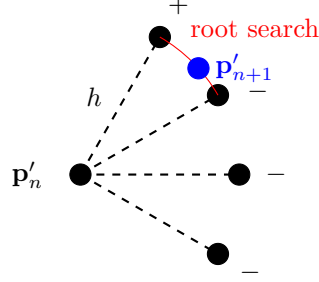


Figure C.1: Stepwise search for a zero of the Jacobian. From the current point \mathbf{p}'_n where $\det J$ is vanishing, $\det J$ is computed at a series of new points at equal distance h away varying the angle. Once a sign change is found between two points, a precision root search is performed for angles between these points, giving the next point \mathbf{p}'_{n+1} along the critical line.

C.6 The forward direction spectrum

The line of initial conditions giving forward directed motion is found in an analogous way, looking for zeros in p_ρ stepwise along the line. Once the line is found, the elements of the Jacobian matrix is computed element-wise in the same way as for Fig. 5.8 for each point along the line.

C.7 The zero energy structure

In order to include the effect of the detector on the scattering process, the basic CTMC method needs to be extended.

C.7.1 Inclusion of the electric field

The detector field is introduced by simply putting in an extra term $-\mathbf{x} \cdot \mathbf{E}_C$ in the equations of motion Eq. (C.4). Thereby the radial symmetry is preserved only if $\mathbf{E}_C \parallel \mathbf{E}_L$; otherwise a full 3D problem is obtained. For the situation of Fig. 6.17 the system is:

$$\begin{aligned} \ddot{x} &= \frac{x}{r^3} - F(t) \\ \ddot{y} &= \frac{y}{r^3} \\ \ddot{z} &= \frac{z}{r^3} - F_C . \end{aligned} \tag{C.4}$$

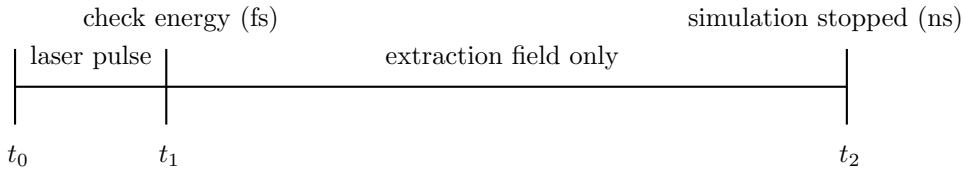


Figure C.2: Sketch of the different steps of the simulation with an extraction field.

C.7.2 The detector plate

As opposed to Section C.2 where the simulation runs for a prescribed time - until the laser pulse is negligible and motion is in the Coulomb field alone, where the asymptotic momentum is found from Eq. (C.3) - motion in a constant field never reaches an asymptotic momentum, and the momentum along the extraction field takes arbitrary large values if the running time is prolonged. The simulation needs in principle to be done like the experiment, running until the electron reaches a certain distance d , where its momentum in the perpendicular directions and its time of flight are recorded. By the same formula Eq. (6.1), the momentum distribution after interaction is reconstructed.

Since some electrons do not escape from the atom but are bound, even with the electric field of the detector, in practice one needs some maximum allowed running time.

To check the particle location at each time step introduces a complication into the numerical code, leading to significantly larger running times. An alternative approach is preferred. This makes use of the fact that well outside the interaction region, the Coulomb field plays no role any more. This has to be assumed anyway in order for the method and Eq. (6.1) to work. (In the simulation we however do not need any assumption about the *time* it takes to reach this region, in contrast to the experimental extraction where it is assumed to happen instantly and without momentum change on the way out.) One can therefore run until a certain time t_2 (corresponding to several nanoseconds), record the electron's position z_2 , and then calculate the flight time to a certain detector distance z_d using the expressions for motion in a constant field F .

$$t_d = t_2 \pm \sqrt{2|z_2 - z_d|/F}$$

with positive sign if $z_2 < z_d$, negative sign otherwise. This expression is then used in Eq. (6.1) to obtain the measured momentum $p_z^{(m)}$.

Both methods have been used and give largely identical results. A few electrons, which at the stoppage time are still in the Coulomb barrier region, will be assigned a different momentum by the second method than the first, which models the experiment more closely. The error can be minimized by making the maximum allowed running time for method 2 longer. Given that the overall computation time for a given simulation time is much shorter with method 2, there is still a gain in precision by the second method.

A further drastic simplification is made in order to make the computation time shorter. After the laser pulse, the energy of each trajectory is conserved; thus by looking at the energy at a time t_1 after the pulse is over, the influence of the detector field can be estimated. It is negligible for all energies except

in a narrow range around $E = 0$; for higher energies, the Coulomb field is negligible during the subsequent motion, and the free-flight formula Eq. (C.3) gives accurate results; for lower energies, the electron remains bound close to the ion despite the presence of the detector field. We thus stop the simulation at t_1 and check the particle energy; if it is larger than some E_{\max} , its asymptotic motion is treated by Eq. (C.3) and its final momentum recorded. As described in Section 6.4 all states below $E = -2\sqrt{F}$ remain bound forever, so only if $E(t_1) \in (-2\sqrt{F}, E_{\max})$ is the simulation allowed to continue until the time t_2 , where the momentum is obtained using method 2 above. We typically use $E_{\max} = 2\sqrt{F}$; consistency was checked by changing E_{\max} between $2\sqrt{F}$ and $10\sqrt{F}$, without noticeable difference in the results.

The modifications are completely independent of the laser parameters and the atomic species studied in the simulation. It is therefore not necessary to tailor the simulation parameters for each new problem; the extensions to the standard CTMC method are completely general. The final time t_2 can be adjusted according to the external field strength; as long as it is large enough for all interesting trajectories to escape the potential, its exact value is however largely irrelevant.

Appendix D

ZES analytics

Here we perform some analytical calculations referred to in Chapter 7. The Jacobi elliptic functions are used throughout; for an overview of their properties see e.g. [111].

D.1 Calculation of $\xi(\tau)$

$$\tau = \int^{\xi} \frac{d\xi}{\sqrt{2E\xi^2 + 2\xi(1+\beta) + \xi^3}} = \int^{\xi} \frac{d\xi}{\sqrt{\xi(\xi - \xi_1)(\xi - \xi_2)}}$$

where $\xi_{1,2} = -E \pm i\sqrt{2(1+\beta) - E^2}$. This integral corresponds to the case 17.4.71 in [78] with the real root = 0. (Note $2(1+\beta) - E^2 > 0$ for unbound motion, cf. Eq. (6.15).) We set according to 17.4.70

$$\begin{aligned} \lambda_{\xi} &\equiv (2(1+\beta))^{1/4} \\ m_{\xi} &\equiv \frac{1}{2} - \frac{1}{2} \frac{E}{\lambda_{\xi}^2} \end{aligned}$$

yielding

$$\tau = \frac{1}{\lambda_{\xi}} F(\varphi|m_{\xi}) \quad \text{where} \quad \cos \varphi = \frac{\lambda_{\xi}^2 - \xi}{\lambda_{\xi}^2 + \xi} \quad (\text{D.1})$$

Using the property of the elliptic functions that

$$\text{cn}F(\varphi|m) = \cos \varphi$$

we rewrite Eq. (D.1) as

$$\begin{aligned} \text{cn}\lambda_{\xi}\tau &= \frac{\lambda_{\xi}^2 - \xi}{\lambda_{\xi}^2 + \xi} \implies \\ \xi(\tau) &= \lambda_{\xi}^2 \frac{1 - \text{cn}\lambda_{\xi}\tau}{1 + \text{cn}\lambda_{\xi}\tau} \quad \left(= \lambda_{\xi}^2 \frac{(1 - \text{cn}\lambda_{\xi}\tau)^2}{1 - \text{cn}^2\lambda_{\xi}\tau} = \lambda_{\xi}^2 \frac{(1 - \text{cn}\lambda_{\xi}\tau)^2}{\text{sn}^2\lambda_{\xi}\tau} \right) \end{aligned}$$

which is the desired expression.

Properties

Due to properties of the function cn : $\text{cn}0 = 1$ and $\text{cn}2K = -1$, we see that

$$\begin{aligned}\xi(0) &= 0 \\ \xi &\longrightarrow \infty \text{ as } \tau \longrightarrow 2K(m_\xi)/\lambda_\xi\end{aligned}$$

where $K(m_\xi)$ is the complete elliptic integral of the first kind.

D.2 Calculation of $\eta(\tau)$

$$\tau = \int^\eta \frac{1}{\sqrt{2E\eta^2 + 2\eta(1-\beta) - \eta^3}} = \int^\eta \frac{1}{\sqrt{-\eta(\eta - \eta_1)(\eta - \eta_2)}}$$

where $\eta_{1,2} = E \pm \sqrt{E^2 + 2(1-\beta)}$. Note that $\eta_1 \geq 0$, $\eta_2 \leq 0$ and $|\eta_1| \leq |\eta_2|$ since E is negative. This integral corresponds to the case 17.4.68 in [78] with $\beta_1 = \eta_1$, $\beta_2 = 0$ and $\beta_3 = \eta_2$. We set according to 17.4.61 (substituting m for m_1)

$$\begin{aligned}\lambda_\eta &\equiv \frac{1}{2}\sqrt{\eta_1 - \eta_2} = \frac{1}{\sqrt{2}}(E^2 + 2(1-\beta))^{1/4} \\ m_\eta &= \frac{\eta_1}{\eta_1 - \eta_2} = \frac{1}{2} + \frac{E}{4\lambda_\eta^2}\end{aligned}$$

yielding

$$\tau = \frac{1}{\lambda_\eta}F(\varphi|m_\eta) \quad \text{where} \quad \sin^2 \varphi = \frac{(\eta_1 - \eta_2)\eta}{\eta_1(\eta - \eta_2)}$$

Using $\text{sn}F(\varphi|m) = \sin \varphi$ we rewrite this as

$$\begin{aligned}\text{sn}^2 \lambda_\eta \tau &= \frac{(\eta_1 - \eta_2)\eta}{\eta_1(\eta - \eta_2)} \implies \\ \eta(\tau) &= \frac{\eta_1 \eta_2 \text{sn}^2 \lambda_\eta \tau}{\eta_1 \text{sn}^2 \lambda_\eta \tau - (\eta_1 - \eta_2)} \\ &= m_\eta \frac{\eta_2 \text{sn}^2 \lambda_\eta \tau}{m_\eta \text{sn}^2 \lambda_\eta \tau - 1} \\ &= m_\eta \frac{\eta_2 \text{sn}^2 \lambda_\eta \tau}{-\text{dn}^2 \lambda_\eta \tau} = \frac{1-\beta}{\sqrt{E^2 + 2(1-\beta)}} \text{sd}^2 \lambda_\eta \tau \equiv B \text{sd}^2 \lambda_\eta \tau\end{aligned}$$

which is the desired expression.

Properties

Due to properties of the function sd : $\text{sd}0 = 0$ and $\text{sd}2K = 0$ (period $4K$ so that period of sd^2 is $2K$), we see that

$$\begin{aligned}\eta(0) &= 0 \\ \eta(\lambda_\eta \tau) &= \eta(\lambda_\eta(\tau + 2K(m_\eta)/\lambda_\eta))\end{aligned}$$

i.e. η is periodic with period $2K(m_\eta)/\lambda_\eta$.

D.3 Finding the time delay

Furthermore the maximum of sd is at K : $sdK = 1/\sqrt{1-m}$, yielding the maximum of η

$$\eta(\tau = K(m_\eta)/\lambda_\eta) = \frac{B}{1-m_\eta} = \eta_1 = E + \sqrt{E^2 + 2(1-\beta)}$$

a result easier obtained directly from setting $p_\eta = 0$ in Eq. (6.11).

D.3 Finding the time delay

The physical time is given by Eq. (7.3). The time delay giving the measured momentum is given by calculating the physical time and subtracting the effect of asymptotic motion in the constant field only. By itself Eq. (7.3) diverges as $\tau \rightarrow T_\xi$. Removing the asymptotic motion gives an expression for the time delay due to the Coulomb potential:

$$t_d = \lim_{\tau_1=T_\xi} \int_0^{\tau_1} \frac{\xi + \eta}{2} d\tau - \sqrt{\xi(\tau_1)}.$$

We treat the contribution from ξ and η separately.

D.3.1 t_ξ

We write the integral as

$$t_\xi = \int_0^{\tau_1} \frac{\xi}{2} d\tau = \frac{\lambda_\xi^2}{2} \int_0^{\tau_1} \frac{1 - \text{cn}\lambda_\xi\tau}{1 + \text{cn}\lambda_\xi\tau} d\tau$$

where we suppress the parameter m_ξ . Changing variable to $u = \lambda_\xi\tau$ gives

$$t_\xi = \frac{\lambda_\xi}{2} \int_0^{u_1} \frac{1 - \text{cn}u}{1 + \text{cn}u} du \equiv \frac{\lambda_\xi}{2} I_1$$

We rewrite the integral I_1 as

$$I_1 = \int_0^{u_1} \left(\frac{1 - \text{cn}u}{\text{sn}u} \right)^2 du = \lim_{u_0=0} \left[\int_{u_0}^{u_1} \text{ns}^2 u du + \int_{u_0}^{u_1} \text{cs}^2 u du - \int_{u_0}^{u_1} 2 \frac{\text{cn}u}{\text{sn}^2 u} du \right].$$

We are interested in the limit when $u_1 \rightarrow 2K$. Due to $\text{sn}^2 u = \text{sn}^2(2K - u)$ and $\text{cn}^2 u = \text{cn}^2(2K - u)$ we can rewrite the first integral as

$$\int_{u_0}^{u_1} \text{ns}^2 u du = \int_{u_0}^K \text{ns}^2 u du + \int_{2K-u_1}^K \text{ns}^2 u du$$

and the second similarly. Using the identities [130]

$$\begin{aligned} \int_u^K \text{ns}^2 u du &= \text{cn}u \text{ds}u + K(m) - E(m) - u + E(\text{am}u|m) \\ \int_u^K \text{cs}^2 u du &= \text{cn}u \text{ds}u - E(m) + E(\text{am}u|m) \\ \int \frac{\text{cn}u}{\text{sn}^2 u} du &= -\text{ds}u \end{aligned}$$

then gives

$$\begin{aligned}
 I_1 &= \lim_{u=0} \{2[\text{cn}udsu - E(m) + E(\text{am}u|m)] + K(m) - u - 2dsu\} \\
 &\quad + \lim_{u=2K} \{2[\text{cn}(2K-u)\text{ds}(2K-u) - E(m) + E(\text{am}(2K-u)|m)] \\
 &\quad + K(m) - (2K-u) + 2dsu\}
 \end{aligned}$$

As $u \rightarrow 0$ $\text{cnu} \rightarrow 1$, so that the problematic dsu -terms cancel out in the first limit, but in the second the divergence survives. We can write (with $E(\text{am}0|m) = E(\text{am}2K|m) = 0$)

$$I_1 = 2(K(m) - 2E(m)) + \lim_{u=2K} 4dsu .$$

In calculating the time delay, we subtract

$$\sqrt{\xi} = \lambda_\xi \frac{1 - \text{cnu}}{\text{snu}} \rightarrow \lambda_\xi \frac{2}{u - 2K}$$

where we expand snu close to $2K$. Expanding dsu similarly gives $dsu \rightarrow 1/(u - 2K)$, so that putting it all together gives

$$\begin{aligned}
 t_\xi - \sqrt{\xi} &= \frac{\lambda_\xi}{2} I_1 - \sqrt{\xi} \\
 &= \lambda_\xi \left(K(m) - 2E(m) + \lim_{u=2K} \left\{ \frac{2}{u - 2K} - \frac{2}{u - 2K} \right\} \right) \\
 &= \lambda_\xi (K(m) - 2E(m)) .
 \end{aligned}$$

The divergences cancel exactly and a compact result is obtained.

D.3.2 t_η

Here the integral can be found directly in tables [78]

$$mm_1 \int_0^u \text{sd}^2 u du = E(\text{am}u|m) - m_1 u - m \text{snuc}du \quad (\text{D.2})$$

so that

$$\begin{aligned}
 t_\eta &= \frac{B}{2} \int_0^{\tau_a} \text{sd}^2(\lambda_\eta \tau | m_\eta) d\tau \\
 &= \frac{A}{\sqrt{2}} \left(\frac{E(\text{am}u|m_\eta) - m_{\eta 1} u - m_\eta \text{snuc}du}{m_\eta m_{\eta 1}} \right)
 \end{aligned}$$

where

$$\begin{aligned}
 u &= 2 \frac{\lambda_\eta}{\lambda_\xi} K(m_\xi) \\
 A &= \frac{1 - \beta}{(E^2 + 2(1 - \beta))^{3/4}}
 \end{aligned}$$

D.4 Calculating the period of barrier orbits

We calculate the physical time

$$t = \int_0^{T_\eta} \frac{\xi(\tau) + \eta(\tau)}{2} d\tau$$

during one half-period of oscillation in η (corresponding to one quarter-period in physical coordinates), for the periodic orbits described above. Since for these orbits $\xi = |E|$,

$$t = \frac{|E|}{2} T_\eta + \int_0^{T_\eta} \frac{\eta(\tau)}{2} d\tau \quad (\text{D.3})$$

with

$$\begin{aligned} \eta(\tau) &= B \operatorname{sd}^2(\tau|m) \\ B &= 1 - \frac{E^2}{4} \\ m &= \frac{1}{2} + \frac{E}{4} \\ T_\eta &= K(m) . \end{aligned}$$

The identity Eq. (D.2) gives

$$\int_0^{T_\eta} \frac{\eta(\tau)}{2} d\tau = \frac{B}{2mm_1} (E(\operatorname{am}K(m)|m) - m_1 K(m) - m \operatorname{sn}K(m) \operatorname{cd}K(m))$$

and using the general properties of elliptic functions

$$\begin{aligned} E(\operatorname{am}K(m)|m) &= E(m) \\ \operatorname{cd}K &= 0 \end{aligned}$$

leads to

$$\int_0^{T_\eta} \frac{\eta(\tau)}{2} d\tau = \frac{B}{2mm_1} (E(m) - m_1 K(m)) .$$

Noting that

$$mm_1 = \left(\frac{1}{2} + \frac{E}{4}\right) \left(\frac{1}{2} - \frac{E}{4}\right) = \frac{1}{4} B$$

we put everything into Eq. (D.3) to get

$$t = -\frac{E}{2} K(m) + 2E(m) - 2 \left(\frac{1}{2} - \frac{E}{4}\right) K(m) = 2E(m) - K(m)$$

Multiplying by two to get the delay for one half-period gives Eq. (7.14).

Bibliography

- [1] Joseph Fraunhofer. Bestimmung des Brechungs- und des Farbenzerstreuungs-Vermögens verschiedener Glasarten in Bezug auf die Vervollkommnung achromatischer Fernröhre". *Denkschriften der Königlichen Akademie der Wissenschaften zu München*, 5:193–226, 1814.
- [2] Gustav Kirchhoff. Ueber die Fraunhofer'schen Linien. *Monatsbericht der Königlichen Preussische Akademie der Wissenschaften zu Berlin*, pages 662–665, 1859.
- [3] A. Einstein. Zur Quantentheorie der Strahlung. *Physik. Zeitschr.*, 18:121–128, 1917.
- [4] M. Göppert-Mayer. Über Elementarakte mit zwei Quantensprüngen. *Annalen der Physik*, 401:273–294, 1931.
- [5] C. I. Blaga, F. Catoire, P. Colosimo, G. G. Paulus, H. G. Muller, P. Agostini, and L. F. DiMauro. Strong-field photoionization revisited. *Nat Phys*, 5(5):335–338, 05 2009.
- [6] J. Dura, N. Camus, A. Thai, A. Britz, M. Hemmer, M. Baudisch, A. Sempf, C. D. Schröter, J. Ullrich, R. Moshhammer, and J. Biegert. Ionization with low-frequency fields in the tunneling regime. *Scientific Reports*, 3:2675, 2013.
- [7] Kaikai Zhang, Yu Hang Lai, Elias Diesen, Bruno E. Schmidt, Cosmin I. Blaga, Junliang Xu, Timothy T. Gorman, Francis Légaré, Ulf Saalman, Pierre Agostini, Jan M. Rost, and Louis F. DiMauro. Universal pulse dependence of the low-energy structure in strong-field ionization. *Physical Review A*, submitted.
- [8] Elias Diesen, Ulf Saalman, Martin Richter, Maksim Kunitski, Reinhard Dörner, and Jan M. Rost. Dynamical characteristics of Rydberg electrons released by a weak electric field. *Physical Review Letters*, submitted.
- [9] Hans A: Bethe and Edwin E. Salpeter. *Quantum Mechanics of One- and Two-Electron Atoms*. Academic Press, New York, 1957.
- [10] Harald Friedrich. *Theoretische Atomphysik*. Springer-Verlag Berlin Heidelberg, second edition, 1994.
- [11] Albert Messiah. *Quantum Mechanics, vol. 2*. North-Holland, Amsterdam, 1962.

-
- [12] A. Ludwig, J. Maurer, B. W. Mayer, C. R. Phillips, L. Gallmann, and U. Keller. Breakdown of the dipole approximation in strong-field ionization. *Phys. Rev. Lett.*, 113:243001, Dec 2014.
- [13] A D Bandrauk, F Fillion-Gourdeau, and E Lorin. Atoms and molecules in intense laser fields: gauge invariance of theory and models. *Journal of Physics B: Atomic, Molecular and Optical Physics*, 46(15):153001, 2013.
- [14] Harald Friedrich. *Theoretische Atomphysik*. Springer-Verlag Berlin Heidelberg, second edition, 1994.
- [15] Gerhard G. Paulus. Strong-field photoionization by few-cycle laser pulses. In Kaoru Yamanouchi, editor, *Progress in Ultrafast Intense Laser Science, Volume IV*. Springer, 2009.
- [16] Koudai Toyota, Ulf Saalman, and Jan M Rost. The envelope hamiltonian for electron interaction with ultrashort pulses. *New Journal of Physics*, 17(7):073005, 2015.
- [17] Dieter Meschede. *Optics, Light and Lasers*. WILEY-VCH Verlag GmbH & Co. KGaA, Weinheim, second edition, 2007.
- [18] J H Posthumus. The dynamics of small molecules in intense laser fields. *Reports on Progress in Physics*, 67(5):623, 2004.
- [19] Jan H. Posthumus and James F. McCann. Diatomic molecules in intense laser fields. In Jan Posthumus, editor, *Molecules and Clusters in Intense Laser Fields*, pages 27–83. Cambridge University Press, 2001.
- [20] P. Agostini and L. F. DiMauro. Atoms in high intensity mid-infrared pulses. *Contemporary Physics*, 49(3):179–197, 2008.
- [21] Caterina Vozzi, Matteo Negro, and Salvatore Stagira. Strong-field phenomena driven by mid-infrared ultrafast sources. *Journal of Modern Optics*, 59(15):1283–1302, 2012.
- [22] Benjamin Wolter, Michael G. Pullen, Matthias Baudisch, Michele Sclafani, Michaël Hemmer, Arne Senftleben, Claus Dieter Schröter, Joachim Ullrich, Robert Moshhammer, and Jens Biegert. Strong-field physics with mid-IR fields. *Phys. Rev. X*, 5:021034, Jun 2015.
- [23] J Ullrich, R Moshhammer, A Dorn, R Dörner, L Ph H Schmidt, and H Schmidt-Böcking. Recoil-ion and electron momentum spectroscopy: reaction-microscopes. *Reports on Progress in Physics*, 66(9):1463, 2003.
- [24] W. Becker, F. Grasbon, R. Kopold, D.B. Milošević, G.G. Paulus, and H. Walther. Above-threshold ionization: From classical features to quantum effects. *Advances in Atomic, Molecular and Optical Physics*, 48:35–98, 2002.
- [25] D B Milošević, G G Paulus, D Bauer, and W Becker. Above-threshold ionization by few-cycle pulses. *Journal of Physics B: Atomic, Molecular and Optical Physics*, 39(14):R203, 2006.

BIBLIOGRAPHY

- [26] S V Popruzhenko. Keldysh theory of strong field ionization: history, applications, difficulties and perspectives. *Journal of Physics B: Atomic, Molecular and Optical Physics*, 47(20):204001, 2014.
- [27] L. V. Keldysh. The envelope Hamiltonian for electron interaction with ultrashort pulses. *Zh. Eksp. Teor. Fiz.*, 47:1945, 1964. [Sov. Phys. JETP **20**, 1307 (1965)].
- [28] F H M Faisal. Multiple absorption of laser photons by atoms. *Journal of Physics B: Atomic and Molecular Physics*, 6(4):L89, 1973.
- [29] Howard R. Reiss. Effect of an intense electromagnetic field on a weakly bound system. *Physical Review A*, 22:1786, 1980.
- [30] H. R. Reiss. Complete Keldysh theory and its limiting cases. *Phys. Rev. A*, 42:1476–1486, Aug 1990.
- [31] Vladimir S Popov. Tunnel and multiphoton ionization of atoms and ions in a strong laser field (Keldysh theory). *Physics-Uspekhi*, 47(9):855, 2004.
- [32] Misha Yu Ivanov, Michael Spanner, and Olga Smirnova. Anatomy of strong field ionization. *Journal of Modern Optics*, 52(2-3):165–184, 2005.
- [33] S. Augst, D. D. Meyerhofer, D. Strickland, and S. L. Chin. Laser ionization of noble gases by Coulomb-barrier suppression. *J. Opt. Soc. Am. B*, 8(4):858–867, 1991.
- [34] Denys I. Bondar, Michael Spanner, Wing-Ki Liu, and Gennady L. Yudin. Photoelectron spectra in strong-field ionization by a high-frequency field. *Phys. Rev. A*, 79:063404, Jun 2009.
- [35] M Abu-samha, D Dimitrovski, and L B Madsen. The role of the atomic potential in the regime of strong-field tunnelling ionization: imprints on longitudinal and 2d momentum distributions. *Journal of Physics B: Atomic, Molecular and Optical Physics*, 41(24):245601, 2008.
- [36] L. Guo, S. S. Han, and J. Chen. Time-energy analysis of above-threshold ionization in few-cycle laser pulses. *Phys. Rev. A*, 86:053409, Nov 2012.
- [37] A Rudenko, K Zrost, C D Schröter, V L B de Jesus, B Feuerstein, R Moshhammer, and J Ullrich. Resonant structures in the low-energy electron continuum for single ionization of atoms in the tunnelling regime. *Journal of Physics B: Atomic, Molecular and Optical Physics*, 37(24):L407, 2004.
- [38] L. D. Landau and E. M. Lifschitz. *Lehrbuch der theoretischen Physik, III: Quantenmechanik*. Akademie-Verlag Berlin, ninth edition, 1994.
- [39] A M Perelomov, V S Popov, and M V Terent'ev. Ionization of atoms in an alternating electric field. *Zh. Eksp. Teor. Fiz.*, 50:1393, 1966. [Sov. Phys. JETP **23**, 924 (1966)].
- [40] A M Perelomov, V S Popov, and M V Terent'ev. Ionization of atoms in an alternating electric field: II. *Zh. Eksp. Teor. Fiz.*, 51:309, 1966. [Sov. Phys. JETP **24**, 207 (1967)].

-
- [41] M V Ammosov, N B Delone, and V P Krainov. Tunnel ionization of complex atoms and of atomic ions in an alternating electromagnetic field. *Zh. Eksp. Teor. Fiz.*, 91:2008, 1986. [Sov. Phys. JETP **64**, 1191 (1986)].
- [42] D. R. Hartree. The wave mechanics of an atom with a non-Coulomb central field. Part I. Theory and methods. *Mathematical Proceedings of the Cambridge Philosophical Society*, 24:89–110, 1 1928.
- [43] Gennady L. Yudin and Misha Yu. Ivanov. Nonadiabatic tunnel ionization: Looking inside a laser cycle. *Phys. Rev. A*, 64:013409, Jun 2001.
- [44] P. Agostini, F. Fabre, G. Mainfray, G. Petite, and N. K. Rahman. Free-free transitions following six-photon ionization of xenon atoms. *Phys. Rev. Lett.*, 42:1127–1130, Apr 1979.
- [45] E. Karule. Two-photon ionisation of atomic hydrogen simultaneously with one-photon ionisation. *Journal of Physics B: Atomic, Molecular and Optical Physics*, 11:441–447, 1978.
- [46] G G Paulus, W Becker, W Nicklich, and H Walther. Rescattering effects in above-threshold ionization: a classical model. *Journal of Physics B: Atomic, Molecular and Optical Physics*, 27(21):L703, 1994.
- [47] P. B. Corkum. Plasma perspective on strong field multiphoton ionization. *Phys. Rev. Lett.*, 71:1994–1997, Sep 1993.
- [48] G. G. Paulus, W. Nicklich, Huale Xu, P. Lambropoulos, and H. Walther. Plateau in above threshold ionization spectra. *Phys. Rev. Lett.*, 72:2851–2854, May 1994.
- [49] B W Shore and P L Knight. Enhancement of high optical harmonics by excess-photon ionisation. *Journal of Physics B: Atomic and Molecular Physics*, 20(2):413, 1987.
- [50] M. Lewenstein, Ph. Balcou, M. Yu. Ivanov, Anne L’Huillier, and P. B. Corkum. Theory of high-harmonic generation by low-frequency laser fields. *Phys. Rev. A*, 49:2117–2132, Mar 1994.
- [51] R. L. Carman, C. K. Rhodes, and R. F. Benjamin. Observation of harmonics in the visible and ultraviolet created in CO₂-laser-produced plasmas. *Phys. Rev. A*, 24:2649–2663, Nov 1981.
- [52] X. F. Li, A. L’Huillier, M. Ferray, L. A. Lompré, and G. Mainfray. Multiple-harmonic generation in rare gases at high laser intensity. *Phys. Rev. A*, 39:5751–5761, Jun 1989.
- [53] Ferenc Krausz and Misha Ivanov. Attosecond physics. *Rev. Mod. Phys.*, 81:163–234, Feb 2009.
- [54] T. Nubbemeyer, K. Gorling, A. Saenz, U. Eichmann, and W. Sandner. Strong-field tunneling without ionization. *Phys. Rev. Lett.*, 101:233001, Dec 2008.

BIBLIOGRAPHY

- [55] U. Eichmann, A. Saenz, S. Eilzer, T. Nubbemeyer, and W. Sandner. Observing Rydberg atoms to survive intense laser fields. *Phys. Rev. Lett.*, 110:203002, May 2013.
- [56] Hong Liu, Yunquan Liu, Libin Fu, Guoguo Xin, Difa Ye, Jie Liu, X. T. He, Yudong Yang, Xianrong Liu, Yongkai Deng, Chengyin Wu, and Qihuang Gong. Low yield of near-zero-momentum electrons and partial atomic stabilization in strong-field tunneling ionization. *Phys. Rev. Lett.*, 109:093001, Aug 2012.
- [57] Mihai Gavrilă. Atomic stabilization in superintense laser fields. *Journal of Physics B: Atomic, Molecular and Optical Physics*, 35(18):R147, 2002.
- [58] Qiang Li, Xiao-Min Tong, Toru Morishita, Cheng Jin, Hui Wei, and C D Lin. Rydberg states in the strong field ionization of hydrogen by 800, 1200 and 1600 nm lasers. *Journal of Physics B: Atomic, Molecular and Optical Physics*, 47(20):204019, 2014.
- [59] R. Moshhammer, J. Ullrich, B. Feuerstein, D. Fischer, A. Dorn, C. D. Schröter, J. R. Crespo Lopez-Urrutia, C. Hoehr, H. Rottke, C. Trump, M. Wittmann, G. Korn, and W. Sandner. Rescattering of ultralow-energy electrons for single ionization of ne in the tunneling regime. *Phys. Rev. Lett.*, 91:113002, Sep 2003.
- [60] K. I. Dimitriou, D. G. Arbó, S. Yoshida, E. Persson, and J. Burgdörfer. Origin of the double-peak structure in the momentum distribution of ionization of hydrogen atoms driven by strong laser fields. *Phys. Rev. A*, 70:061401, Dec 2004.
- [61] N. I. Shvetsov-Shilovski, S. P. Goreslavski, S. V. Popruzhenko, and W. Becker. Capture into Rydberg states and momentum distributions of ionized electrons. *Laser Physics*, 19:1550, 2009.
- [62] W. Quan, Z. Lin, M. Wu, H. Kang, H. Liu, X. Liu, J. Chen, J. Liu, X. T. He, S. G. Chen, H. Xiong, L. Guo, H. Xu, Y. Fu, Y. Cheng, and Z. Z. Xu. Classical aspects in above-threshold ionization with a midinfrared strong laser field. *Phys. Rev. Lett.*, 103:093001, Aug 2009.
- [63] Chengpu Liu and Karen Z. Hatsagortsyan. Origin of unexpected low energy structure in photoelectron spectra induced by midinfrared strong laser fields. *Physical Review Letters*, 105:113003, 2010.
- [64] Gennady L. Yudin and Misha Yu. Ivanov. Physics of correlated double ionization of atoms in intense laser fields: Quasistatic tunneling limit. *Phys. Rev. A*, 63:033404, Feb 2001.
- [65] Tian-Min Yan, S. V. Popruzhenko, M. J. J. Vrakking, and D. Bauer. Low-energy structures in strong field ionization revealed by quantum orbits. *Physical Review Letters*, 105:253002, 2010.
- [66] Dmitry A. Telnov and Shih-I Chu. Low-energy structure of above-threshold-ionization electron spectra: Role of the Coulomb threshold effect. *Phys. Rev. A*, 83:063406, Jun 2011.

-
- [67] Alexander Kästner, Ulf Saalman, and Jan M. Rost. Electron-energy bunching in laser-driven soft recollisions. *Physical Review Letters*, 108:033201, 2012.
- [68] Alexander Kästner, Ulf Saalman, and Jan M. Rost. Energy bunching in soft recollisions revealed with long-wavelength few-cycle pulses. *Journal of Physics B*, 45:074011, 2012.
- [69] Christoph Lemell, Konstantinos I. Dimitriou, Xiao-Min Tong, Stefan Nagele, Daniil V. Kartashov, Joachim Burgdörfer, and Stefanie Gräfe. Low-energy peak structure in strong-field ionization by midinfrared laser pulses: Two-dimensional focusing by the atomic potential. *Phys. Rev. A*, 85:011403, Jan 2012.
- [70] Christoph Lemell, Joachim Burgdörfer, Stefanie Gräfe, Konstantinos I. Dimitriou, Diego G. Arbó, and Xiao-Min Tong. Classical-quantum correspondence in atomic ionization by midinfrared pulses: Multiple peak and interference structures. *Phys. Rev. A*, 87:013421, Jan 2013.
- [71] C. Y. Wu, Y. D. Yang, Y. Q. Liu, Q. H. Gong, M. Wu, X. Liu, X. L. Hao, W. D. Li, X. T. He, and J. Chen. Characteristic spectrum of very low-energy photoelectron from above-threshold ionization in the tunneling regime. *Phys. Rev. Lett.*, 109:043001, Jul 2012.
- [72] L. Guo, S. S. Han, X. Liu, Y. Cheng, Z. Z. Xu, J. Fan, J. Chen, S. G. Chen, W. Becker, C. I. Blaga, A. D. DiChiara, E. Sistrunk, P. Agostini, and L. F. DiMauro. Scaling of the low-energy structure in above-threshold ionization in the tunneling regime: Theory and experiment. *Phys. Rev. Lett.*, 110:013001, Jan 2013.
- [73] Benjamin Wolter, Christoph Lemell, Matthias Baudisch, Michael G. Pullen, Xiao-Min Tong, Michaël Hemmer, Arne Senftleben, Claus Dieter Schröter, Joachim Ullrich, Robert Moshhammer, Jens Biegert, and Joachim Burgdörfer. Formation of very-low-energy states crossing the ionization threshold of argon atoms in strong mid-infrared fields. *Phys. Rev. A*, 90:063424, Dec 2014.
- [74] Lutz Fechner, Nicolas Camus, Andreas Krupp, Joachim Ullrich, Thomas Pfeifer, and Robert Moshhammer. Creation and survival of autoionizing states in strong laser fields. *Phys. Rev. A*, 92:051403, Nov 2015.
- [75] Diego G. Arbó, Kenichi L. Ishikawa, Emil Persson, and Joachim Burgdörfer. Doubly differential diffraction at a time grating in above-threshold ionization: Intracycle and intercycle interferences. *Nuclear Instruments and Methods in Physics Research Section B: Beam Interactions with Materials and Atoms*, 279:24 – 30, 2012. Proceedings of the Fifth International Conference on Elementary Processes in Atomic Systems Belgrade, Serbia, 21-25 June 2011.
- [76] H. B. van Linden van den Heuvell and H. G. Muller. Limiting cases of excess-photon ionization. In S. J. Smith and P. L. Knight, editors, *Multiphoton Processes*, pages 25–34. Cambridge University Press, 1987.

BIBLIOGRAPHY

- [77] A. Kamor, C. Chandre, T. Uzer, and F. Mauger. Recollision scenario without tunneling: Role of the ionic core potential. *Phys. Rev. Lett.*, 112:133003, Apr 2014.
- [78] Milton Abramowitz and Irene A. Stegun (eds.). *Handbook of Mathematical Functions*. Dover, New York, 1965.
- [79] Gilbert Grynberg, Alain Aspect, and Claude Fabre. *Introduction to Quantum Optics*. Cambridge University Press, Cambridge, 2010.
- [80] S. P. Goreslavski, G. G. Paulus, S. V. Popruzhenko, and N. I. Shvetsov-Shilovski. Coulomb asymmetry in above-threshold ionization. *Phys. Rev. Lett.*, 93:233002, Nov 2004.
- [81] Wolfgang Nolting. *Grundkurs Theoretische Physik 1: Klassische Mechanik*. Springer-Verlag Berlin Heidelberg, sixth edition, 2002.
- [82] M. Möller, F. Meyer, A. M. Saylor, G. G. Paulus, M. F. Kling, B. E. Schmidt, W. Becker, and D. B. Milošević. Off-axis low-energy structures in above-threshold ionization. *Phys. Rev. A*, 90:023412, Aug 2014.
- [83] W Becker and D B Milošević. Above-threshold ionization for very low electron energy. *Journal of Physics B: Atomic, Molecular and Optical Physics*, 48(15):151001, 2015.
- [84] M V Berry and K E Mount. Semiclassical approximations in wave mechanics. *Reports on Progress in Physics*, 35(1):315, 1972.
- [85] A Rudenko, K Zrost, Th Ergler, A B Voitkiv, B Najjari, V L B de Jesus, B Feuerstein, C D Schröter, R Moshhammer, and J Ullrich. Coulomb singularity in the transverse momentum distribution for strong-field single ionization. *Journal of Physics B: Atomic, Molecular and Optical Physics*, 38(11):L191, 2005.
- [86] Michael G Pullen, Judith Dura, Benjamin Wolter, Matthias Baudisch, Michaël Hemmer, Nicolas Camus, Arne Senftleben, Claus Dieter Schroeter, Robert Moshhammer, Joachim Ullrich, and Jens Biegert. Kinetically complete measurements of strong field ionization with mid-IR pulses. *Journal of Physics B: Atomic, Molecular and Optical Physics*, 47(20):204010, 2014.
- [87] R. Moshhammer, J. Ullrich, M. Unverzagt, W. Schmidt, P. Jardin, R. E. Olson, R. Mann, R. Dörner, V. Mergel, U. Buck, and H. Schmidt-Böcking. Low-energy electrons and their dynamical correlation with recoil ions for single ionization of helium by fast, heavy-ion impact. *Phys. Rev. Lett.*, 73:3371–3374, Dec 1994.
- [88] T. F. Gallagher. *Rydberg Atoms*. Cambridge University Press, Cambridge, 2005.
- [89] Johannes Stark. Beobachtungen über den Effekt des elektrischen Feldes auf Spektrallinien I. Quereffekt. *Annalen der Physik*, 43:965–983, 1914.

-
- [90] U. Eichmann, K. Richter, D. Wintgen, and W. Sandner. Scaled-energy spectroscopy and its relation with periodic orbits. *Phys. Rev. Lett.*, 61:2438–2441, Nov 1988.
- [91] L. D. Landau and E. M. Lifschitz. *Lehrbuch der theoretischen Physik, I: Mechanik*. Akademie-Verlag Berlin, thirteenth edition, 1988.
- [92] V. I. Arnold. *Mathematical Methods of Classical Mechanics*. Springer, second edition, 1989.
- [93] J. Gao and J. B. Delos. Resonances and recurrences in the absorption spectrum of an atom in an electric field. *Phys. Rev. A*, 49:869–880, Feb 1994.
- [94] Dieter Wintgen. Periodic orbit approach to Stark-induced resonances. *J. Phys. B*, 22:L5–L8, 1989.
- [95] V D Kondratovich and V N Ostrovsky. Resonance and interference phenomena in the photoionisation of a hydrogen atom in a uniform electric field. I. Resonances below and above the potential barrier. *Journal of Physics B: Atomic and Molecular Physics*, 17:1981–2010, 1984.
- [96] V D Kondratovich and V N Ostrovsky. Resonance and interference phenomena in the photoionisation of a hydrogen atom in a uniform electric field. II. Overlapping resonances and interference. *Journal of Physics B: Atomic and Molecular Physics*, 17(10):2011, 1984.
- [97] Christian Bordas. Classical motion of a photoelectron interacting with its ionic core: Slow photoelectron imaging. *Phys. Rev. A*, 58:400–410, Jul 1998.
- [98] Céline Nicole, Ingrid Sluimer, Florentina Rosca-Pruna, Marcel Warntjes, Marc Vrakking, Christian Bordas, Frederic Texier, and Francis Robicheaux. Slow photoelectron imaging. *Phys. Rev. Lett.*, 85:4024–4027, Nov 2000.
- [99] C. Nicole, H. L. Offerhaus, M. J. J. Vrakking, F. Lépine, and Ch. Bordas. Photoionization microscopy. *Phys. Rev. Lett.*, 88:133001, Mar 2002.
- [100] Ch. Bordas, F. Lépine, C. Nicole, and M. J. J. Vrakking. Semiclassical description of photoionization microscopy. *Phys. Rev. A*, 68:012709, Jul 2003.
- [101] Harald Friedrich and Johannes Trost. Working with WKB waves far from the semiclassical limit. *Physics Reports*, 397(6):359 – 449, 2004.
- [102] R. Côté, H. Friedrich, and J. Trost. Reflection above potential steps. *Phys. Rev. A*, 56:1781–1787, Sep 1997.
- [103] Thomas Fennel, Lora Ramunno, and Thomas Brabec. Highly charged ions from laser-cluster interactions: Local-field-enhanced impact ionization and frustrated electron-ion recombination. *Phys. Rev. Lett.*, 99:233401, Dec 2007.

BIBLIOGRAPHY

- [104] B. Schütte, M. Arbeiter, Th. Fennel, M. J. J. Vrakking, and A. Rouzée. Rare-gas clusters in intense extreme-ultraviolet pulses from a high-order harmonic source. *Phys. Rev. Lett.*, 112:073003, Feb 2014.
- [105] B. Schütte, F. Campi, M. Arbeiter, Th. Fennel, M. J. J. Vrakking, and A. Rouzée. Tracing electron-ion recombination in nanoplasmas produced by extreme-ultraviolet irradiation of rare-gas clusters. *Phys. Rev. Lett.*, 112:253401, Jun 2014.
- [106] V. V. Beletsky. *Essays on the Motion of Celestial Bodies*. Springer Basel AG, 2001.
- [107] Gregory Lantoine and Ryan P. Russell. Complete closed-form solutions of the Stark problem. *Celestial Mechanics and Dynamical Astronomy*, 109(4):333–366, 2011.
- [108] W. Pauli. Über das Wasserstoffspektrum vom Standpunkt der neuen Quantenmechanik. *Zeitschrift für Physik*, 36:336, 1926.
- [109] Aneta S. Stodolna. *Taking Snapshots of Atomic Wave Functions with a Photoionization Microscope*. PhD Thesis, Radboud University Nijmegen, 2014.
- [110] Karl F. Sundman. Mémoire sur le problème des trois corps. *Acta mathematica*, 36:105, 1912.
- [111] E. T. Whittaker and G. N. Watson. *A Course of Modern Analysis*. Merchant Books, second edition, 1915.
- [112] Léon van Hove. The occurrence of singularities in the elastic frequency distribution of a crystal. *Physical Review*, 89:1189, 1953.
- [113] Mark S. Child. *Semiclassical Mechanics with Molecular Applications*. Clarendon Press, Oxford, 1991.
- [114] M.V. Berry. Waves and Thom’s theorem. *Advances in Physics*, 25(1):1–26, 1976.
- [115] Vladimir I. Arnold. *Catastrophe Theory*. Springer-Verlag Berlin Heidelberg, third edition, 1992.
- [116] M. Morse. Relations between the critical points of a real function of n independent variables. *Trans. Amer. Math. Soc.*, 27:345–396, 1925.
- [117] M. Morse. The critical points of a function of n variables. *Trans. Amer. Math. Soc.*, 33:72–91, 1931.
- [118] Hassler Whitney. On singularities of mappings of Euclidean spaces. I. Mappings of the plane into the plane. *Annals of Mathematics*, 62:374–410, 1912.
- [119] Arlie O. Petters, Harold Levine, and Joachim Wambsganss. *Singularity Theory and Gravitational Lensing (Progress in Mathematical Physics Vol. 21)*. Springer Science+Business Media New York, 2001.

-
- [120] Evan O. Kane. Critical-point structure in photoelectric emission energy distributions. *Phys. Rev.*, 175:1039–1048, Nov 1968.
- [121] R. Car, G. Ciucci, and L. Quartapelle. Calculation of angular photoelectric spectra. *Solid State Communications*, 21:289–291, 1977.
- [122] Kenneth C. Kulander. Multiphoton ionization of hydrogen: A time-dependent theory. *Phys. Rev. A*, 35:445–447, Jan 1987.
- [123] K. J. Schafer and K. C. Kulander. Energy analysis of time-dependent wave functions: Application to above-threshold ionization. *Phys. Rev. A*, 42:5794–5797, Nov 1990.
- [124] E Cormier and P Lambropoulos. Above-threshold ionization spectrum of hydrogen using B-spline functions. *Journal of Physics B: Atomic, Molecular and Optical Physics*, 30(1):77, 1997.
- [125] Th. Mercouris, Y. Komninos, S. Dionissopoulou, and C. A. Nicolaides. Computation of strong-field multiphoton processes in polyelectronic atoms: State-specific method and applications to H and Li^- . *Phys. Rev. A*, 50:4109–4121, Nov 1994.
- [126] Shaohao Chen, Xiang Gao, Jiaming Li, Andreas Becker, and Agnieszka Jaroń-Becker. Application of a numerical-basis-state method to strong-field excitation and ionization of hydrogen atoms. *Phys. Rev. A*, 86:013410, Jul 2012.
- [127] Adrian N. Pfeiffer, Claudio Cirelli, Mathias Smolarski, Darko Dimitrovski, Mahmoud Abu-samha, Lars Bojer Madsen, and Ursula Keller. Attoclock reveals natural coordinates of the laser-induced tunneling current flow in atoms. *Nature Physics*, 8:76–80, 2012.
- [128] E. Hairer, S. P. Norsett, and G. Wanner. *Solving Ordinary Differential Equations I. Nonstiff Problems (Springer Series in Computational Mathematics)*. Springer-Verlag, 1993.
- [129] Available at <http://www.unige.ch/~hairer/software.html> (retrieved 2015-12-07).
- [130] Harris Hancock. *Elliptic Integrals (Mathematical Monographs No. 18)*. John Wiley & Sons, Inc., New York, 1917.

Versicherung

Diese Arbeit wurde am Max-Planck-Institut für Physik komplexer Systeme unter der wissenschaftlichen Betreuung Prof. Dr. Jan-Michael Rosts durchgeführt. Hiermit versichere ich, dass ich die vorliegende Arbeit ohne unzulässige Hilfe Dritter und ohne Benutzung anderer als der angegebenen Hilfsmittel angefertigt habe; die aus fremden Quellen direkt oder indirekt übernommenen Gedanken sind als solche kenntlich gemacht. Die Arbeit wurde bisher weder im Inland noch im Ausland in gleicher oder ähnlicher Form einer anderen Prüfungsbehörde vorgelegt.

Darüber hinaus erkenne ich die Promotionsordnung der Fakultät Mathematik und Naturwissenschaften der Technischen Universität Dresden vom 23. Februar 2011 an.

Elias Diesen

Dresden, 29. Januar 2016